NOTICE

The quality of this microform is heavily dependent upon the quality of the original thesis submitted for microfilming. Every effort has been made to ensure the highest quality of reproduction possible.

If pages are missing, contact the university which granted the degree.

Some pages may have indistinct print especially if the original pages were typed with a poor typewriter ribbon or if the university sent us an inferior photocopy.

Reproduction in full or in part of this microform is governed by the Canadian Copyright Act, R.S.C. 1970, c. C-30, and subsequent amendments.

AVIS

La qualité de cette microforme dépend grandement de la qualité de la thèse soumise au microfilmage. Nous avons tout fait pour assurer une qualité supérieure de reproduction.

S'il manque des pages, veuillez communiquer avec l'université qui a conféré le grade.

La qualité d'impression de certaines pages peut laisser à désirer, surtout si les pages originales ont été dactylographiées à l'aide d'un ruban usé ou si l'université nous a fait parvenir une photocopie de qualité inférieure.

La reproduction, même partielle, de cette microforme est soumise à la Loi canadienne sur le droit d'auteur, SRC 1970, c. C-30, et ses amendements subséquents.

HEAT TRANSFER
IN ROD BUNDLE SUBCHANNELS

by

MOHAMED SADOK GUELLOUZ

A thesis
presented to the University of Ottawa
on September, 1989
in partial fulfillment of the
requirements for the degree of
MASTER of APPLIED SCIENCE
in
MECHANICAL ENGINEERING

Ottawa-Carleton Institute for
Mechanical and Aeronautical Engineering

ISBN 0-315-60034-9

UNIVERSITÉ D'OTTAWA
UNIVERSITY OF OTTAWA

Abstract

Presented in this study is an experimental investigation of heat transfer in a model of the 37-rod CANDU reactor bundle. Measurements were conducted at 34.2 rod diameters from the duct entrance and at a Reynolds number of 74000. The study was mainly focused on the effect of the rod-wall proximity on the local heat transfer coefficient and on the flow mean and fluctuating temperatures.

Localized heat was provided by a narrow heated strip mounted on the central rod, which could be traversed within the duct and rotated about its axis. The relative variation of the "apparent" local heat transfer coefficient around the central rod was determined for various rod-wall proximities including the two limiting cases of rod-wall contact and rod-rod-wall contact.

The measurements show that the heat transfer coefficient is minimum near narrow gaps and maximum in open flow regions. The minimum heat transfer coefficient at the gap generally decreased with decreasing gap size, but its decrease was appreciable only at very small gaps.

The flow temperature measurements were concentrated on the rod-wall gap variation. The statistics of the temperature fluctuations showed a deviation from Gaussianity, that was more pronounced as the gap diminished. Asymmetry of the mean temperature and the temperature fluctuation con-

tours is observed with the heater near the gap as well as facing the sub-channel centre.

Acknowledgements

I express deep gratitude to Professor Stavros Tavoularis for his motivating guidance and encouragement, for providing a comfortable working atmosphere and for being always available for discussions. His quick and careful editing of the manuscript and his comments contributed significantly to the quality of the thesis. I also express my thanks to Professors J.T. Rogers and S.C. Cheng for reading and commenting on this thesis.

I wish to thank D^r S. Sutradhar of AECL for providing feedback, as well as, my colleagues in the fluid mechanics group: Gordon Holloway (from whom, I learned a lot), D^r Umesh Karnik (for his help with the instrumentation and data acquisition), Faouzi Trabelsi (for helping in setting the final version of the thesis), Brahim Chebbi and Mohsen Ferchichi, with all of whom I shared a warm academic experience.

I extend my thanks to Don Seaman, the department administrative officer, and the technical staff of the departmental workshop.

The financial support provided by the Atomic Energy of Canada Limited (AECL), the Scientific Mission of Tunisia and the Natural Sciences and Engineering Research Council of Canada (NSERC), University-Industry Program, is greatly appreciated.

Finally, I am indebted to Sonia for her support, encouragement and help; and to my family for their consistent morale support.

Nomenclature

A	exposed area of the heating block, also subchannel cross-sectional area
c_p	specific heat
D	rod diameter
dA	elementary area of the heated strip
D_h	37 element rod bundle hydraulic diameter
D_{h_m}	present model hydraulic diameter
$D_{h_{T_1}}$	inner triangular subchannel 1 hydraulic diameter
$D_{h_{T_2}}$	inner triangular subchannel 2 hydraulic diameter
D_{hw}	wall subchannel hydraulic diameter
F	flatness factor
f	Fanning friction factor
g	gravitational acceleration
Gr	Grashof number
h	convective heat transfer coefficient
h_a	apparent heat transfer coefficient
$\hat{h_a}$	average apparent heat transfer coefficient
h_c	corrected heat transfer coefficient
$\hat{h_c}$	average corrected heat transfer coefficient
k	thermal conductivity
L	heated strip length
Nu	Nusselt number
P	pitch (distance between rod centres)
Pr	Prandlt number
q	heat convected from the heated strip
q_{in}	total heat input to the heating block
q_l	heat loss from the heating block
R	radius of pressure tube
r	radial distance from the rod surface
Re	Reynolds number
R_2	radius of middle ring of rods
R_3	radius of outer ring of rods
S	skewness factor
St	Stanton number

T	temperature
t	time
$T_{m,n}$	temperature at node (m,n)
T_w	wall temperature
T_{wc}	wall temperature at the center of the heated strip
t_o	time interval for averaging
T_∞	unheated flow temperature
U_b	bulk velocity
U_i	velocity component along axis i
u_i	fluctuating velocity along axis i
W	wall subchannel width
x	distance along the heated strip

GREEK SYMBOLS

β	coefficient of thermal expansion, also peripheral coordinate with respect to the heater axis
δ	rod-wall gap width
θ	fluctuating temperature
λ_{θ_1}	streamwise Corrsin microscale
μ	dynamic viscosity
ν	kinematic viscosity
ρ	density
ϕ	peripheral coordinate
ϕ_o	angular position of the heater axis
τ	wall shear stress

SUBSCRIPTS AND SUPERSCRIPTS

$\overline{(\,)}$	time average value
$(\,)'$	root mean square value

Table of Contents

List of Tables

List of Figures

Chapter 1

Introduction

Commercial nuclear technology has developed dramatically during the past four decades, leading to a variety of reactor designs. Nuclear reactors can be generally classified, according to the type and state of the coolant, into the following categories: Pressurized Water Reactors (PWRs), Boiling Water Reactors (BWRs), Gas Cooled Reactors (GCRs) and Pressurized Heavy Water Reactors (PHWRs).

The only standardized commercial model of PHWRs is the CANDU (CANadian Deuterium Uranium) reactor, designed and developed by the Atomic Energy of Canada Limited (AECL).

Presented in Figure 1.1 is a 600 MW (electrical) CANDU nuclear power

unit. The reactor comprises a large horizontal, cylindrical, stainless steel vessel, called Calandria, housed within a light water-filled, steel lined, concrete structure (the Calandria vault), which provides radiation shielding and cooling. The Calandria contains heavy water (D_2O) moderator, reactivity control mechanisms and about 380 identical pressure tubes that contain natural uranium fuel bundles through which pressurized (9.6 MPa), high temperature, heavy water coolant from the heat transport system is directed. The heavy water coolant removes heat produced by fission in the fuel elements, to carry it to the steam generators. The produced light water steam is fed to the turbine-generator system to produce electricity.

The pressure tubes, made of Zirconium alloy, are about 6 m long and 100 mm in diameter and have a wall thickness of 4 mm. Each pressure tube contains a string of twelve 37-rod fuel bundles (Figure 1.2) stacked end to end. The rods are each 13.08 mm in diameter and arranged in a compact pattern.

The efficiency of the reactor depends on the thermal-hydraulic performance of the bundles, which in turn, depends upon the geometry of the rod subchannels and the flow structure.

Each rod contains fissile material, i.e natural uranium, enclosed in a Zircaloy sheath. This sheath constitutes the first of a number of barriers against release of the radioactive fission products to the surroundings.

Therefore, it is of major importance that the sheath remains intact during the operating life of the fuel elements. The risk of damage of the sheath, either by chemical interaction with the coolant or by exceeding the mechanical strength of the sheath material, is closely related to the value and distribution of the sheath temperature. Consequently, an important factor in the design calculations for nuclear fuel elements is the knowledge of heat transfer. Previous studies of heat transfer in rod bundles have mostly focussed on the prediction of bulk properties, and cannot predict the precise local temperature distribution, especially under distorted subchannel geometries.

The neutron flux gradients across the fuel bundles produce a non-uniform temperature distribution across the fuel pins, which may lead to bowing of rods towards neighboring ones or towards the wall. This may result in a change of the thermal-hydraulic performance of the bundles, since the flow structure and heat transfer would be affected.

The present work is aimed at investigating the variation of heat transfer, as well as providing turbulence and temperature distributions in an outer rod's vicinity, with this rod at its design position as well as displaced towards another rod and/or the sheath.

The experimental work was carried in two stages. The first stage covered the measurement of the local heat transfer coefficient, while the second stage

involved the measurement of the flow mean and fluctuating temperatures.

It is hoped that the present results will contribute to the understanding of heat transfer processes within the CANDU reactor and could be useful towards further development of thermal-hydraulic codes for reactor design and safety.

Chapter 2

Literature Review

2.1 General Comments

Turbulent flow and heat transfer in rod bundles are distinctly three-dimensional problems and, therefore, their analytical description generally requires the use of three dimensional conservation equations (momentum, energy and mass). This presents a major difficulty in dealing with such flows.

While both analytical and numerical solutions are available for laminar flow in rod bundles, two approximate approaches have been developed to describe the turbulent flow case. The "standard" approach consists of a "subchannel analysis" in which the mean velocity and fluid temperature

are averaged over the subchannel. This method can only provide Nusselt number correlations with various parameters and peripherally averaged wall temperatures in the subchannels. The second approach is a local analysis, where detailed velocity and temperature distributions are sought. Numerical methods, based on finite element or finite difference analyses, have so far been used. However, these require several assumptions, including the incorporation of turbulent models, the validity of which can only be assessed by comparison with experimental data.

It is observed, from the available literature, that studies of fluid flow are far more numerous than those of heat transfer. A literature review of turbulent flow in rod bundle subchannels of various shapes has been presented by Ouma [1988]. The following sections will summarize previous findings concerning heat transfer in rod bundles.

2.2 Subchannel Studies

A comprehensive literature review of heat transfer in rod bundles has been presented by Rehme [1987]. For the fully developed turbulent heat transfer, he focused on triangular and rectangular subchannels.

In the case of an infinite triangular array, he presented a correlation by Petukhov and Roisen [1974], in which the Nusselt number in the subchannel is related to the Nusselt number of a circular tube. This correlation

represents an upper limit for pitch to diameter (P/D) ratios from 1 to 4.

According to Rehme [1987], the same correlation can be reasonably applied to square subchannels with P/D greater than 1.3 .

Barrow et al [1984] investigated the case of a corner subchannel at W/D=1.0 (wall subchannel width to diameter ratio). They obtained a ratio of the subchannel Nu to the circular tube Nu equal to 0.38.

2.3 Local Analyses

2.3.1 Wall Temperature and Heat Transfer Coefficient Distributions

Berger and Ziai [1982] and Berger et al [1986] used an electrochemical analogy method to obtain the variation of the local Stanton number (St) with angle from the line of closest approach (i.e. line joining the two centers of adjacent rods), relative displacement and Reynolds number. Two geometries were studied: a single rod in a channel and a seven-rod cluster, in which several rods could be moved or bent simultaneously.

Palmer and Swanson [1963] studied heat transfer for parallel air flow in a seven-rod cluster, with P/D=1.015 and at a Reynolds number of 20,000. They found that the average heat transfer coefficient in a triangular sub-

channel was approximately equal to the one for smooth circular pipe, while the peripheral variation of the local heat transfer coefficient varied between 0.5 and 1.3 of the average value.

Hoffman et al [1970] performed extensive experimental work on fluid flow and heat transfer in a seven-rod cluster. They obtained wall temperature variation around the central rod and an outer one. In another part of their work, they used a mass transfer analogy to obtain the heat transfer coefficient distribution for different rod-rod and rod-wall separations.

2.3.2 Heat Transport and Temperature Distribution in the Coolant

Nijsing et al [1966] attempted a theoretical analysis of fluid flow and heat transfer in a triangular array of parallel rods. They considered two boundary conditions, namely uniform peripheral heat flux distribution and uniform peripheral surface temperature distribution.

Axford [1967] developed an analytical "multiregion" method to predict temperature fields in the coolant, cladding and fuel regions of a rod-bundle.

Ramm and Johannsen [1975] used the "turbulence model" approach to e solve the momentum and energy equations. To describe the Reynolds stresses and turbulent heat fluxes, they formulated a "phenomenological"

turbulence model based on Buleev's theoretical model [1962,1964]. They applied the obtained model to predict the turbulent diffusivity of heat in triangular and square infinite rod arrays.

Mohanty and Sohoo [1988] analyzed turbulent flow and heat transfer in triangular and square subchannels for P/D from 1.1 to 1.5, using a two-dimensional eddy diffusivity and a higher order "k-l" model.

Based on an experimental investigation, Ingesson and Hedberg [1970] developed a calculation method to predict intersubchannel mixing for various channel geometries.

Sutherland and Kays [1966] analyzed turbulent heat transfer in triangular parallel rod arrays using the technique of superposition of fundamental solutions to solve the energy equation. The fundamental solutions were determined experimentally. This method allows the prediction of the heat transfer performance with arbitrarily specified heat flux distributions, once the fundamental solutions are established.

Meyder [1975] developed a method to calculate local heat transfer coefficient, temperature, mixing rate, friction factor and wall shear stress distribution in a central subchannel of a fuel element. A limitation of this method is that it neglects the effect of secondary flows.

Rogers and Tahir [1975,1979] reported that secondary flows assist turbulent interchange by reducing the mixing distance, thus explaining the

insensitivity of the turbulent interchange mixing rates to P/D variation. They also stated that secondary flows increase the gradients of temperature, velocity and turbulent stresses across the gap.

Seale [1979] investigated analytically and experimentally the mixing by turbulent diffusion and secondary flows between subchannels of rod bundles. In a second publication of the same year, he performed a numerical study using the "k-ε" model. He confirmed the findings of Rogers and Tahir [1975], that the intersubchannel mixing rates are higher than predicted by simple diffusion theories, and insensitive to P/D variations. He observed also, that the effective diffusivities through the gap were strongly anisotropic, but he did not obtain any evidence of secondary flows.

In another study, Seale [1981] postulated that the anisotropy of diffusivities, rather than secondary flows, was the dominant mechanism causing the enhanced intersubchannel mixing rates.

Chapter 3

Definitions and Background Information

3.1 Hydraulic Diameter and Bulk Quantities

A considerable amount of information about the velocity and temperature fields in circular pipe flows is available from experimental and theoretical studies. It is customary to compare results of fluid flow and heat transfer through channels of non-circular cross-section with those in circular pipes with comparable flow conditions (e.g. Reynolds number). The obvious characteristic length of a circular pipe is its diameter. A commonly used

characteristic length for non-circular channels is the hydraulic diameter, defined as four times the channel cross-sectional area, divide by its wetted perimeter.

For the 37-element rod bundle, shown in Figure 3.1, the hydraulic diameter is:

$$D_h = \frac{\pi(4R^2 - 37D^2)}{2\pi R + 37\pi D} \tag{3.1}$$

where R is the radius of the pressure tube and D is the diameter of the rods.

The hydraulic diameter of the present model (Figure 3.1), obtained by taking into account the additional flat walls, is (Ouma [1988])

$$D_{h_m} = \frac{4(\frac{\pi}{6}R^2 - \frac{1}{2}(R_1 + D)^2 \cos\frac{\pi}{6} - \frac{5\pi D^2}{4} - (\frac{2\pi R_3 - 18D}{18})(R - (R_1 + D)))}{\frac{\pi}{6}R - 2(\frac{2\pi R_3 - 18D}{18}) + (R_2 - D) + 2(R - (R_2 - D)) + 5\pi D} \tag{3.2}$$

It has been established by previous studies that the velocity and temperature distributions close to the channel wall are essentially independent of the shape of the channel cross section. In rod bundle flows, the flow through individual subchannels depends mainly on the local flow conditions. Therefore, the flow parameters for each subchannel can be estimated by substituting the subchannel hydraulic diameter, for the pipe diameter, in relations developed for circular pipe flows.

As shown in Figure 3.1, two types of subchannels of interest are present in the experimental model. Subchannels bounded by the outer curved wall,

termed wall subchannels, and subchannels bounded by rods only, termed inner subchannels; the latter ones are in this case "triangular" subchannels.

The hydraulic diameter of the wall subchannels for the design position is

$$D_{h_W} = \frac{4(\frac{\pi}{18}R^2 - \frac{\pi}{18}R_3^2 - \frac{97\pi}{720}D^2)}{\frac{\pi R}{9} + \frac{97\pi D}{180}} \tag{3.3}$$

The hydraulic diameters of the two triangular subchannels are given by

$$D_{h_{T_1}} = \frac{0.51(2R_2 sin\frac{\pi}{12})(2R_3 sin\frac{\pi}{18})}{\pi D} \tag{3.4}$$

and

$$D_{h_{T_2}} = \frac{0.69(2R_2 sin\frac{\pi}{12})^2}{\pi D} \tag{3.5}$$

Experiments in turbulent flows have proved that the use of the hydraulic diameter in correlations for circular pipes gives a reasonably good approximation of gross flow parameters in channels of various cross-sectional shapes, provided there are no sharp corners, or, generally, no appreciable non-uniformity in the wall shear stress distribution. Obviously this approach can not provide peripheral variation of various parameters like the heat transfer coefficient and the wall temperature, as it can only give estimates of the averages over the channel. Nevertheless, these averaged parameters are useful for comparisons.

The subchannel bulk velocity is defined as

$$U_b = \frac{Total\ flow\ rate}{A} \tag{3.6}$$

where A is the subchannel cross-sectional area.

The Reynolds number, which represents the ratio of the inertial forces to the viscous forces, is the most commonly used dimensionless parameter to characterize a flow. For a subchannel it is given by

$$Re = \frac{U_b D_h}{\nu} \tag{3.7}$$

where D_h is the subchannel hydraulic diameter and ν the kinematic viscosity of the fluid.

When a fluid at rest or in motion is in contact with a surface at a different temperature, energy flows in the direction of the lower temperature. The flux of energy leaving (or entering) the surface can be related to the wall, T_w, and fluid, T_f, temperatures by Newton's law of cooling,

$$q = hA(T_W - T_f) \tag{3.8}$$

where A is the surface area in contact with the fluid. The proportionality factor, h, is called the convective heat transfer coefficient.

The Nusselt number, which represents the ratio of convective energy flux to conductive energy flux in the fluid, is defined as

$$Nu = \frac{hD_h}{k} \tag{3.9}$$

where k is the thermal conductivity of the fluid.

Another dimensionless number, useful for comparing the performances

of various channels, is the Stanton number,

$$St = \frac{h}{\rho c_p U_b} \tag{3.10}$$

where ρ and c_p are respectively the density and specific heat of the fluid. The Stanton number represents the ratio of the quantity of heat actually transferred to the thermal capacity of the fluid. It is related to the Nusselt and Reynolds numbers as follows:

$$St = \frac{Nu}{Re.Pr} \tag{3.11}$$

where Pr is the Prandtl number, defined as

$$Pr = \frac{c_p \mu}{k} \tag{3.12}$$

The Prandtl number represents the ratio of the momentum diffusion to the thermal diffusion in a fluid at rest or in laminar flow.

3.2 Heat and Momentum Transfer Analogy

Reynolds [1874] postulated that the laws governing momentum and heat transfer were analogous. He concluded that, in geometrically similar systems, a simple proportionality relation must exist between the fluid friction and heat transfer. Formulated mathematically, the Reynolds analogy yields

$$St = \frac{h}{U c_p \rho} = \frac{f}{2} \tag{3.13}$$

where f is the Fanning friction factor, defined as

$$f = \frac{\tau}{\frac{1}{2}\rho U^2} \tag{3.14}$$

Equation 3.13 is a reasonable approximation of turbulent heat transfer data for fluids which have a Prandtl number close to 1.

Prandtl [1910] and Taylor [1916] extended Reynolds' work to take into account the velocity distribution, by subdividing the flow into two regions: a turbulent region where the kinematic viscosity, ν, and the thermal diffusivity, α, are negligible; and a laminar region where the eddy viscosity and eddy diffusivity are negligible compared to ν and α. It resulted in the following analogy equation:

$$\frac{h}{\rho c_p U} = \frac{f/2}{1 + 5\sqrt{f/2}(Pr - 1)} \tag{3.15}$$

Von Karman [1939] further extended the theory to include the buffer layer. He used the universal velocity distribution to obtain the relationship

$$\frac{h}{\rho c_p U} = \frac{f/2}{1 + 5\sqrt{f/2}(Pr - 1 + \ln(1 + \frac{5}{6}(Pr - 1)))} \tag{3.16}$$

For $Pr = 1$, the above equation reduces to the Reynolds analogy, i.e. equation 3.13.

Additional modifications have been introduced to these analogies by several authors, mainly by the use of empirical relations.

3.3 Statistical Definitions

The cumulative distribution function $F_\chi(x)$ of a random variable, χ, is defined as the probability that $\chi \leq x_1$. The probability density function (pdf) of χ is the derivative of its distribution function

$$f_\chi(x) = \frac{dF_\chi(x)}{dx} \tag{3.17}$$

The expectation, or mean of a random variable, χ, is defined as

$$E\{\chi\} = \overline{x} = \int_{-\infty}^{+\infty} x f_\chi(x) dx \tag{3.18}$$

In general the moment of n^{th} order is

$$\overline{x^n} = \int_{-\infty}^{+\infty} x^n f_\chi(x) dx \tag{3.19}$$

The variance is given by

$$\sigma^2 = E\{(\chi - E\{\chi\})^2\} = \overline{(x-\overline{x})^2} = \int_{-\infty}^{+\infty} (x-\overline{x})^2 f_\chi(x) dx \tag{3.20}$$

The standard deviation, or root-mean-square (rms) is the positive square root, σ, of the variance.

The central moment of the n^{th} order is defined as

$$\overline{(x-\overline{x})^n} = \int_{-\infty}^{+\infty} (x-\overline{x})^n f_\chi(x) dx \tag{3.21}$$

The degree of a symmetry of a distribution can be evaluated by the "skewness factor"

$$S = \frac{\overline{(x-\overline{x})^3}}{\sigma^3} \tag{3.22}$$

The "flatness factor", defined as

$$F = \frac{\overline{(x - \overline{x})^4}}{\sigma^4} \tag{3.23}$$

is used to supplement the information obtained from the variance. In the case of a normal distribution F=3.

A random process is said to be statistically stationary if its statistics are not affected by a shift in the time origin.

A random process is called ergodic if all its statistics can be determined from a single member of the ensemble.

3.4 Statistical Properties of a Scalar Quantity Transported by a Turbulent Flow

Turbulence is a highly irregular, rotational and three dimensional fluid motion in which the flow quantities vary randomly with time and space. It always occurs at large Reynolds number and it enhances mixing and kinetic energy dissipation.

Any passive (i.e. quantities which have no effect on the velocity field, e.g. small amounts of heat) scalar quantity that may be present in a turbulent flow is transported by turbulence in a manner similar to the turbulent momentum transport.

Due to its random nature turbulence can only be described by statistical means.

Using Reynolds' decomposition procedure, the instantaneous velocity components and temperature can be decomposed into mean and fluctuations as

$$U_i = \overline{U_i} + u_i \qquad T = \overline{T} + \theta \tag{3.24}$$

where overbars denote averages and, by definition, $\overline{u_i} = \overline{\theta} = 0$.

Using the stationary and ergodic hypotheses, the following relations can be derived (the analysis will be presented for temperature fluctuations, but the same treatment is valid for velocity fluctuations). The mean, or average temperature can be computed as

$$\overline{T} = \lim_{t_o \to \infty} \frac{1}{2t_o} \int_{-t_o}^{+t_o} T(t)dt \tag{3.25}$$

Similarly, the central moment of the n^{th} order is obtained as

$$\overline{\theta^n} = \lim_{t_o \to \infty} \frac{1}{2t_o} \int_{-t_o}^{+t_o} \theta^n(t)dt \tag{3.26}$$

The skewness and the flatness factor can be calculated as

$$S = \frac{\overline{\theta^3}}{(\overline{\theta^2})^{\frac{3}{2}}} \tag{3.27}$$

and

$$F = \frac{\overline{\theta^4}}{(\overline{\theta^2})^2} \tag{3.28}$$

The streamwise "Corrsin" (temperature) microscale is by definition:

$$\lambda_{\theta 1} = \sqrt{\frac{2\overline{\theta^2}}{\overline{(\partial\theta/\partial x_1)^2}}} \tag{3.29}$$

Using Taylor's "frozen flow" approximation, expressed as

$$\frac{\partial}{\partial x_i}(\,) \approx -\frac{1}{\overline{U_i}}\frac{\partial}{\partial t}(\,) \tag{3.30}$$

the streamwise (the coordinate system is defined in Figure 3.2) microscale can be estimated from the mean square temporal derivative of temperature as

$$\lambda_{\theta 1} = \overline{U_1}\sqrt{\frac{2\overline{\theta^2}}{\overline{(\partial\theta/\partial t)^2}}} \tag{3.31}$$

In a turbulent scalar field, spectral analysis provides the distribution of scalar fluctuation activity over different eddy sizes, or, inversely, different wavenumber ranges. With the turbulent eddies considered as convected by the mean speed, one can define the frequency spectrum $F(f)$ as the Fourier transform of the auto-correlation function, $R_\theta(\tau)$, as

$$F(f) = \int_{-\infty}^{+\infty} R_\theta(\tau) e^{-i2\pi f\tau} d\tau \tag{3.32}$$

where $R_\theta(\tau) = \overline{\theta(0)\theta(\tau)}$.

Chapter 4

Flow Facility and Instrumentation

4.1 Flow Facility

The general experimental set-up is shown in Figure 4.1. Excluding the heated section, it has been described in Ouma [1988].

The flow facility is a 12.9 upscale model of an outer segment of the 37-rod bundle of the CANDU reactor. It consists of five circular pipes, arranged in a quasi-trapezoidal duct with a circular arc top, as shown in Figure 4.2. The central pipe was suspended at both ends so that it could be traversed sideways, while the other four were held fixed on the duct walls.

The movable rod could also be rotated by 360° about its axis. Definitions of the rod diameter, D, rod-wall gap, δ, peripheral coordinate, ϕ, radial coordinate, r, rod pitch, P, and wall subchannel width, W, are included in Figure 4.2.

4.2 Heating Element

In order to permit heat transfer measurements, a heating block was added to the original set-up near the downstream end of the central rod. The position, geometry and materials of the heated section are shown in Figures 4.3, 4.4 and 4.5. The heating block was embedded in an insulated section of the rod, made mainly of wood. The heating block, made of copper, was 381 mm long, had an exposed width of 9.5 mm and was placed in a cast cement shroud, providing further thermal insulation between the heater and the wooden section. Thin wooden strips were used for covering the sides of the heating block, while the space underneath these strips was filled by loose fiberglass insulation.

An electric cartridge heater was used to provide the required heat. It is an 1100 W heater, 381 mm long and having a diameter of 9.5 mm. A variable transformer was used to adjust the power input. The heater was sandwiched between two sections of the heating block. Thermal paste (silicone compound) was used to improve heat conduction from the heater

to the copper block. The geometry of the block was selected in order to provide sufficient localized heat on the rod surface and a nearly uniform surface temperature.

4.3 Temperature Measuring Instrumentation

4.3.1 Wall and Free Stream Temperatures

Considering their superior sensitivity within the temperature range of interest (20 to 60°C), thermistors (Fenwal Electronic, 2000 Ω) were selected for the measurement of the heating-element surface temperature. Special thermistor assemblies, consisting of glass-coated beads mounted on slender aluminum disks (see Figure 4.6) have been used.

Thermistor positions on the heating block are shown in Figure 4.5. They were operating with the use of a home-made electronic circuit (Figure 4.7), providing nearly linear output. The circuit could power up to four thermistors and could provide outputs corresponding to individual thermistors as well as to differences between two thermistor voltages.

The unheated flow temperature was measured using a similar thermistor assembly, mounted on one of the fixed rods, upstream of the heated section.

4.3.2 Flow Mean Temperature

The flow mean temperature was measured by a glass-coated thermistor mini-probe (Fenwal Electronics, 2000 Ω), which was mounted on slender support (2 mm diameter, 70 mm long) in order to reduce probe interference.

The probe was operated with an electronic circuit (similar to the one presented in Figure 4.7) which can operate two thermistors.

4.3.3 Flow Fluctuating Temperature

The fluctuating temperature was measured with a 1.3 μm platinum wire, mounted on a subminiature probe, (DANTEC, model 9055A) operating at a constant current of 0.4 mA supplied by an active bridge (Peattie [1987]). A diagram of this circuit is provided in Figure 4.8. It consists of an ultra-low drift precision voltage source and a voltage-to-current converter, which supplies the cold-wire with a constant current.

4.4 The Traversing Mechanism

All flow temperature measurements were taken at nearly 65 hydraulic diameters downstream from the flow entry. The probes were inserted into the test section from the exit end of the duct. The probe mounting and traversing systems (Figure 4.9) were designed and constructed in the de-

partmental workshop. They permitted accurate traversing azimuthally, radially and longitudinally.

4.5 The Calibration Jet

The thermistor and cold wire probes were calibrated in the heated airflow produced by the calibration jet shown in Figure 4.10. The jet was designed and constructed at the University of Ottawa.

The flow, produced by a centrifugal blower, was passed through various turbulence-reducing screens, a settling chamber and then through a 24:1 axisymmetric contraction with a 22.5 mm exit diameter. In order to perform the calibration of temperature probes, the flow was heated using electric heaters placed immediately after the fan.

4.6 The Data Acquisition System

Thermistor signals were acquired using digital averaging voltmeters (TSI, model 1076).

The cold wire (i.e. fluctuating temperature) signals were observed on a dual beam storage oscilloscope (Tektronix, model 5113), and conditioned with high gain, low noise, instrumentation amplifiers (Tektronix 5A22N).

The amplifiers provided gains ranging from 0.1 to 50,000 and had built-in high pass and low pass filters with a 3 dB drop-off per octave.

The conditioned signals were digitized using an analog-to-digital converter, mounted on an IBM-PC-AT compatible personal computer (system 1800, 1 MB Random Access Memory). The A/D board had a 5 mV resolution (12 bit, $\pm$10V input range).

The PC featured a hard disk with 20 MB storage capacity and a magnetic cartridge drive (60 MB).

The data were acquired with the use of a software package (Data Translation, ATLAB) and stored on cartridge tapes to be processed at a later time.

Chapter 5

Experimental Procedures and Accuracies

5.1 Heat Transfer Measurement

The amount of heat, δq, convected (per unit time) from an elementary surface with area δA and temperature T_w to a flowing stream with temperature T_∞ is related to these quantities by Newton's law of cooling

$$\delta q = h\delta A(T_w - T_\infty) \tag{5.1}$$

where h is, by definition, the local convective heat transfer coefficient. In general, $\delta q, T_w$ and h would vary with position. In the present experimental model, the total convective heat flux from the heated surface to the fluid

would be (see Figure 5.1 for definition of coordinates)

$$q = \int_0^L \int_{\phi_1}^{\phi_2} h(x,\phi)[T_w(x,\phi) - T_\infty] r d\phi dx \tag{5.2}$$

Due to the high conductivity of copper, the surface temperature of the heater is not expected to vary substantially. In the present experiments, it will be represented by a typical value, T_{wc}, measured near the center of the heating strip. Estimates of the temperature variation along the heater will be presented later.

Another complication arises from the fact that, instead of the actual convective heat flux from the heater surface, the present technique provides the total power input

$$q_{in} = q + q_l \tag{5.3}$$

which includes heat losses, q_l, mainly to the surrounding insulation, which are eventually transferred to the fluid by convection from the wooden surface of the rod. Numerical estimates of heat losses, using a finite difference technique, have been performed and are presented in chapter 6. These estimates show that losses can be substantial, up to 40% of the total power input. An analysis of their effect upon the accuracy of the measured heat transfer coefficient will also be presented later.

It is clear from the above discussion that the exact local heat transfer coefficient, h(x,ϕ), as it appears in equation (5.2), cannot be determined with the present setup. What will be presented below is a directly measurable,

"apparent" heat transfer coefficient, defined as

$$h_a = \frac{q_{in}}{A(T_{wc} - T_\infty)} \tag{5.4}$$

where A is the exposed area of the heater. It is also obvious that this value could be substantially higher than the one computed using q instead of q_{in}. However, the purpose of the current study is not to measure the precise value of heat transfer coefficient (which, in any case, would be different from the one in the operating reactor) but, rather, its sensitivity upon position and subchannel size. The angular position of the heater can be defined by the angular coordinate

$$\phi_o = \frac{1}{2}(\phi_1 + \phi_2) \tag{5.5}$$

of its plane of symmetry. The values of h_a will be normalized with the corresponding average "apparent" heat transfer coefficient, define as

$$\hat{h_a} = \frac{1}{2\pi}\int_0^{2\pi} h_a(\phi_o)d\phi_o \tag{5.6}$$

It should be noted that this quantity would be different from the average heat transfer coefficient for a fully heated rod, because of differences in the temperature fields of the two systems.

A "corrected" heat transfer coefficient, h_c, based on an estimate ratio q/q_{in}, will also be presented with the measurements of h_a. It is defined as

$$h_c(\phi_o) = \left(\frac{q}{q_{in}}\right)_{est} h_a(\phi_o) \tag{5.7}$$

The numerical analysis provides the ratio $(q/q_{in})_{est}$ as a function of $h_a/\hat{h}_a$. Therefore, the relative variation of the "corrected" heat transfer coefficient can be expressed as

$$\frac{h_c}{\hat{h}_c} = \frac{f\left(h_a/\hat{h}_a\right)}{\frac{1}{2\pi}\int_0^{2\pi} f\left(\frac{h_a}{\hat{h}_a}\right) d\phi_o} \tag{5.8}$$

where

$$f\left(\frac{h_a}{\hat{h}_a}\right) = \left(\frac{q}{q_{in}}\right)_{est} \frac{h_a}{\hat{h}_a} \tag{5.9}$$

As described in the previous chapter, special thermistor assemblies were used to measure the above temperatures. Prior to their mounting on the rod, the thermistors were calibrated in the heated jet of the calibration tunnel, versus a mercury thermometer with a $0.1°C$ resolution. The thermistor circuits were adjusted such that the individual calibration curves (see Figure 5.2) had the same shape.

The thermistor outputs were measured using averaging voltmeters with a resolution of 1 mV. Considering a typical sensitivity of the thermistor circuit output of $0.034\ V/°C$, the resolution of the temperature measuring system would, ideally, be $0.03\ °C$.

The power input to the electric heater was obtained by measuring the current and voltage inputs using analog instrumentation (Figure 5.3). Taking into account the meter resolutions, one would anticipate a resolution of about 0.5% in power input measurements. However, fluctuations in the power line voltage were occasionally observed, which combined with the

relatively slow time response of the heater, would further contaminate the measuring accuracy. At a later stage of this work, a regulating transformer became available, which almost entirely (within 0.1%) removed power input fluctuations.

Following an error analysis, the "absolute (maximum) error" in measuring the "apparent" heat transfer coefficient was estimated to be 0.8 %.

A fortran computer program using finite difference technique was developed, to study the heat losses from the heating block. It is described thoroughly in chapter 6.

5.2 Mean Temperature Measurement

To account for possible drift in the ambient temperature, the temperature rise was measured with respect to the free stream temperature, obtained with a thermistor placed upstream of the heated section. The heated strip temperature was also monitored using thermistors. The input voltage to the heater was kept nearly constant by the use of a voltage regulator.

The same procedure, as in the previous section, was followed in calibrating the above thermistors and their circuits.

5.3 Temperature Fluctuation Measurement

The cold-wire was calibrated in the heated jet of the calibration tunnel using a previously calibrated thermistor probe as a reference.

Considering the low level of the signal, the cold wire output was amplified by a factor of 10,000. However for the calibration, only an amplification of 10 was used, since high gains resulted in a considerable drift of the DC output of the amplifier. A typical calibration curve for the cold wire is presented in Figure 5.4. It shows that the cold wire sensitivity to temperature was 0.46 $V/°C$ at a gain of 10,000.

Prior to its digitization, the signal was low-pass filtered at 3 kHz (3 dB drop-off) to eliminate the high-frequency noise. The above choice of filter cut-off is near the upper limit of the frequency response of cold wires such as the present ones to temperature fluctuations (Hojstrup et al. [1976]). The power spectrum of the cold wire (Figure 5.5) indicates that more than 95% of the temperature signal is contained in the part of the spectrum below 1000 Hz.

The insensitivity of the cold wire to velocity changes was verified by traversing the wire in the test section for an unheated flow.

The noise to signal ratio was defined as $\overline{e_n^2}/\overline{e_s^2}$ where the nominator is the mean square of the output voltage of the cold wire in the unheated flow

and the denominator is the mean squared voltage in the heated flow.

Close to the heater the noise to signal ratio was typically of the order of 1.5%. It was also obtained that the noise had a nearly Gaussian probability density function (Figure 5.6). It is customary to assume the noise to be statistically independent of the temperature fluctuations, and therefore apply simple corrections to eliminate the noise contamination.

Typical power spectra measured with the cold wire in the unheated and in the heated flow are shown in Figure 5.5. The noise contribution to the total "energy" is approximately 1%.

5.4 Computational Procedures

A discrete time history of the temperature signal θ_n^m (n=1,2,....N; m=1,2,....M) was acquired, consisting of M=40 records, each containing N=4096 data points. Successive records were separated by intervals 1 sec long. The sampling time interval between consecutive data points was 0.13 msec. Although the cold-wire outputs were AC-coupled to the digitizers, the record averages were subtracted from the digitized signals in order to eliminate possible residual offsets in the data acquisition system.

5.4.1 One-Point Moments

For the temperature fluctuations, the one point moments were calculated from the discrete time history as:

$$\overline{\theta^n} = \frac{\sum_{j=1}^{M} \sum_{i=1}^{N} (\theta_i^j)^n}{N \times M} \tag{5.10}$$

where n is the order of the moment.

5.4.2 Spectral Calculations

The discrete Fourier transform, Θ_k^m, of each data record was calculated with the use of a Fast Fourier Transform, as

$$\Theta_k^m = \sum_{n=1}^{N} \theta_n^m e^{-\frac{i(2\pi nk)}{N}} \tag{5.11}$$

k=1,2,....N/2 m=1,2,....M

The power spectral estimate was then obtained by

$$\hat{F}_k = \frac{1}{MN} \sum_{m=1}^{M} \Theta_k^m (\Theta_k^m)^* \tag{5.12}$$

k=1,2,....N/2

the * indicates the complex conjugate of the quantity.

5.4.3 Probabilistic Calculations

First the discrete time history was normalized by the corresponding standard deviation σ_θ, as

$$s_n^m = \frac{\theta_n^m}{\sigma_\theta} \tag{5.13}$$

Then the probability density $P_s(\eta)$ of the normalized signal was obtained as

$$P_s(\eta) = \frac{P(\eta - \frac{w}{2} \leq s_n^m \leq \eta + \frac{w}{2})}{w} \tag{5.14}$$

where the numerator represents the probability over the interval $[\eta - \frac{w}{2}, \eta + \frac{w}{2}]$, i.e the number of data points in the interval divided by the total number of points. The window, w, was chosen wider for large η and narrower for small η.

Chapter 6

Numerical Estimation of Heat Losses

The "apparent" heat-transfer coefficient was evaluated by measuring the wall and unheated flow temperatures and the electrical power input to the heating element.

However, as indicated earlier, part of the generated heat was conducted through the insulation to the wooden rod. Therefore, it is of interest to estimate the relative magnitude of these losses. Considering the complexity of the heating-block geometry (Figure 4.4), it appears that the most suitable approach to the problem would be the numerical one. The numerical method selected for this application is based on the finite-difference technique.

6.1 Principles of the Finite Difference Technique

The details of the finite difference technique are available in most heat transfer textbooks (e.g. Holman [1981] and Patankar [1980]). Presented below are the most relevant principles. Consider a two-dimensional body, whose cross-section is fitted by a rectangular grid with equal node spacing in both the x and y directions. Using the nomenclature shown in Figure 6.1(a), the temperature gradients at different nodes of the grid can be approximated as follows :

$$\left.\frac{\partial T}{\partial x}\right]_{m+1/2,n} \approx \frac{T_{m+1,n} - T_{m,n}}{\Delta x} \tag{6.1}$$

$$\left.\frac{\partial T}{\partial x}\right]_{m-1/2,n} \approx \frac{T_{m,n} - T_{m-1,n}}{\Delta x} \tag{6.2}$$

$$\left.\frac{\partial T}{\partial y}\right]_{m,n+1/2} \approx \frac{T_{m,n+1} - T_{m,n}}{\Delta y} \tag{6.3}$$

$$\left.\frac{\partial T}{\partial y}\right]_{m,n-1/2} \approx \frac{T_{m,n} - T_{m,n-1}}{\Delta y} \tag{6.4}$$

$$\left.\frac{\partial^2 T}{\partial x^2}\right]_{m,n} \approx \frac{-\left.\frac{\partial T}{\partial x}\right]_{m+1/2,n} - \left.\frac{\partial T}{\partial x}\right]_{m-1/2,n}}{\Delta x} = \frac{T_{m+1,n} + T_{m-1,n} - 2T_{m,n}}{(\Delta x)^2} \tag{6.5}$$

$$\left.\frac{\partial^2 T}{\partial y^2}\right]_{m,n} \approx \frac{\left.\frac{\partial T}{\partial y}\right]_{m,n+1/2} - \left.\frac{\partial T}{\partial y}\right]_{m,n-1/2}}{\Delta y} = \frac{T_{m,n+1} + T_{m,n-1} - 2T_{m,n}}{(\Delta y)^2} \qquad (6.6)$$

For two-dimensional, steady state heat transfer, the general heat conduction equation is

$$\frac{\partial}{\partial x}(k\frac{\partial T}{\partial x}) + \frac{\partial}{\partial y}(k\frac{\partial T}{\partial y}) + \dot{q} = 0 \qquad (6.7)$$

where k is the thermal conductivity and $\dot{q}$ the heat generation per unit area.

For a constant conductivity and equal increments in x and y (i.e. $\Delta x = \Delta y$), Equation 6.7 combined with Equations 6.5 and 6.6 gives

$$T_{m+1,n} + T_{m-1,n} + T_{m,n+1} + T_{m,n-1} - 4T_{m,n} + \frac{\dot{q}(\Delta x)^2}{k} = 0 \qquad (6.8)$$

In the case of a composite wall (with no heat generation), such as the one shown in Figure 6.1(b), Equation 6.7 is approximated as follows

If $f \leq 0.5$

$$\left(\frac{k'}{(1-f)k' + fk}\right) T_{m+1,n} + T_{m-1,n} + T_{m,n+1} + T_{m,n-1} - \left(3 + \frac{k'}{(1-f)k' + fk}\right) T_{m,n} = 0$$

If $f > 0.5$ (6.9)

$$\left(\frac{k'}{(1-f)k' + fk}\right) T_{m+1,n} + T_{m-1,n} + \left((\frac{3}{2} - f) + \frac{k'}{k}(f - \frac{1}{2})\right) (T_{m,n+1} + T_{m,n-1})$$
$$- \left(1 + \frac{k'}{(1-f)k' + fk} + 2\left((\frac{3}{2} - f) + \frac{k'}{k}(f - \frac{1}{2})\right)\right) T_{m,n} = 0$$

A different configuration arises when the solid is exposed to a convective boundary (Figure 6.1(c)). Then, the general heat conduction equation becomes:

$$\left(\frac{h\Delta x}{k}+2\right)T_{m,n}-\frac{h\Delta x}{k}T_{\infty}-\frac{1}{2}(2T_{m-1,n}+T_{m,n+1}+T_{m,n-1})=0 \quad (6.10)$$

For a corner with convection boundary, as in Figure 6.1(d), the nodal equation can be written as

$$2\left(\frac{h\Delta x}{k}+1\right)T_{m,n}-\frac{2h\Delta x}{k}T_{\infty}-T_{m-1,n}+T_{m,n-1}=0 \quad (6.11)$$

For any other configuration, the nodal equation can be obtained in a similar manner.

6.2 Present Application

In view of the approximate nature of this study and the limitations on the computer memory available, the actual heated section geometry was approximated by a simpler one, shown in Figure 6.2. The dimensions and shape of the heating block, insulation shroud and loose insulation were kept the same, while the rod was approximated by a rectangular section instead of the circular one. The obtained convection area was nearly equal to the one of the circular rod. At the bottom, a perfect insulation was used, which is equivalent to assuming that all the heat is convected from the upper half

of the rod. Advantage was taken of the symmetry of the body to reduce the number of required nodes by half.

The body was divided into equal segments in both x and y directions. Using the finite difference technique, the nodal equations were written for each node. Then, the obtained system of linear equations was solved directly using an IMSL (International Mathematical and Statistical Library) subroutine. This direct method of solution, though it needs a large memory space, presents an advantage over iterative techniques, because it requires orders of magnitude less computing time.

The computation was repeated for different values of thermal conductivities of the heated section materials in order to study the sensitivity of the results to these thermal conductivity values. The obtained results showed a very weak dependence on the assumed conductivity of the copper block. In fact, for $\pm 20\%$ variation of this conductivity, the maximum percentage difference was 0.25%. A relatively low sensitivity was also found with respect to the conductivities of the insulation and the cement shroud (for 20% variation in conductivity, the difference in the losses was 5% and 3%, respectively). However, in the case of the wood, a 20% variation in conductivity resulted in 10% change in the heat losses.

A second test was run in order to determine the effect of the numerical grid-spacing on the heat losses estimation. Nearly the same heat loss

(within 2%) was obtained for 1.91 and 2.22 mm grid spacing.

Figure 6.3 presents isotherm contours obtained for a uniform heat transfer coefficient around the body. It shows that the copper block would be at a relatively uniform temperature and that most of the heat would be convected from the heated strip and the part of wall adjacent to it.

As expected, the percentage heat loss was found constant with a variation in the heat input. However, it decreased slightly with increasing convective heat-transfer coefficient. Figure 6.4 is a plot of such a variation. It shows that the losses are comparable in magnitude to the heat convected from the copper strip. In fact, the losses represent about 40% of the heat input, which would imply that the heat-transfer coefficient would also be overestimated by about 40%.

This result was confirmed by estimates (for the design geometry, ϕ_0=0) of the heat losses based on measurements of the surface temperature around the heated rod. The rod surface near the heater was divided to a number of strips defined by the angular sectors, α_i (Figure 6.5).The corresponding surface temperature, T_i, on each strip was measured using a thermistor in contact with the surface. The ratio of the heat convected from the copper strip to the total heat input can be approximated as

$$\frac{q}{q_{in}} = \frac{hA_1(T_1 - T_\infty)}{\sum hA_i(T_i - T_\infty)} \tag{6.12}$$

Assuming a uniform convective heat transfer coefficient over the surface

(the variation being less than 2% over the 30° angle) and calculating the strip area as

$$A_i = (\frac{\pi}{180} DL)\alpha_i \tag{6.13}$$

Equation (6.12) becomes

$$\frac{q}{q_{in}} = \frac{\alpha_1(T_1 - T_\infty)}{\sum \alpha_i(T_i - T_\infty)} \tag{6.14}$$

Using the measured values of T_i (Figure 6.5) one may estimate that the ratio of the heat convected from the copper strip to the total heat would be about 57%, i.e. that the losses from the wooden section would be about 43% of the power input.

Corrections to the "apparent" heat-transfer coefficient distributions, $h_a/\hat{h_a}$, can be based on the estimated dependence of the ratio q/q_{in} upon the ratio $h_a/\hat{h_a}$, according to Equations (5.8) and (5.9). These estimates are obtained from computations performed for few cases of $h_a/\hat{h_a}$, with the convective heat-transfer coefficient being h_a over the heated strip and $\hat{h_a}$ over the rest of the body. Figure 6.6 presents the variation of $(q/q_{in})_{est}$ and $f(h_a/\hat{h_a})$ for the range $0 \leq h_a/\hat{h_a} \leq 1.4$, which more than covers the present experimental range.

The sensitivity of this correction procedure to the assumed distribution of h_a over the numerical model was tested by performing a second estimation (referred to as "estimate 2") of the ratio q/q_{in}, by assuming that the convective heat transfer coefficient had a uniform value, h_a, over the entire

top of the body and another value, $\hat{h_a}$, over the two sides. The results of the above two estimates are shown in Figure 6.6 where "estimate 1" refers to the first estimation. It is seen that the two estimates nearly coincide in the range $0.6 \leq h_a/\hat{h_a} \leq 1.4$ .The distributions used in these two estimations represent extreme cases for the convective heat transfer coefficient distribution close to the heated strip. As their differences are insignificant, the results of "estimate 1" will be used to correct the "apparent" heat transfer coefficient distributions.

Chapter 7

The Measurements

7.1 Preliminary Tests

A number of preliminary tests were conducted prior to the measurements.

The flow temperature was monitored during the starting period of the wind tunnel. Figure 7.1 shows that this temperature would typically stabilize after a period of about 60 minutes.

Similarly, the heating block temperature was plotted against time, starting at the moment when the heater was turned on (Figure 7.2). This figure indicates that steady state was reached after about 2 hours.

Thus, all measurements were taken after both the fan and the heater were in operation for at least 3 hours.

Figure 7.3 is a plot of the temperature of the heating element, after rotation of the rod carrying the element, which resulted in a step change in the convective heat transfer. It shows that a period of 60 minutes should elapse between measurements at different heater orientations.

The flow rate through the duct was monitored and was found to be essentially constant with time. The Reynolds number, based on the bulk flow velocity and the hydraulic diameter of the wall subchannel at the design geometry was about 74,000. This value, although lower than the estimated value of 450,000 in the operating reactor, is large enough for the subchannel flow to be fully turbulent. It has also been established (Ouma [1988]) that the flow was fully developed at the measuring location near the outlet of the duct. Since the measurements are based on a typical temperature, T_{wc}, measured near the center of the heating strip, a test was done to estimate the temperature variation along the heater for the working conditions. It was found that the maximum temperature variation would be less than 1% of the difference between the wall and free stream temperatures. Therefore, the temperature, T_{wc}, near the center of the heating strip should be a relatively good approximation of the average surface temperature.

7.2 Heat Transfer Measurements

Detailed measurements of the local "apparent" heat transfer coefficient around the periphery of the central rod were conducted for the design geometry, as well as for several other cases with varying rod-wall and/or rod-rod proximities. The measured values are provided in Table 7.1, while the corresponding value of the average "apparent" heat transfer coefficient (Equation 5.6), calculated by integrating a fourth order polynomial fitted to the measurements, are presented in Table 7.2. The same results are plotted in Figures 7.4 to 7.7. The measurements clearly show that the local heat transfer coefficient is minimum near narrow gaps and maximum in open flow regions. The irregular variation of this coefficient can be attributed partly to measuring uncertainty but mainly to secondary flow effects.

As shown in Figure 7.6, a reduction in W/D results in a decrease of h_a at the rod-wall gap. This decrease is appreciable at values of W/D close to 1 , but relatively small at W/D around the design value. The average heat transfer coefficient is much less sensitive to gap size than the local one is.

The case in which the central rod was in contact with both the wall and a neighboring rod (Figure 7.7) presented the lowest $\hat{h}_a$ and two regions of relatively low values of h_a, one near the rod-wall contact line and another near the rod-rod contact line. The values of h_a in the confined subchannel were substantially lower than those in the free subchannels.

7.3 Temperature Measurements

7.3.1 Mean Temperature

The heating element constitutes a stepwise discontinuity in the rod surface temperature. Although the velocity profile is fully developed, due to the small size of the heater and the complexity of the bundle cross-section, the thermal boundary layer is three-dimensional and cannot reach full development in the measuring section. Radial profiles of the mean temperature were measured for several downstream positions. Figure 7.8, shows the downstream development of isotherms, for different angles, ϕ_o, and different gap sizes. The lines shown in this Figure are smoothened curves through the measurements, which, in some occasions, exhibit considerable scatter. It is seen that the thermal layer thickness decreases as the gap size diminishes. It is also obvious that the spatial resolution increases, downstream.

For this reason, it was decided to take all subsequent measurements at a station 330 mm downstream of the starting of the heating element, close to its downstream end.

Mean temperature profiles are presented in Figure 7.9, for different gap sizes and different angular positions of the heating element. It can be seen that the temperature gradients, close to the rod surface, become larger as the gap diminishes.

Figure 7.10 shows radial profiles of the mean temperature for different angular positions with respect to the heating element, which was kept at $\phi_o = 0°$. The same measurements are presented in contour form in Figure 7.11. Isotherm contours are shown in Figure 7.12, for the design position with $\phi_o = 45°$. It is clear that these contours are asymmetric, bulging towards the rod-wall gap.

7.3.2 Temperature Fluctuations

Typical samples of the fluctuating cold-wire signals at three radial positions in the heated flow and at one position in the unheated flow are shown in Figure 7.13. It is clear that, near the heated surface, the effects of noise and sensitivity to velocity on this signal would be negligible but they would become severe with increasing distance.

Figures 7.14, 7.15 and 7.16 present radial profiles of the root mean square (rms) of the temperature fluctuations. Figure 7.17(a) is a replot of 7.16 in contour form, while the remaining plots in figure 7.17 are "constant-θ'" contours for different gap sizes. It can be observed that for smaller gaps the thermal layer is squashed, i.e it becomes thinner in the radial direction and expands in the azimuthal direction. This is illustrated in Figure 7.18.

The "constant-θ'" contours, in the cases where the heating element is at $\phi_o = -45°$ and 5° respectively, are shown in Figure 7.19. As in the case of

the mean temperature for $\phi_o = -45°$, the contours bulge towards the gap while they bulge toward the open flow region for $\phi_o = 5°$.

7.3.3 Probability Density Function, Skewness And Flatness

Figure 7.20, shows the probability density function (pdf) of the temperature fluctuations for several radial positions at the design conditions and with the heating element on the gap ($\phi_o = 0°$). The shown pdfs depart from the standard normal distribution (also represented in the figure) and become more peaked towards the cold fluid with distance from the heated wall.

The pdfs, shown in Figure 7.21 (for different gap sizes), show a measurable deviation from "Gaussianity" and a skewness that increases with diminishing gap sizes. Also, as the gap decreases the pdfs become more peaked.

Measurements of skewness factors for several rod and heating elements configurations were obtained. Figure 7.22 displays that the skewness factor was nearly constant in the radial direction, while it increased with decreasing W/D. The flatness factor, on the other hand, was observed (Figure 7.23) to increase both radially and with decreasing W/D. This confirms the results reported in Figures 7.20 and 7.21. All measurements have been corrected for electronic noise and sensitivity of the cold-wire to velocity

fluctuation by assuming that these quantities are uncorrelated with the temperature fluctuations.

7.3.4 Corrsin Microscale

The Corrsin microscales were calculated employing Equation 3.31 and using measurements of $\overline{U_1}$ obtained with a pitot-static tube. Figure 7.24 shows the variation of the streamwise Corrsin microscales in the radial position. It reveals that λ_{θ_1} was nearly constant in the radial direction, but decreased with diminishing gap size.

Chapter 8

Analysis and Discussion of Results

8.1 Comparison of the Present Model with an Operating Reactor Bundles

Prior to the discussion of the results, it seems necessary to compare the experimental model with the actual reactor bundle, and to address the possible consequences of the differences between the two facilities.
A summary of these differences is presented in Table 8.1.

Except for the addition of side walls and the absence of [illegible]s, rod

spacers and upstream bundles, the present model is geometrically similar to the CANDU bundle. Dynamic similarity would be achieved by matching the Reynolds numbers in the two situations, provided that the flow can be assumed as incompressible and single-phase and that gravitational forces are negligible.

The relative importance of natural convection from the heated surface can be assessed based on the value of the Grashof number, which for the present experimental conditions was estimated to be, typically,

$$Gr = \frac{g\beta(T_{wc} - T_\infty)L^3}{\nu^2} = 1.2 \times 10^9 \qquad (8.1)$$

where g is the gravitational acceleration, β the coefficient of thermal expansion of air, L the length of the heated strip and ν is the kinematic viscosity of air, evaluated at the film temperature $\frac{1}{2}(T_{wc} + T_\infty)$. Because heat transfer correlations corresponding to the present experimental geometry are not readily available, correlations established for heat transfer from vertical and horizontal flat plates were used instead (Kakaç [1987]). All estimates showed that natural convection would be negligible, so that forced convection would by far be the dominant mode of heat transfer.

The model Reynolds number is lower than the one in the actual bundle, although both correspond to fully turbulent flow. Since in general, the higher the Reynolds number is, the thinner the wall layer would be, the heat transfer coefficient would tend to be larger in the actual bundle than

in the model.

The mechanism of turbulent heat transfer from a solid wall to a fluid flowing in a channel involves three zones: wall viscous layer, buffer layer and turbulent core. The heat leaving the wall is conducted through the viscous sublayer and delivered to the buffer layer, where heat is transferred partly by turbulent transport and partly by conduction under the influence of the transverse gradient in temperature. The heat is then transferred to the turbulent core where turbulent transport dominates. The turbulent transport depends on the flow characteristics while conduction is driven by the temperature gradient.

At the measuring station, the velocity profile is fully developed, however the temperature profile is not. In the present model, only a narrow strip on one of the rods is heated, while in the actual bundle, all rods are heated. Furthermore, materials are different in the two systems. Therefore the detailed paths of heat transfer are different in the two cases.

8.2 Heat Transfer Coefficient

It was concluded from the numerical study of heat losses from the heated rod section, that the tabulated values of the heat transfer coefficient (Tables 7.1 and 7.2) would be overestimated by a substantial amount. Table 7.3 compares h_a and h_c (for the design position, $\phi_o = 0$) to heat transfer

coefficients obtained using different analogies and correlations. It is also expected that the distributions presented in Figures 7.4 to 7.7 would be somewhat different from the distributions of the actual local heat-transfer coefficient. Figure 8.1 illustrates the differences between the distributions of the ratios $h_a/\hat{h_a}$ and $h_c/\hat{h_c}$. Although $\hat{h_c}$ is 40% smaller than $\hat{h_a}$ (Table 7.2), the above ratios differ by a relatively small amount.

Figures 8.2 to 8.5 are replots of all measurements, corrected for the conductive heat losses to the insulation. Compared to the corresponding "apparent" heat transfer coefficient measurements (Figures 7.4 to 7.7) the "corrected" ones appear qualitatively similar but with more pronounced extremes.

As shown in Figures 7.4, 7.5 and 7.7, the local heat transfer coefficient distributions have minima near narrow gaps and maxima in open flow regions. It can also be seen that the heat transfer coefficient does not increase monotonically from the rod-wall gap towards the open flow regions. This trend has already been reported for the wall shear stress by several authors (Tavoularis and Ouma [1988], Kjellstrom [1974], Trupp and Azad [1975] and Rehme [1978,1980,1982]), and was attributed to the effect of secondary flows. These effects become stronger with diminishing the gap size.

8.3 Flow Temperature

As shown in Figures 7.8 and 7.9, the thermal layer thickness decreases with decreasing gap size. Also, the temperature gradient close to the heated surface becomes smaller as the gap size diminishes. This is consistent with the heat transfer coefficient variation presented in Figure 7.6. In fact, the convective heat transfer coefficient is directly proportional to the temperature gradient at the surface. Figures 7.15, 7.17 and 7.18 display clearly that, as the gap size diminishes, the thermal layer is squashed.

The reduction of the gap size forces the heat to spread in the azimuthal direction rather than in the radial one. This would be assisted by the action of secondary flows, if such flows occur in a pattern similar to that near corners in channel flows.

Figure 7.12 shows that the mean temperature contours, when the heating element is at an angle $\phi_o = -45°$, are asymmetric, tending towards the narrow gap. This can be possibly attributed to the presence of lower convective velocities near the gap than near the subchannel center, thus permitting more extensive diffusion of heat by turbulent motions. A similar displacement of the θ' contours (Figure 7.19(a)) towards the gap can be explained by the same reasoning. On the other hand, θ' contours for $\phi_o = 5°$, show a shift away from the gap (Figure 7.19(b)). This could be attributed to the presence of secondary flows, which carry fluid near the

wall from the gap towards the center of the subchannel.

As the gap size diminishes, it is seen (Figure 7.17) that the temperature spreads more in the azimuthal direction, thus implying stronger secondary flows, in conformity with the results of Trupp and Aly [1979].

The pdfs presented in Figures 7.20 and 7.21 all deviated from the normal distribution and exhibited measurable skewness. This skewness can be explained by observing that the cold-wire signal (Figure 7.13) presents more peaks in the "hot side" than in the "cold side" of the mean. For higher radial positions, the signal corresponds to mostly unheated fluid with occasional "pockets" of hot fluid, which is in concordance with the radial increase of flatness (Figure 7.23).

As the gap size decreases the pdfs deviate more from Gaussianity and the skewness and flatness increase.

Chapter 9

Conclusions and Recommendations for Further Research

The main conclusions drawn from the results of the study on a roughly 12.9 upscale model of the CANDU reactor are listed below:

- The heat transfer coefficient presents relative minima at narrow gaps and maxima at open flow regions.
- The heat transfer coefficient has a distribution similar to but not identical with that of the wall shear stress.

- At small rod-wall proximities both the average and the gap local heat transfer coefficients are low. This implies that the wall temperature would tend to be higher than the design value.

- At W/D close to 1, a reduction in W/D results in an appreciable decrease in the heat transfer coefficient.

- The statistics of the flow temperature fluctuations deviate from those of the normal distribution.

- As the rod-wall gap diminishes, the pdf of the temperature fluctuations deviate more from Gaussianity and the skewness and flatness increase.

- The Corrsin microscales are nearly constant in the radial direction. However, they decrease with decreasing gaps.

- Some evidence for the presence of secondary flows was obtained from the temperature measurements, however this phenomenon requires further study.

Future continuation of the present experimental program is planned. It includes, in a first stage, the acquisition of additional mean and fluctuating temperature contours and the computation of temperature autocorrelations, spectra and integral scales. The cross-channel mixing will also be investigated by the localized injection of heated air. In a second stage,

temperature velocity correlations will be obtained, in an attempt to balance the heat transport equations and to test the applicability of various turbulence models.

Further exploration of analytical estimation of the heat transfer coefficient and temperature distributions is also planned.

References

Axford, R.A., 1967, Two dimensional multiregion analysis of temperature fields in reactor tube bundles, Nucl. Engng. Design, 6, p 25-42.

Barrow H., Hassan, A.K.A. and Avgerinos, C., 1984, Peripheral temperature variation in the wall of a noncircular duct, an experimental investigation, Int. J. Heat Mass Transfer, 27, p 1031-1037.

Berger, F.P. and Ziai, A., 1982, The effect of displacement and bowing in rod clusters on local heat transfer characteristics, Proc. Conf. "Gas Cooled Reactors Today", 3, p 217-222.

Berger, F.P, Erfan, A., Rapier, A.C. and Ziai, A., 1986, The effect on local heat transfer of bowing of pins in a cluster, Proc. 8^{th} Intl Heat Transfer Conf., San Francisco.

Bulew, N.I., 1962, Theoretical model of the mechanism of turbulent exchange in fluid flow, Report AERE-Trans. 957, English translation from: Teploperedacha, USSR Academy of Science, Moscow, p 64-98.

Bulew, N.I., 1964, Theoretical model for turbulent transfer in three-dimensional fluid flow, Paper n°329 presented at the 3^{rd} UN. Intern. Conf. on Peaceful Uses of Atomic Energy, Geneva.

Hojstrup, J., Rasmussen, K. and Larsen, S.E., 1976, Dynamic calibration of temperature wires in still air, DISA information 20,22, DISA Electronics,

Franklin lakes, New Jersey.

Hoffman, H.W., Kidd, G.J.Jr., Lynch, F.E., Stelzman, W.J., Wantland, J.L. and Sogin, H.H., 1970, Experimental studies of the heat transfer and fluid dynamic characteristics of rod-cluster-type nuclear reactor fuel elements, ORNL 4356 report.

Holman, J.P., 1981, Heat Transfer, McGraw-Hill.

Ingesson, L. and Hedberg, S., 1970, Heat transfer between subchannels in a rod bundle, 4th International Heat Transfer Conference, Vol3, p114-126.

Kakaç, S., Shah, R.K. and Aung, W., 1987, Handbook of Single Phase Convective Heat Transfer, Wiley-Interscience.

Karnik, U., 1988, Experiments on the structure of turbulence and the diffusion of heat from a line source in uniformly sheared flows, Ph.D. Thesis, University of Ottawa, Canada.

Kjellstrom, B., 1974, Studies of turbulent flow parallel to a rod bundle of triangular array, Report AE-487 AB Atomenergi, Sweden.

Meyder, R., 1975, Turbulent velocity and temperature distribution in the central subchannel of rod bundles, Nucl. Engng. Design, 35. 181-189.

Mohanty, A.K. and Sohoo, K.M., 1988, Turbulent flow and heat transfer in rod-bundle subchannels, Nucl. Engng. Design, 106, p 327-344.

Nijsing, R., Gargantini, I. and Eiffer, W., 1966, Analysis of fluid flow and heat transfer in a triangular array of parallel heat generating rods, Nucl. Engng. Design, 4, p375-398.

Ouma, B.H., 1988, Experiments in rod bundle subchannel flows with varying rod-wall proximity, M.A.Sc. Thesis, University of Ottawa, Ottawa, Ontario, Canada.

Palmer, L.D., Swanson, L.L., 1963, Measurments of heat transfer coefficients, friction factors and velocity profiles for air flowing parallel to closely-spaced rods, Int. Heat Transfer Conf. Boulder, Colorado, paper 63.

Patankar, S.V., 1980, Numerical Heat Transfer and Fluid Flow, Hemisphere.

Peattie, R., 1987, A simple, low-dift circuit for measuring temperatures in fluids, J. Phys. E:Sci Instrum. 20.

Petukhov, B.S. and Roisen, L.I., 1974, Generalized dependences for heat transfer in tubes of annular cross section, Teplofis. Vysokikh Temp., 12, p 565-569.

Prandtl, L., 1910, Z. Physik, 11, p 1072.

Ramm, H. and Johannsen, K., 1975, A phenomenological turbulence model an its application to heat transport in infinite rod arrays with axial turbulent flow, Heat Transfer.

Rehme, K., 1978, The structure of turbulent flow through a wall subchannel of a rod bundle, Nuclear Engineering and Design, 45, p 311-323.

Rehme, K., 1980, Turbulent momentum transport in rod bundles, Nuclear Design, 62, p 137-146.

Rehme, K., 1982, Distributions of velocity and turbulence in parallel flow along an asymmetric rod bundle, Nuclear Technology, 59, p 148-159.

Rehme, K., 1987, Convective Heat Transfer over Rod Bundles, ch 7, Handbook of Single Phase Convective Heat Transfer, editors: Kakaç, S., Shah, R.K. and Aung, W., Wiley-Interscience.

Reynolds, O., 1874, On the extent and action of the heating surface for steam boilers, Procedings of the Manchester Literary and Philosophical society, 14, p 7, Also in Papers on mechanical and physical subjects, Cambridge, 1890, 1, p 81.

Rogers, J.T. and Tahir, A., 1975, Turbulent interchange mixing in rod bundles and the role of secondary flows, ASME paper n°75-HT31.

Rogers, J.T. and Tahir, A., 1979, The mechanism of secondary flows in turbulent interchange in rod bundles, 7^{th} Canadien Congress of Applied Mechanics, Sherbrooke, Canada.

Seale, W.J., 1979, Turbulent diffusion of heat between connected flow passages, Nucl. Engng. Design, 54, p 183-195.

Seale, W.J., 1979, Turbulent diffusion of heat between connected flow passages, Nucl. Engng. Design, 54, p 197-209.

Seale, W.J., 1981, The effect of subchannel shape on heat transfer in rod bundles with axial flow, Int. J. Heat Mass Transfer, 24, p 768-770.

Sutherland, W.A., Kays, W.M., 1966, Heat transfer in parallel rod arrays, Journal of Heat Transfer, Trans. ASME.

Tavoularis, S., 1978, Experiments in turbulent transport and mixing, Ph.D Thesis, The Johns Hopkins University, Baltimore, Maryland, USA.

Taylor, G.I., 1916, Conditions at the surface of a hot body exposed to the wind, Technical Report, Advisory Commitee for Aeronautics, 2, Reports and Momoranda n°272, p 423.

Trupp, A.C. and Azad, R.S., 1975, The structure of turbulent flow in triangular array rod bundles, Nuclear Engin and Design, 32, p 47-84.

Trupp, A.C and Aly, A.M.M., 1979, Predicted Secondary Flows in Triangular Array Rod Bundles, Trans. ASME 101, p 354.

Von Karman, T.J., 1939, The analogy between fluid friction and heat transfer, Trans. Am. Soc. Mech. Engns, 61, p 705-710.

	$h_a(W/m^2K)$		
ϕ \ W/D	1.149	1.089	1.030
....0.....	174.12	170.51	169.17
30.	174.68	169.30	165.79
60.	175.63	174.97	171.33
90.	178.06	174.47	175.12
120.	177.92	181.98	178.80
150.	183.84	184.73	-
180.	184.83	187.50	180.74
210.	184.68	185.21	-
240.	182.74	183.59	178.84
270.	181.26	176.44	176.47
300.	178.65	176.51	175.87
330.	174.27	169.97	164.49

Table 7.1: Measurements of the apparent heat transfer coefficient

Table 7.1: continued

ϕ_o (deg)	h_a W/m^2K
15.	133.29
40.	159.07
60.	174.29
135.	182.06
180.	183.72
214.	183.28
270.	178.42
300.	167.69
348.5	134.04

W/D=1.0 (Rod-wall contact)

ϕ_o (deg)	h_a W/m^2K
13.	130.06
31.	140.43
55.	150.74
61.	153.45
68.	151.65
87.	135.12
154.	181.47
174.	184.02
232.5	181.81
287.	179.25

Rod-rod-wall contact position

W/D	h_a W/m^2K
1.015	158.56
1.030	164.47
1.045	168.01
1.059	168.06
1.074	170.50
1.089	171.90
1.104	172.92
1.119	173.55
1.134	174.17
1.149	174.11

With varying W/D
minimum rod-wall gap

W/D	$\hat{h}_a$ W/m^2K	$\hat{h}_c/\hat{h}_a$	position
1.149	179.4	.597	design position
1.089	178.5	.595	
1.030	175.1	.595	
1.000	165.2	.593	rod-wall contact
1.000	152.3	.570	rod-rod-wall contact

Table 7.2: Average apparent heat transfer coefficient

METHOD	h (w/m^2k)
h_a	174
h_c	104
Reynolds analogy (equ:3.13)	67
Prandtl analogy (equ:3.15)	74
Von Karman analogy (equ:3.16)	83
Palmer and Swanson correlation[1]	61
Dittus and Boelter correlation for smooth tubes[2]	66

1) $\frac{f}{2} = St\ Pr^{\frac{2}{3}}$

2) $Nu_d = 0.023\ Re_d^{0.8}\ Pr^{0.4}$

Table 7.3 Comparison of h_a and h_c with different analogies and correlations

PARAMETER	UNITS	REACTOR BUNDLE	MODEL
Operating fluid	-	Heavy water	Air
Fluid temperature	°C	220-240	25-28
Fluid pressure	MPa	13.79	Atmospheric
Bundle length	m	0.50	6.10
Rod diameter	mm	13.08	168.27
Pitch to diameter ratio, P/D	-	1.14	1.14 at design
Hydraulic diameter	mm	7.85	55.58
Reynolds number	-	450,000	74,000
Flow obstructions	-	Upstream bundle, endplates, rod spacers	side walls
Heating	-	All rods heated	heated strip on central rod

Table 8.1 Comparison between actual bundle and model

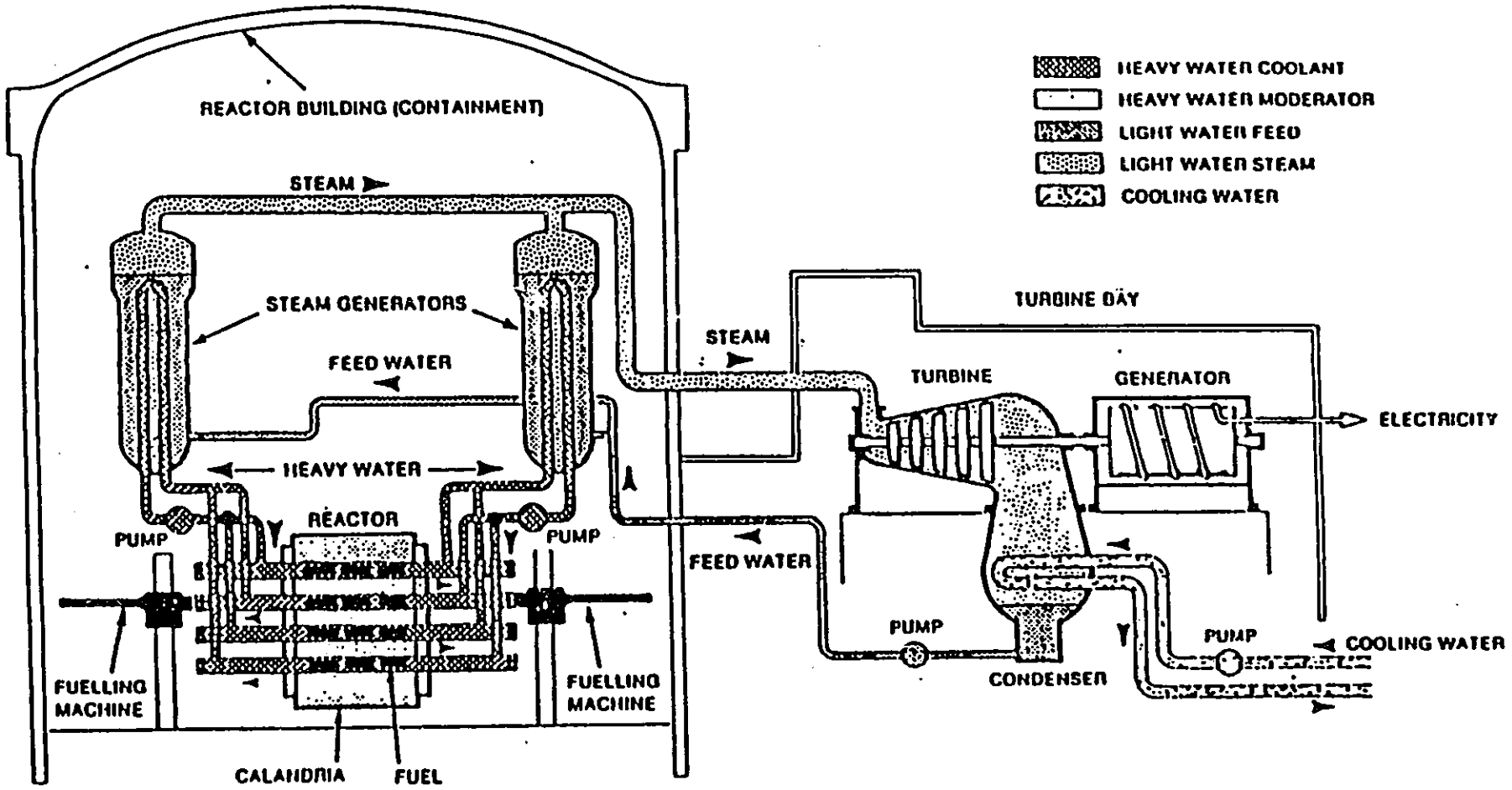

Figure 1.1: CANDU nuclear power system

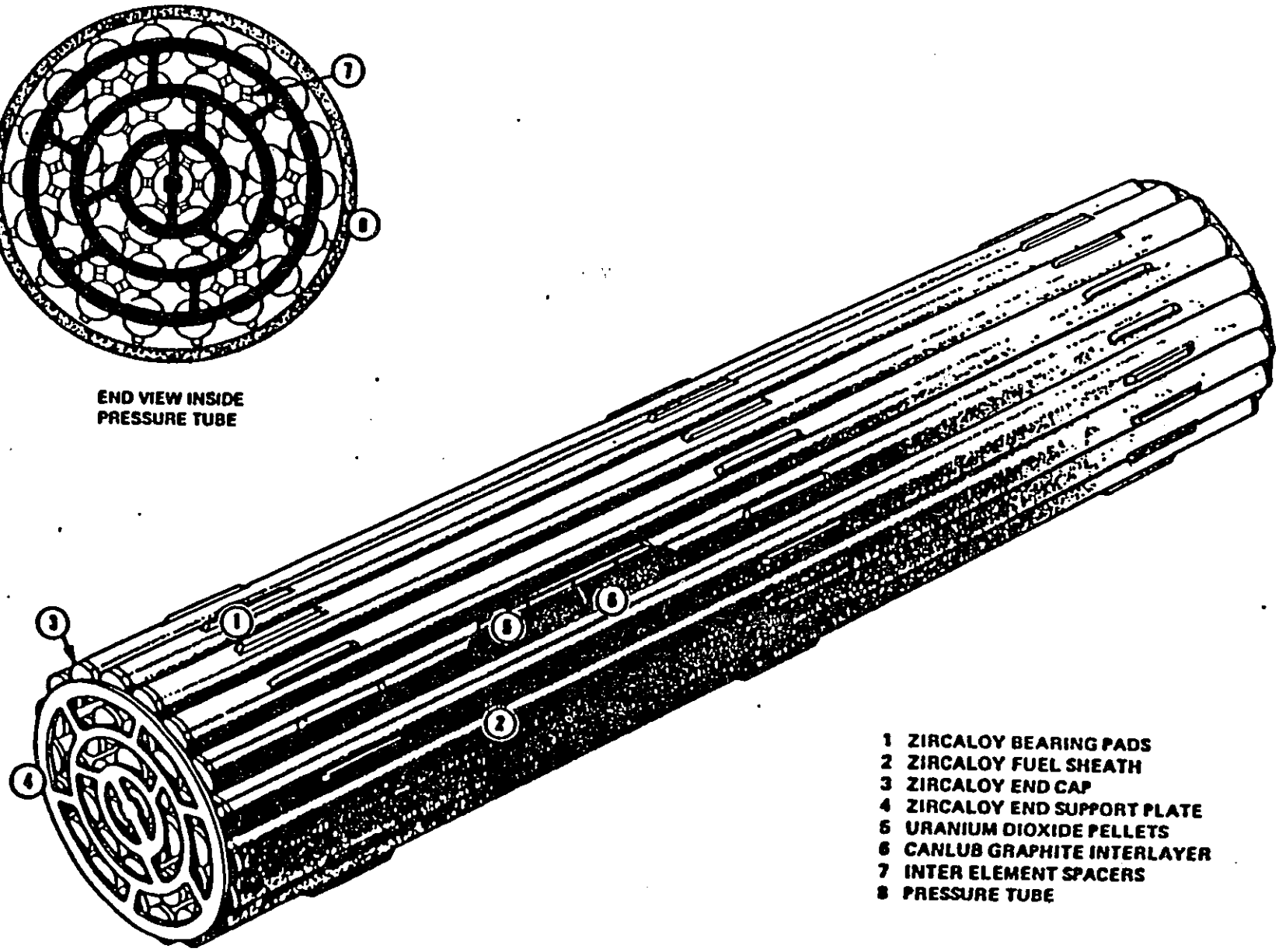

Figure 1.2: 37-rod element reactor bundle

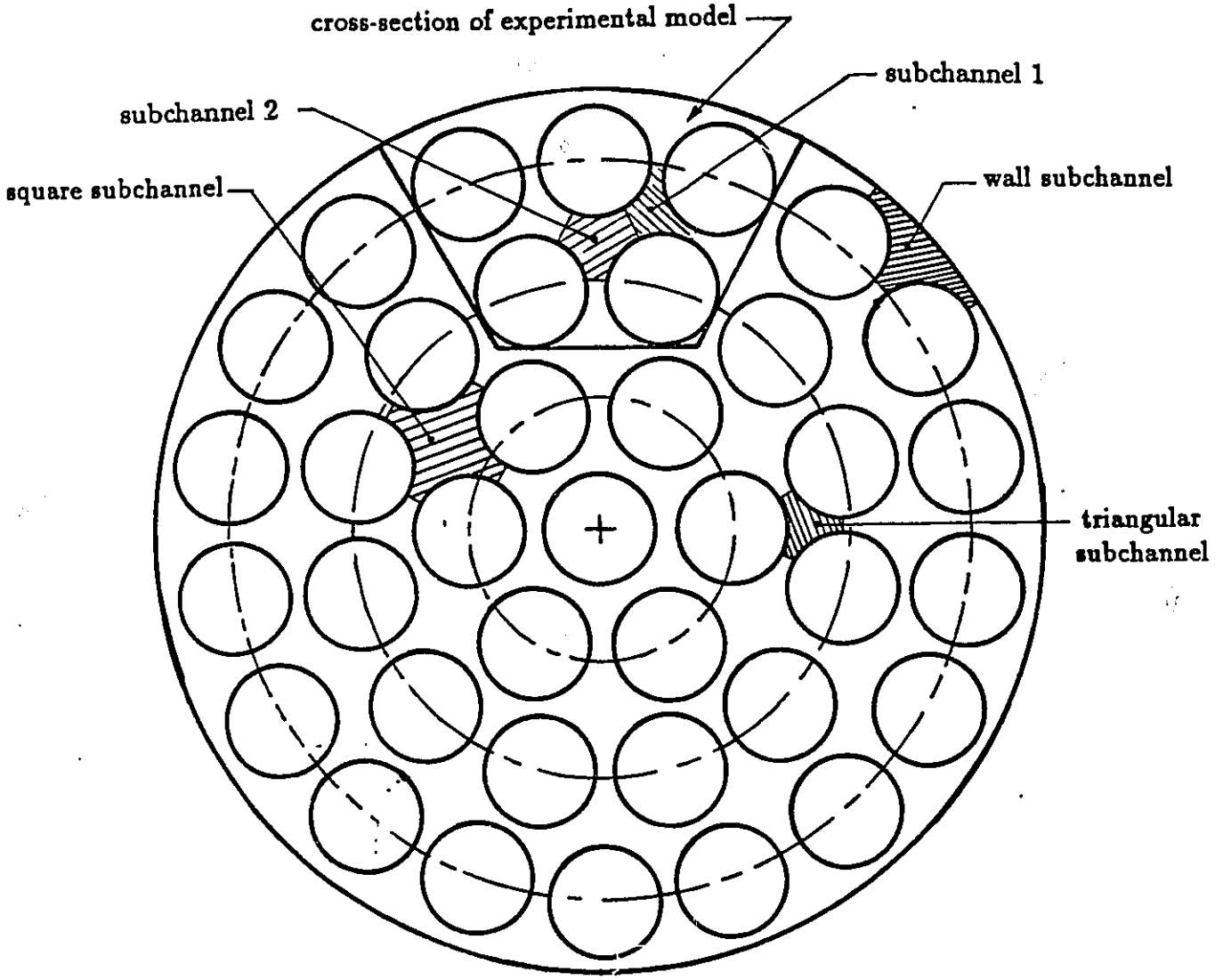

Figure 3.1: Cross-section of a 37-rod CANDU reactor bundle.

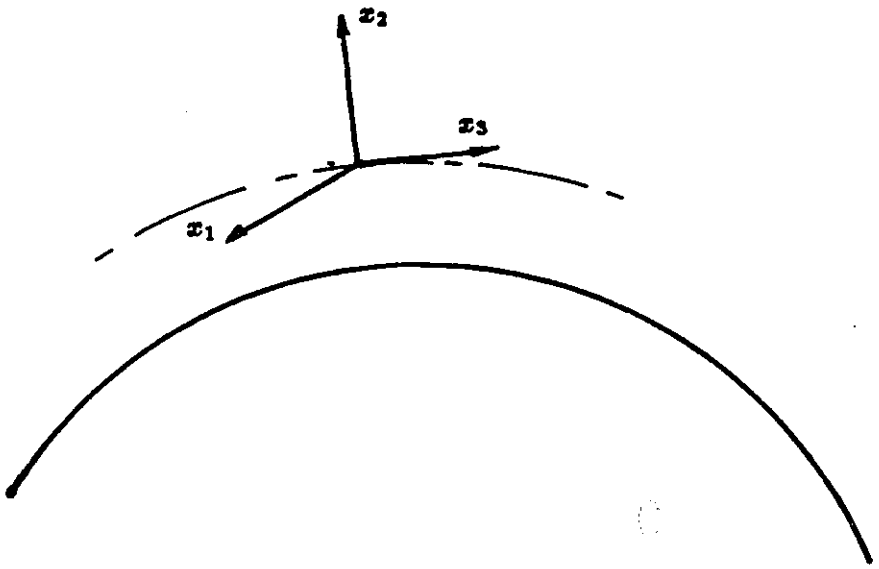

Figure 3.2: Coordinate system for velocity.

1-FLOW SECTION
2-PRESSURE BOX
3-FAN
4-SUPPORT
5-HORIZONTAL ROD-TRAVERSING MECHANISM
6-VERTICAL ROD-TRAVERSING MECHANISM
7-AIR FILTER

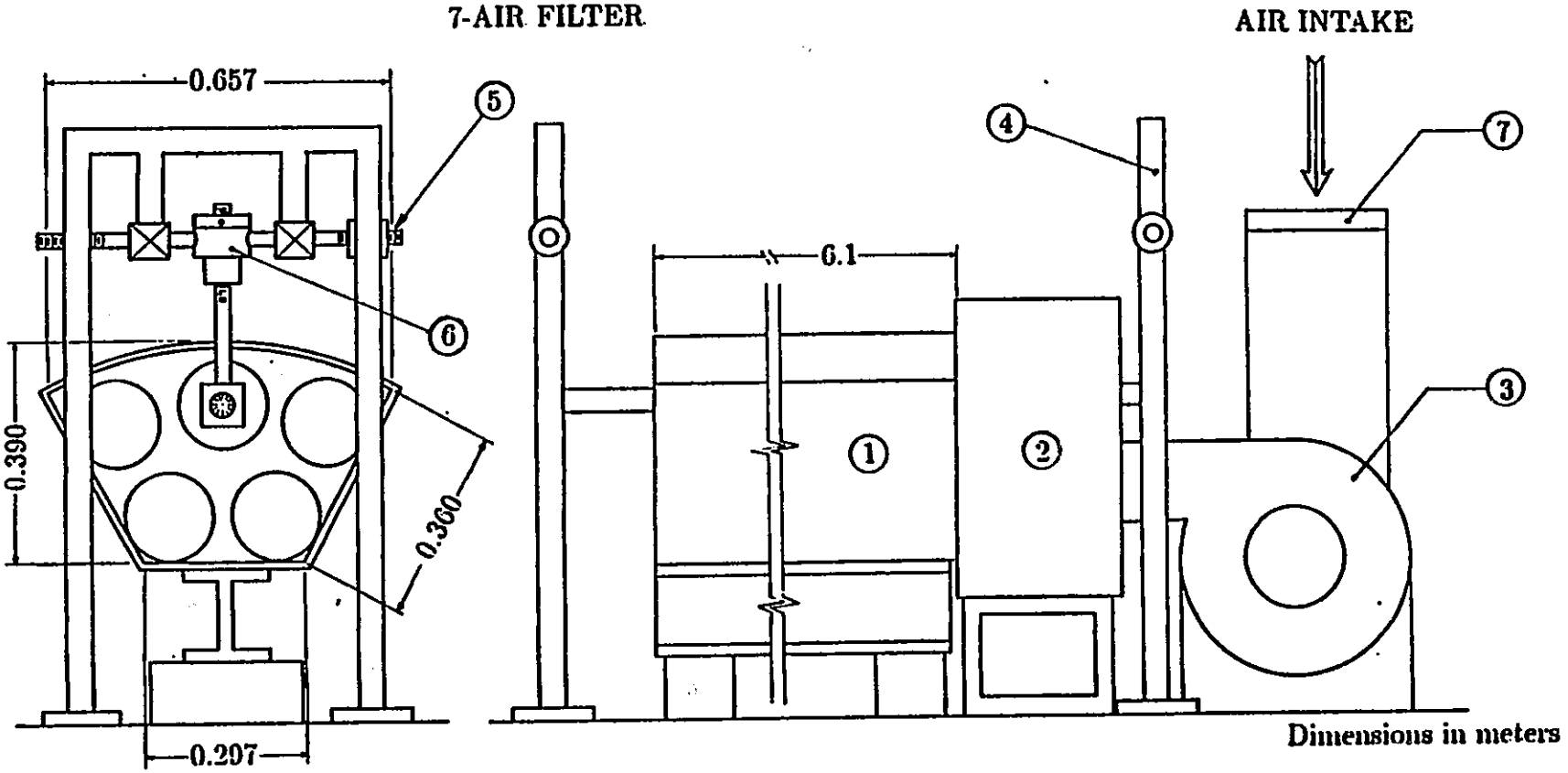

Figure 4.1: Sketch of the flow facility

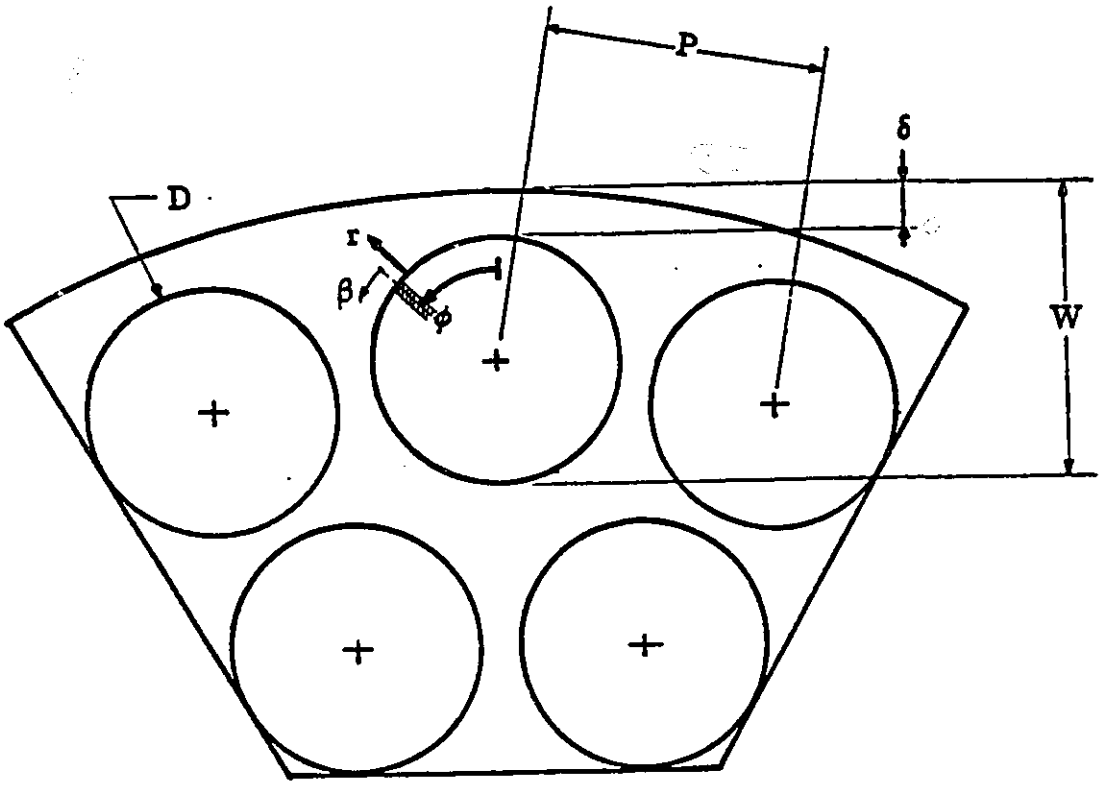

Figure 4.2: Cross-section of the model bundle facility (x-axis outwards)

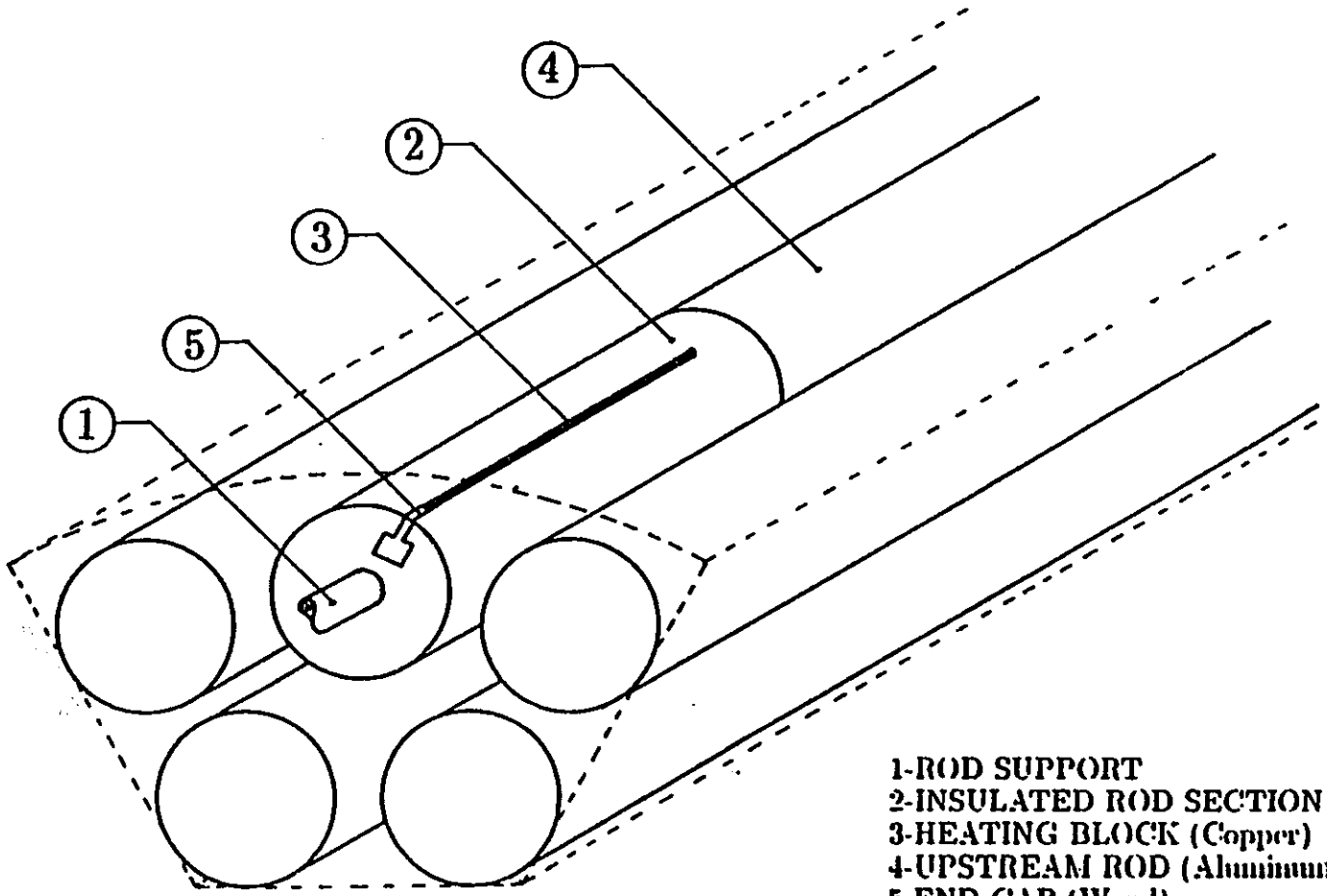

Figure 4.3: Position of the heated rod section

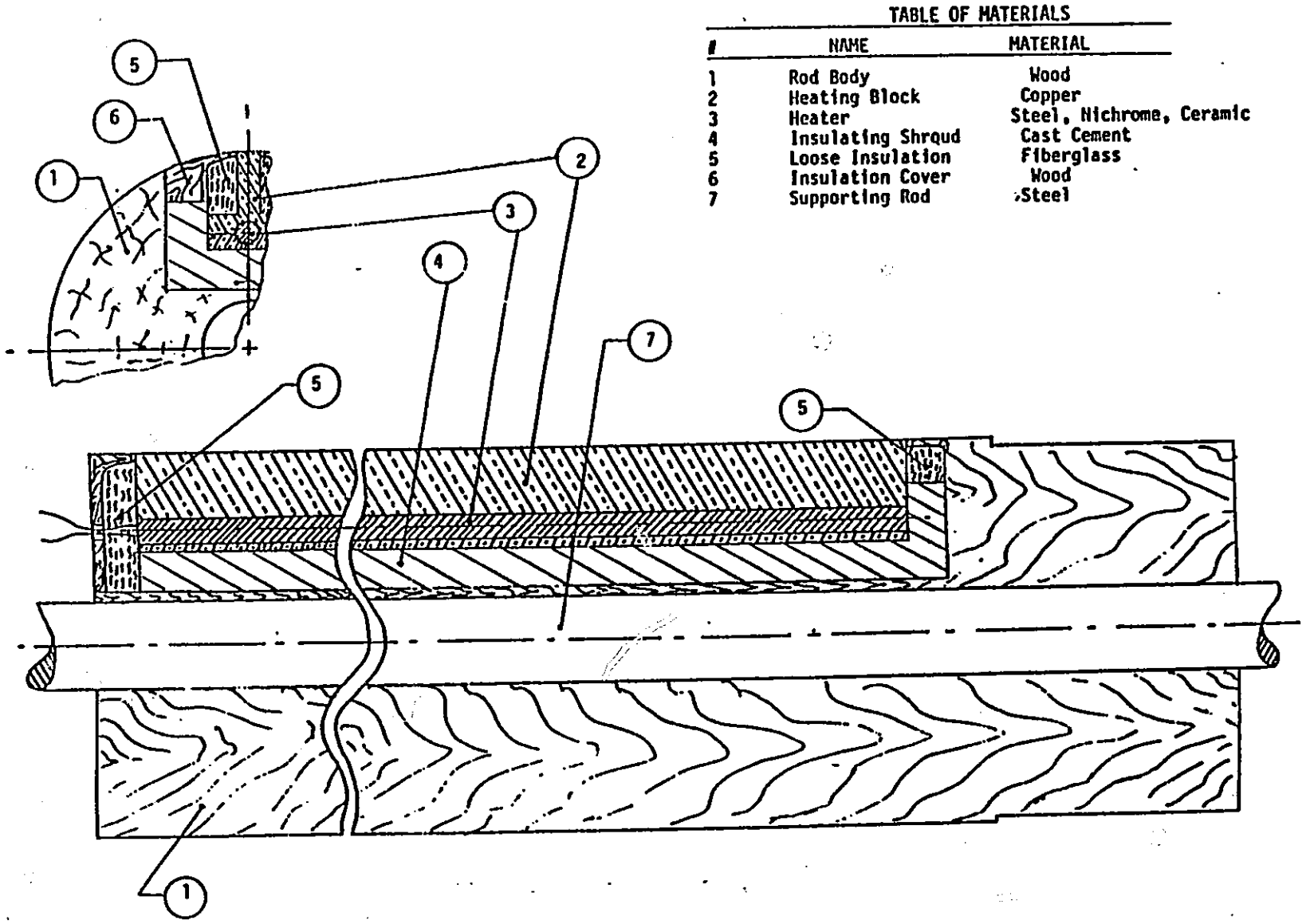

Figure 4.4: Assembly drawing of the heated rod section

All dimensions in mm.

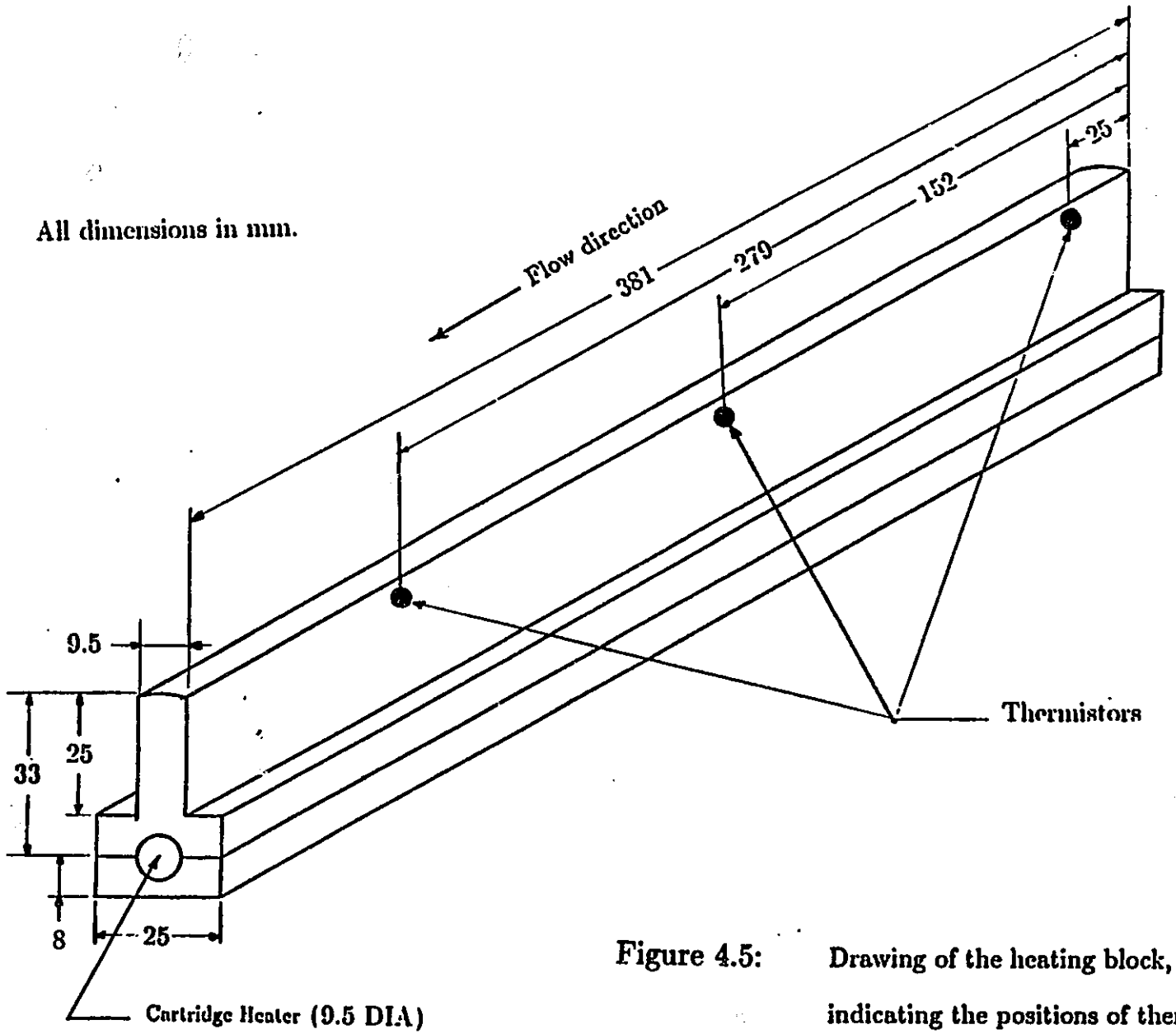

Figure 4.5: Drawing of the heating block, also indicating the positions of thermistors.

All dimensions in mm.

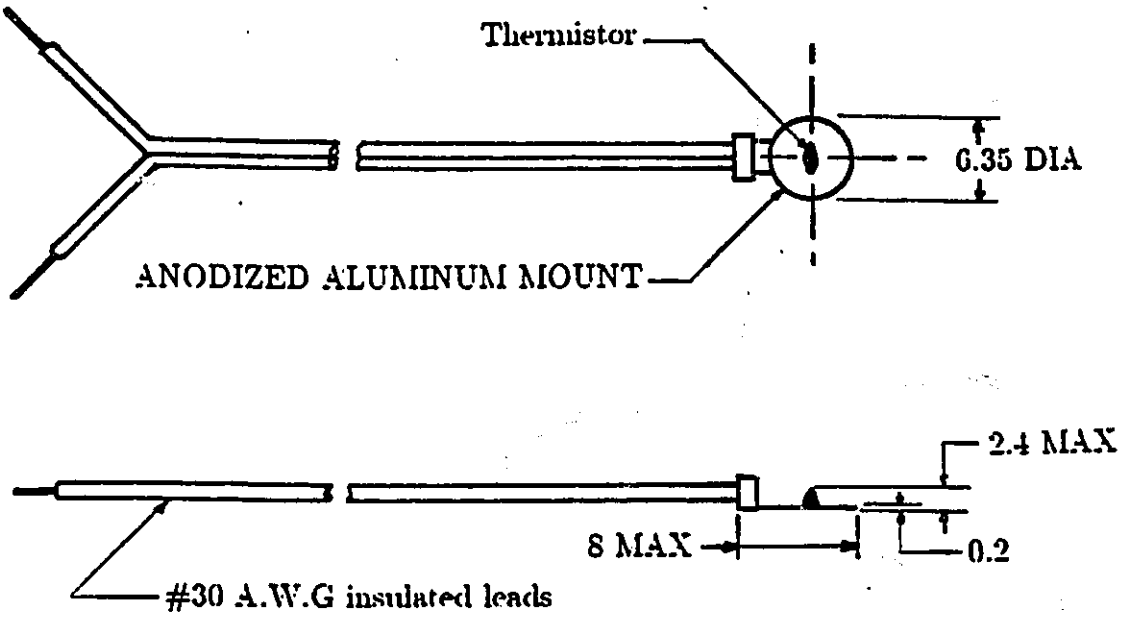

Figure 4.6: Sketch of a thermistor assembly

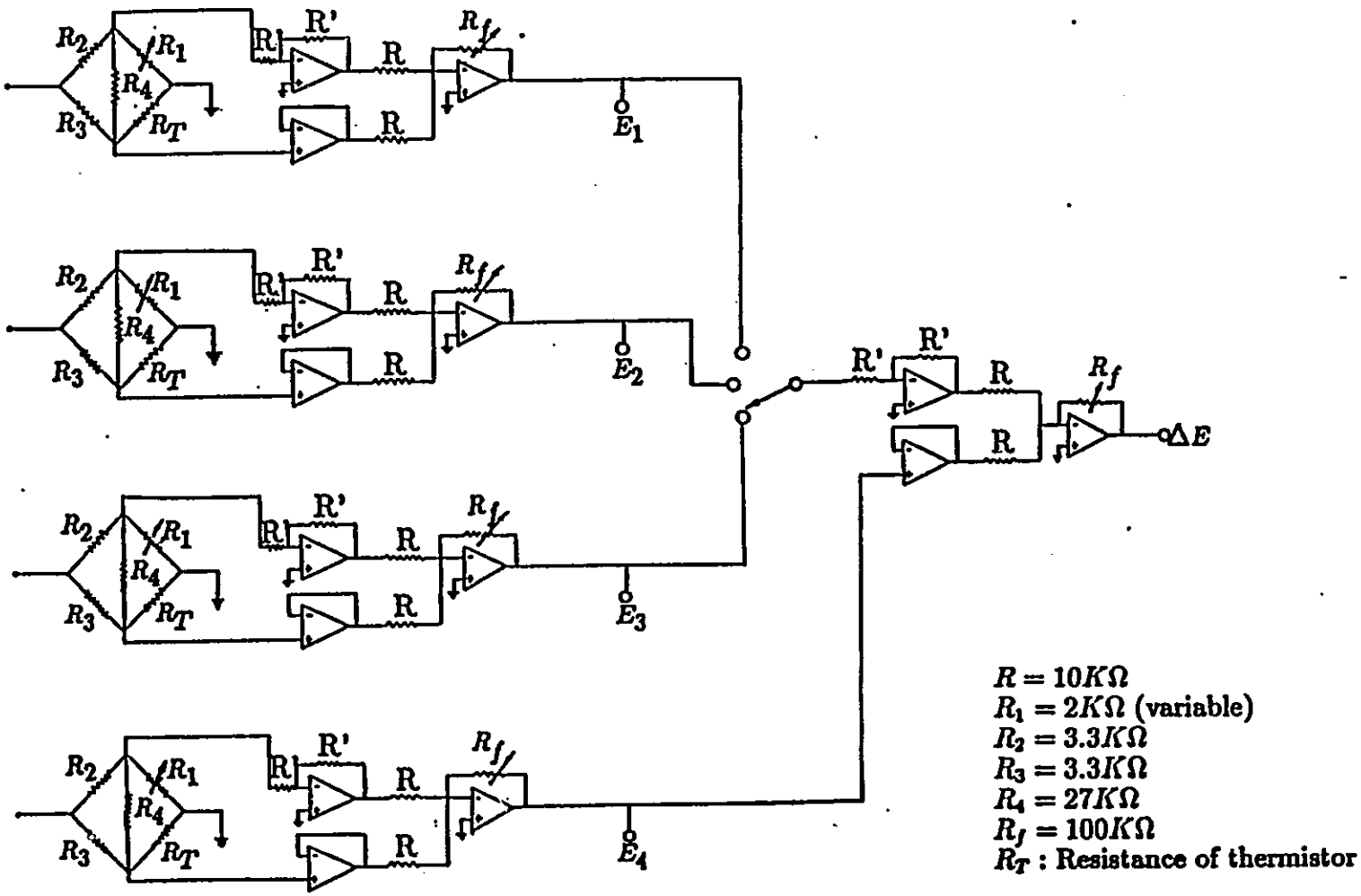

Figure 4.7: Thermistor electronic circuits

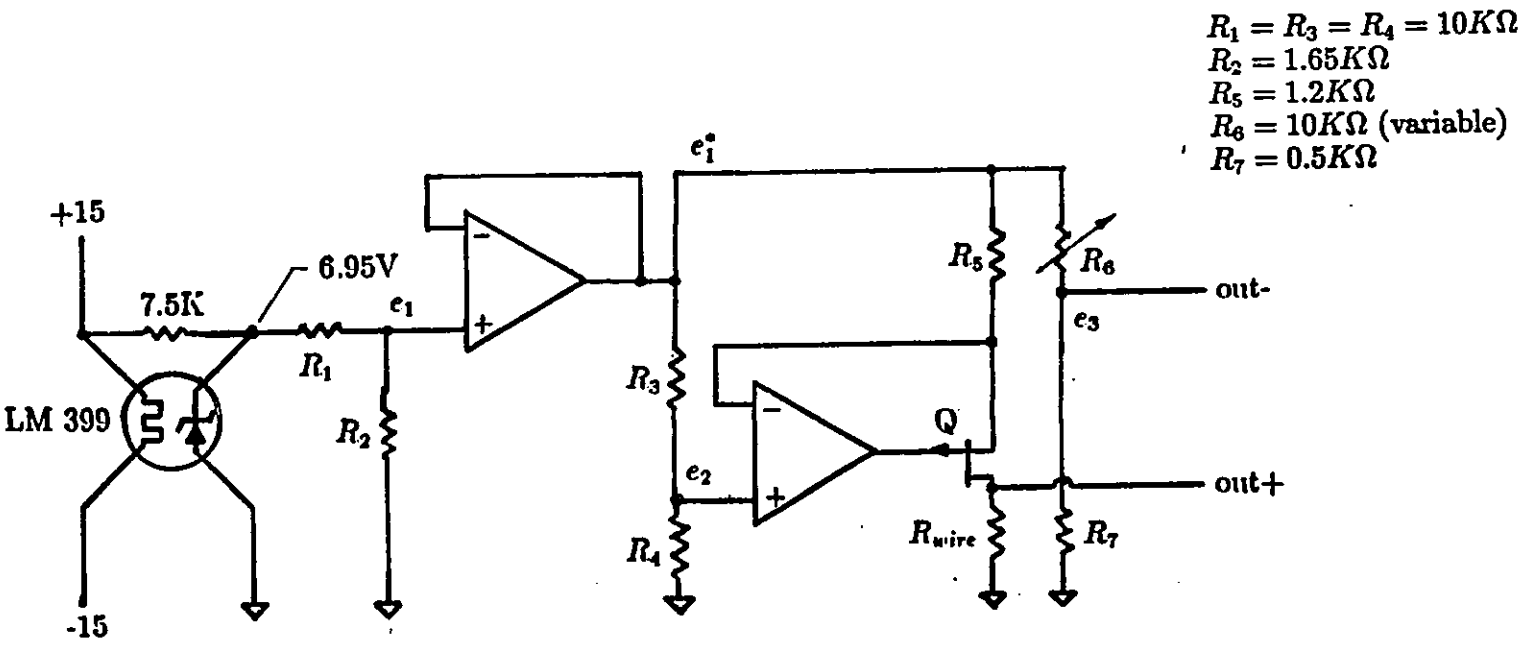

Figure 4.8: Constant current circuit diagram.

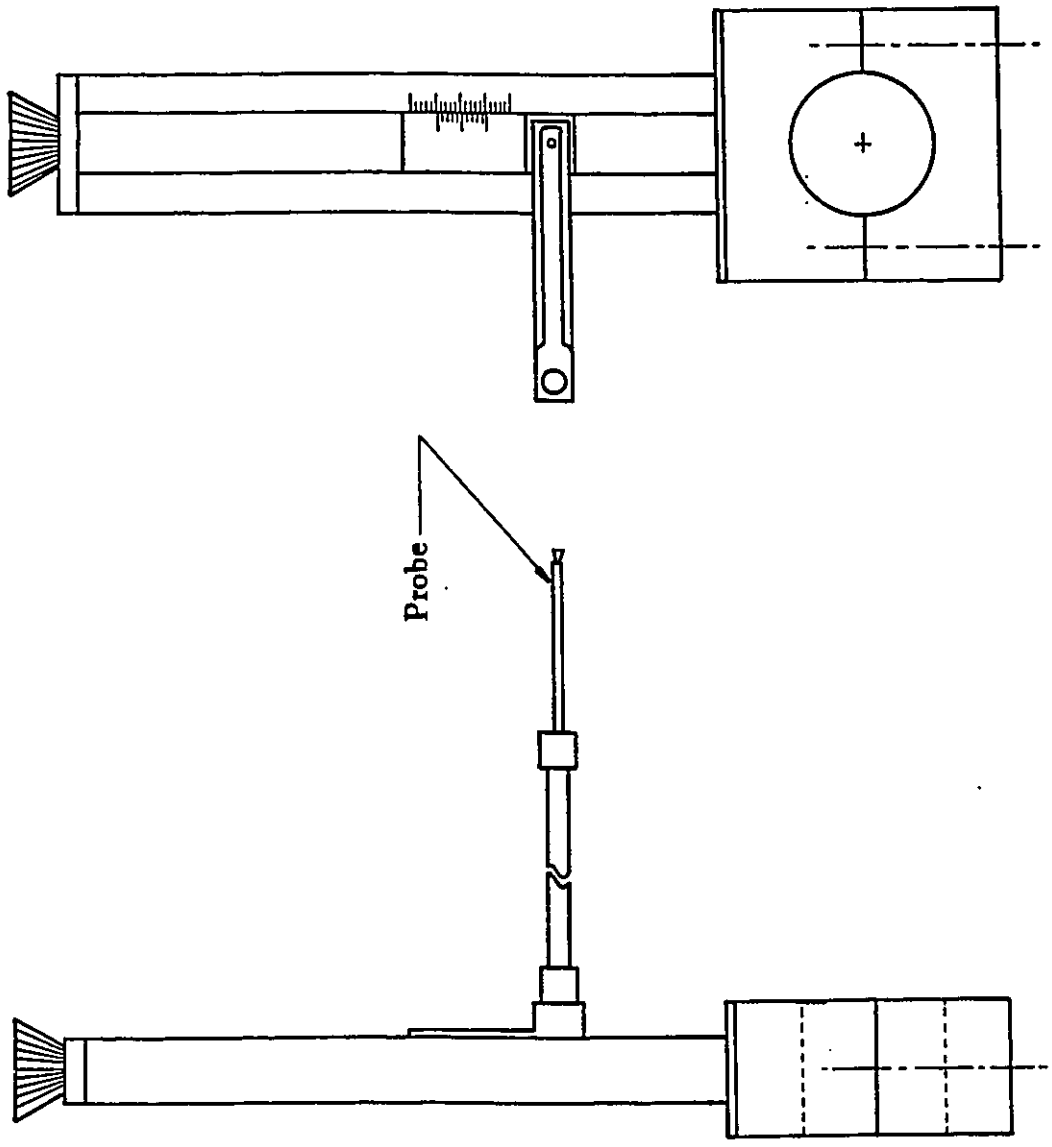

Figure 4.9: Probe traversing mechanism.

All dimensions in mm.

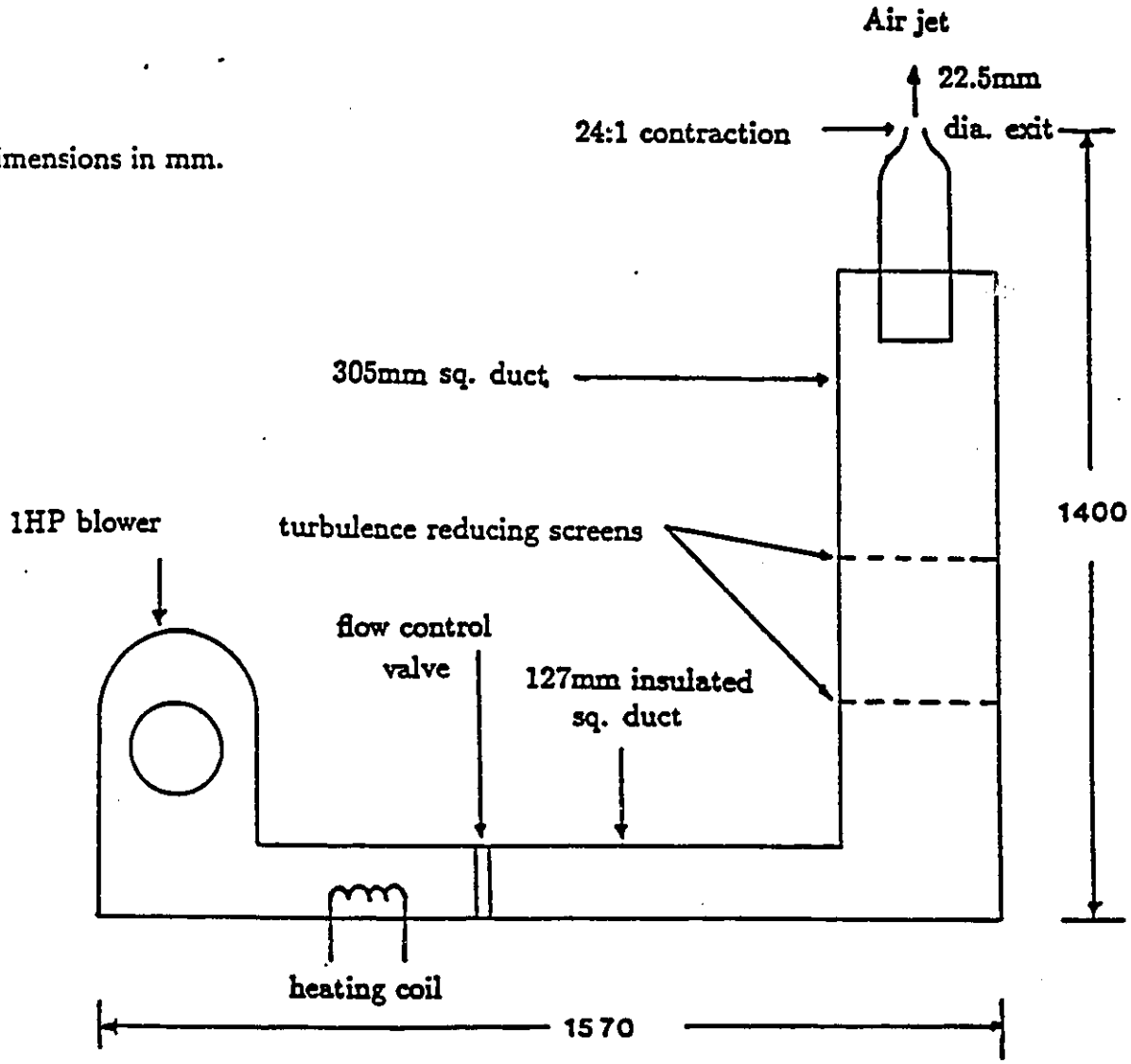

Figure 4.10: The Calibration jet (Karnik [1988])

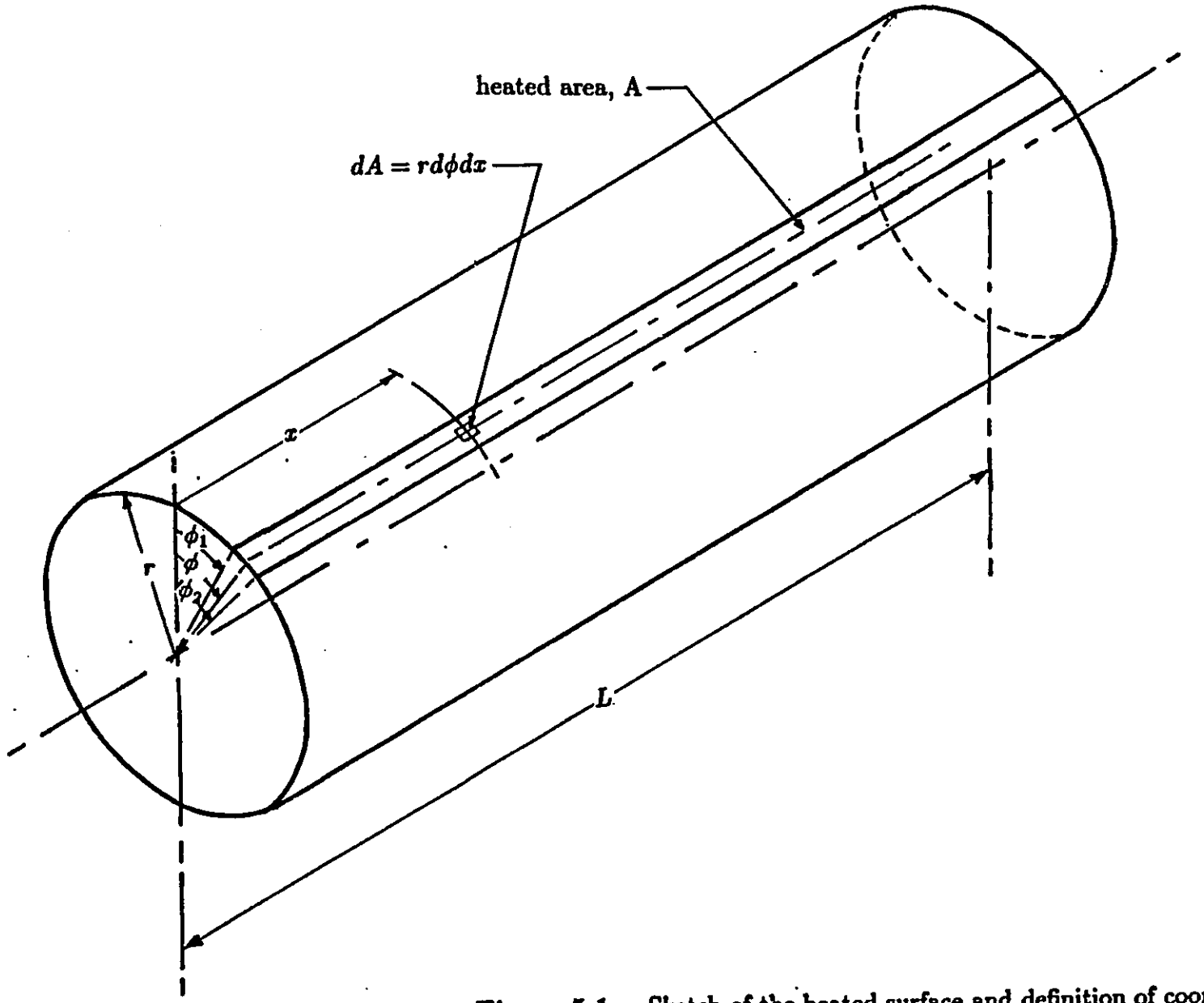

Figure 5.1: Sketch of the heated surface and definition of coordinates

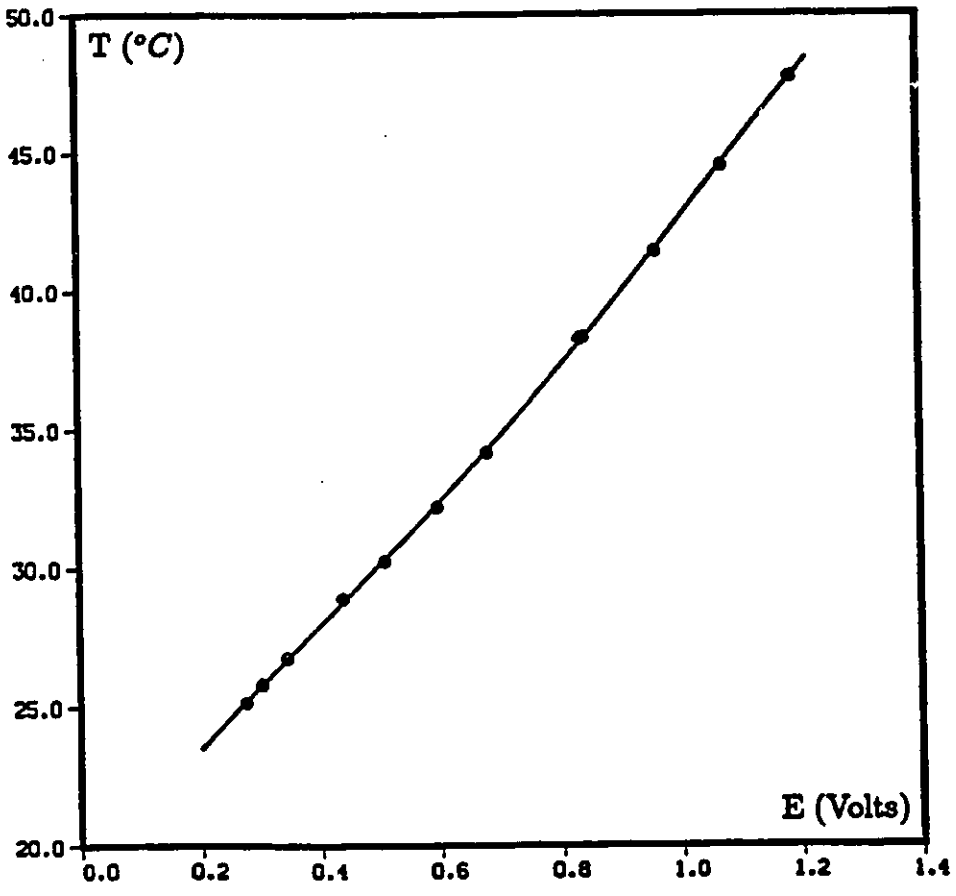

Figure 5.2: Typical thermistor calibration curve

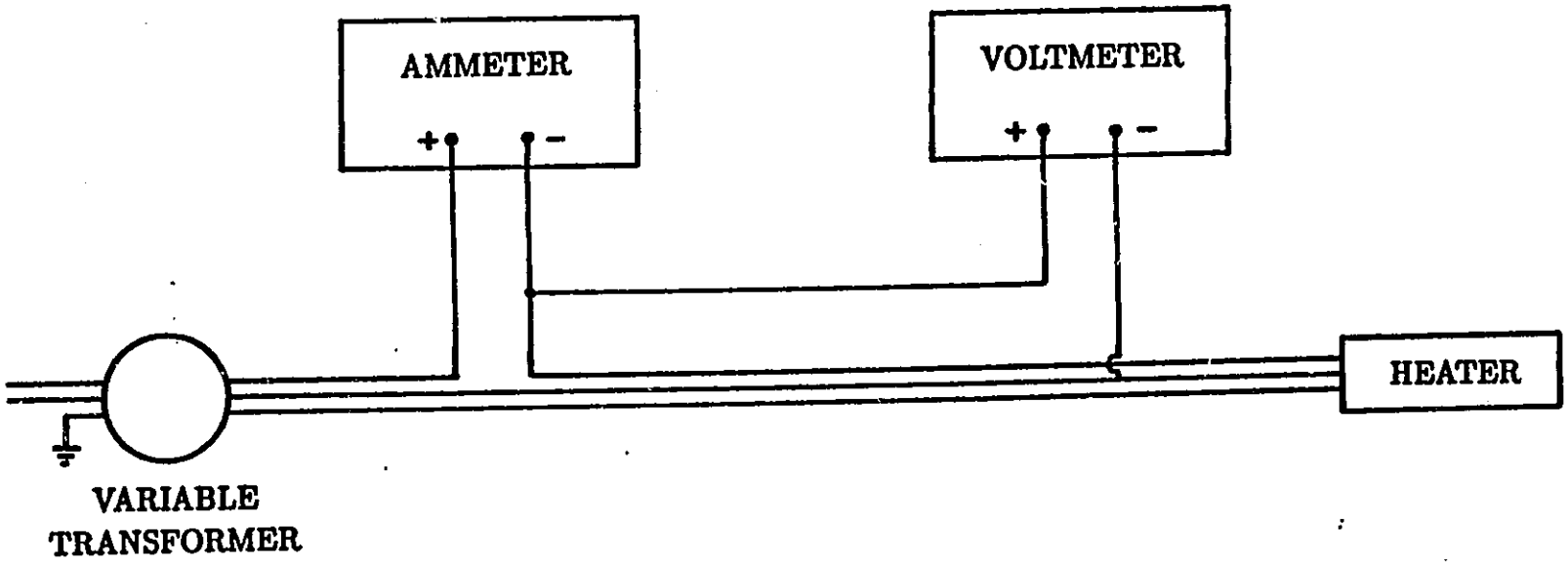

Figure 5.3: Set up for the measurement of the power input to the heater

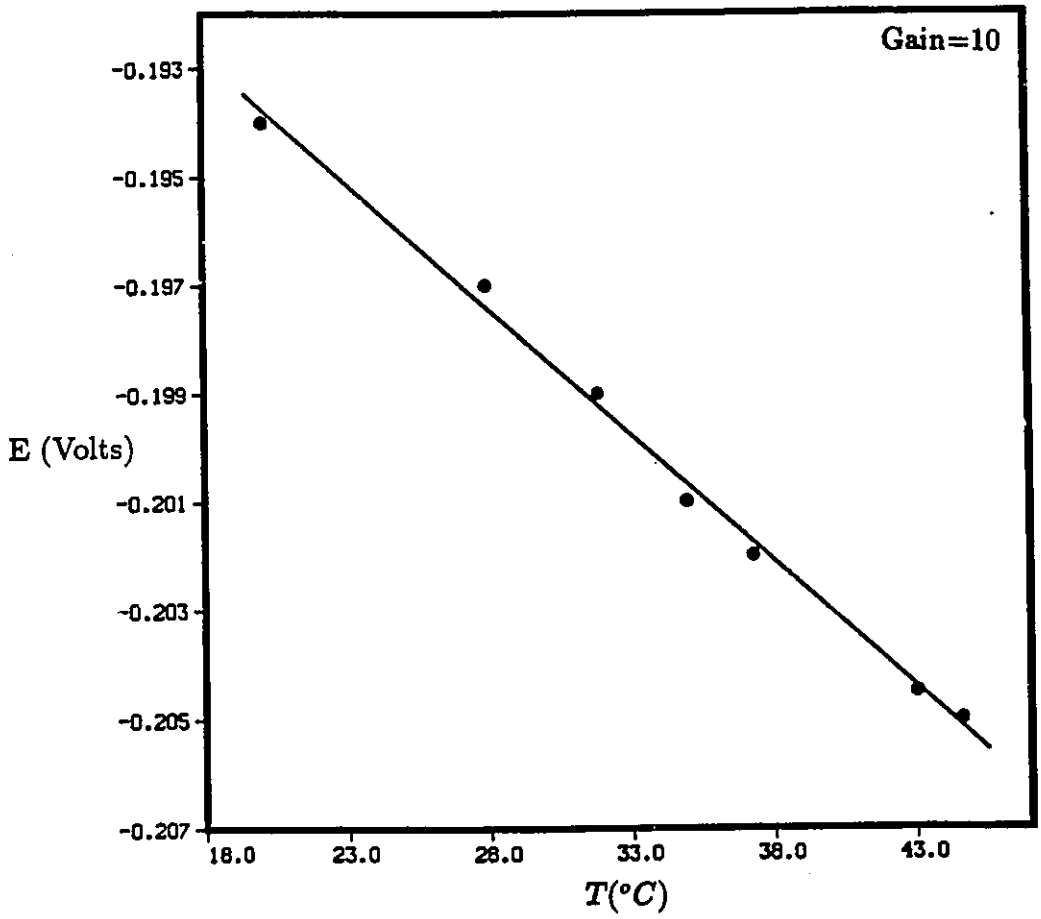

Figure 5.4: Typical cold wire calibration curve

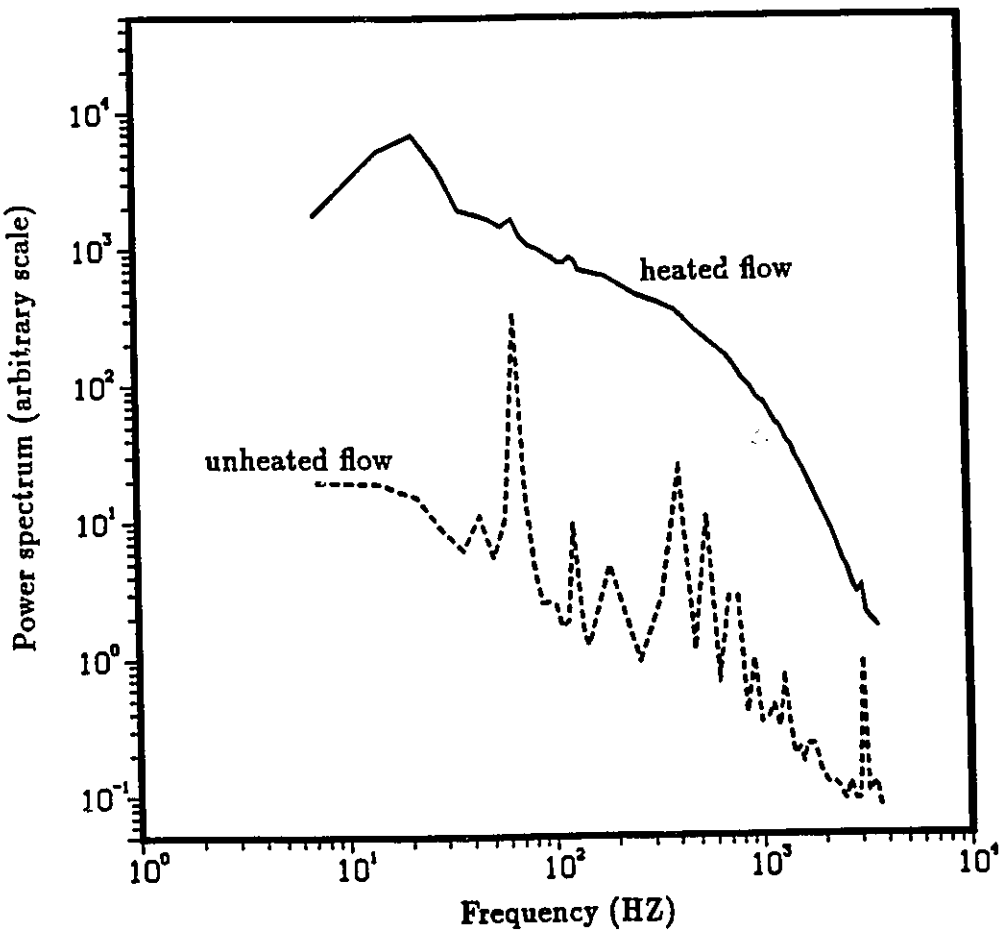

Figure 5.5: Power spectrum of the cold-wire signal in the heated and unheated flow.

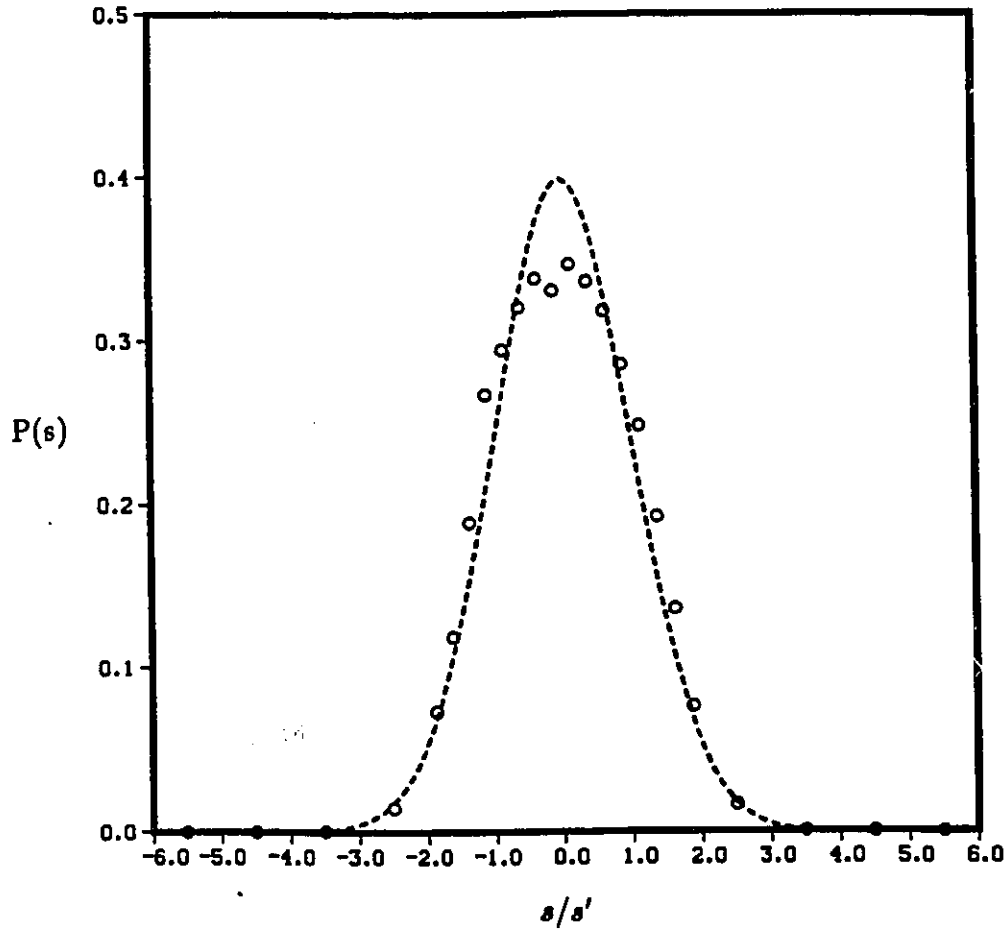

Figure 5.6: Probability density function of the cold wire signal in the unheated flow.

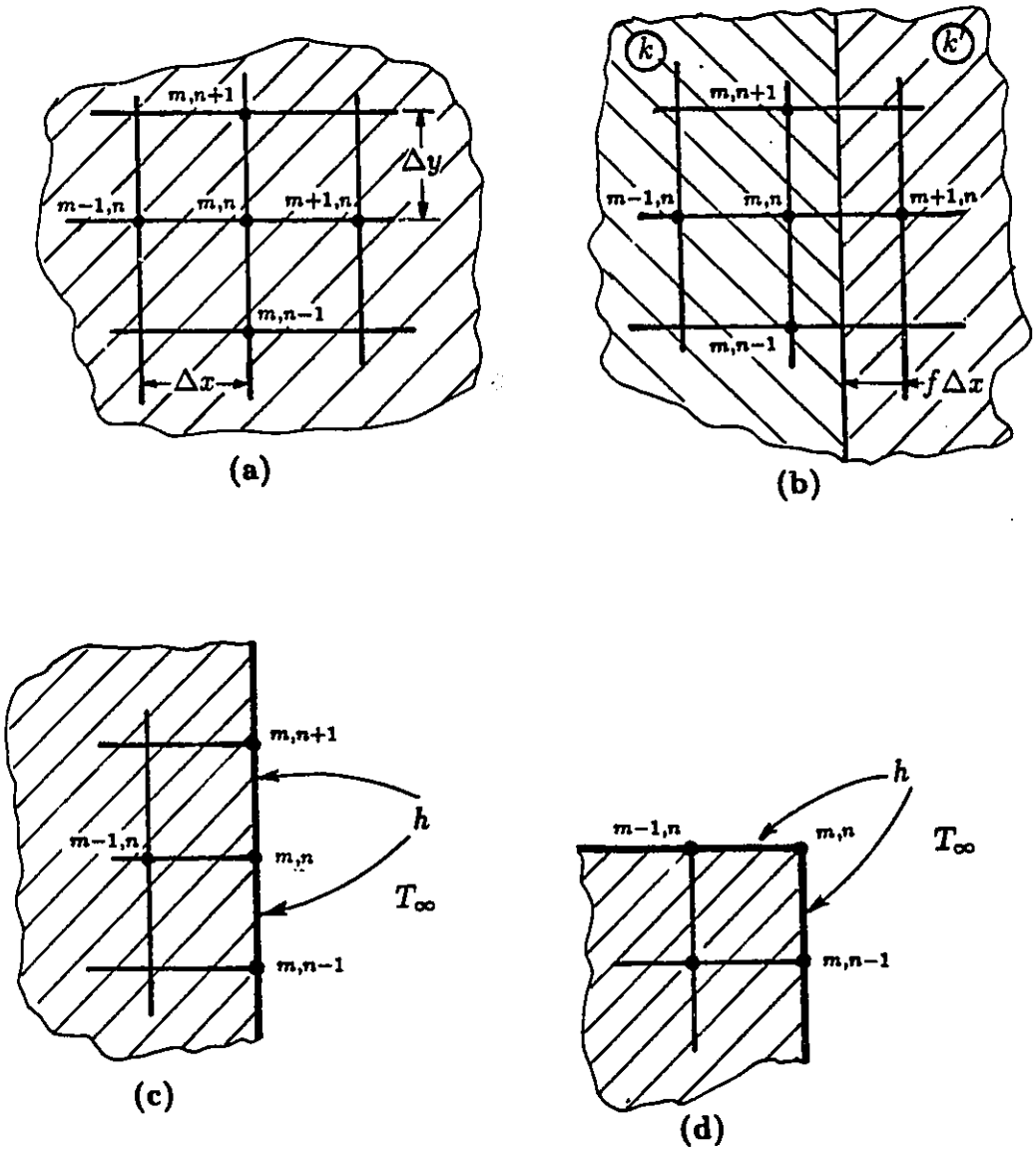

Figure 6.1: Nomenclature used in finite difference technique (a) interior node, (b) composite wall, (c) convective boundary node and (d) corner node with convection boundary.

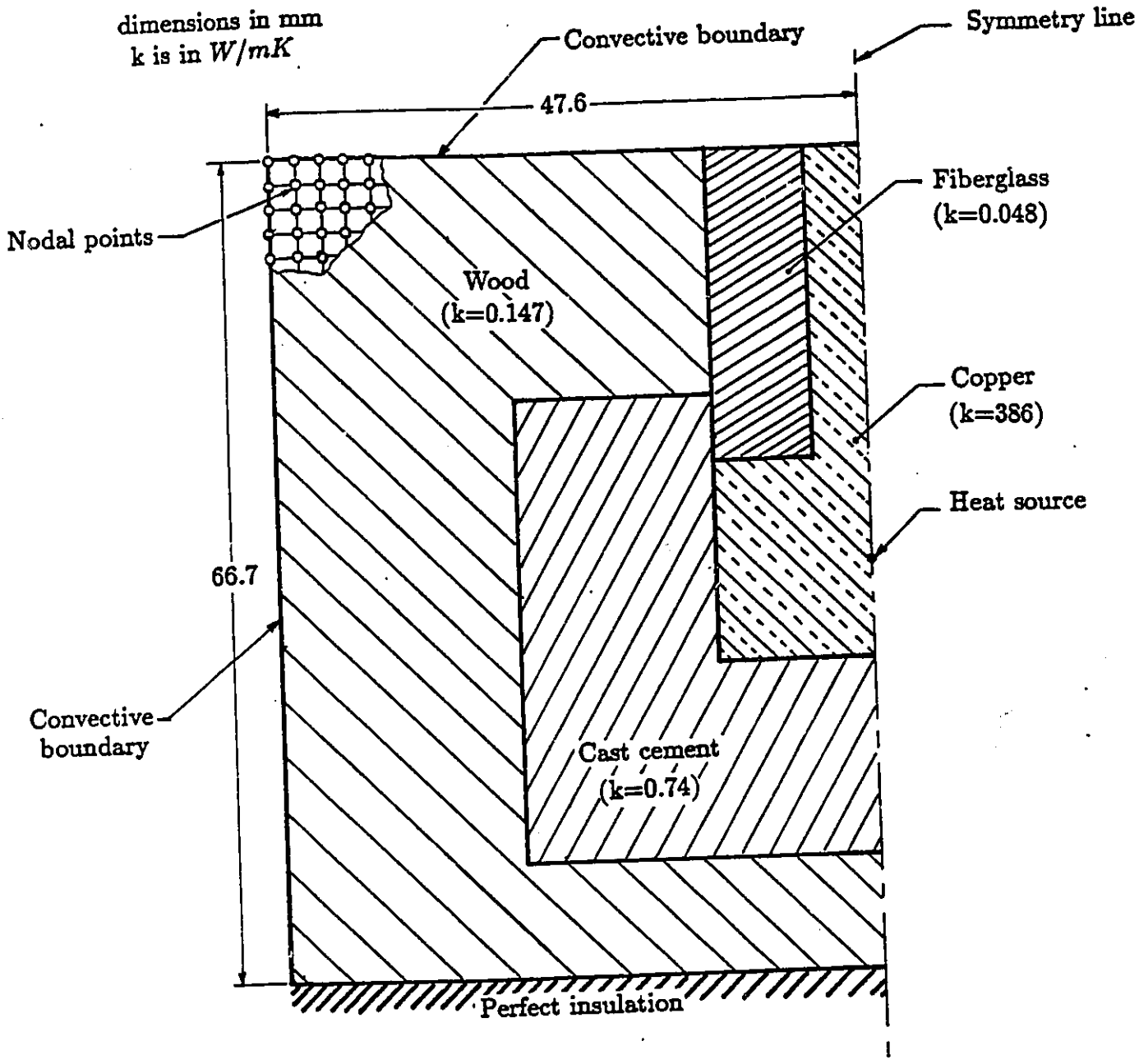

Figure 6.2: Heated section geometry used in the numerical analysis.

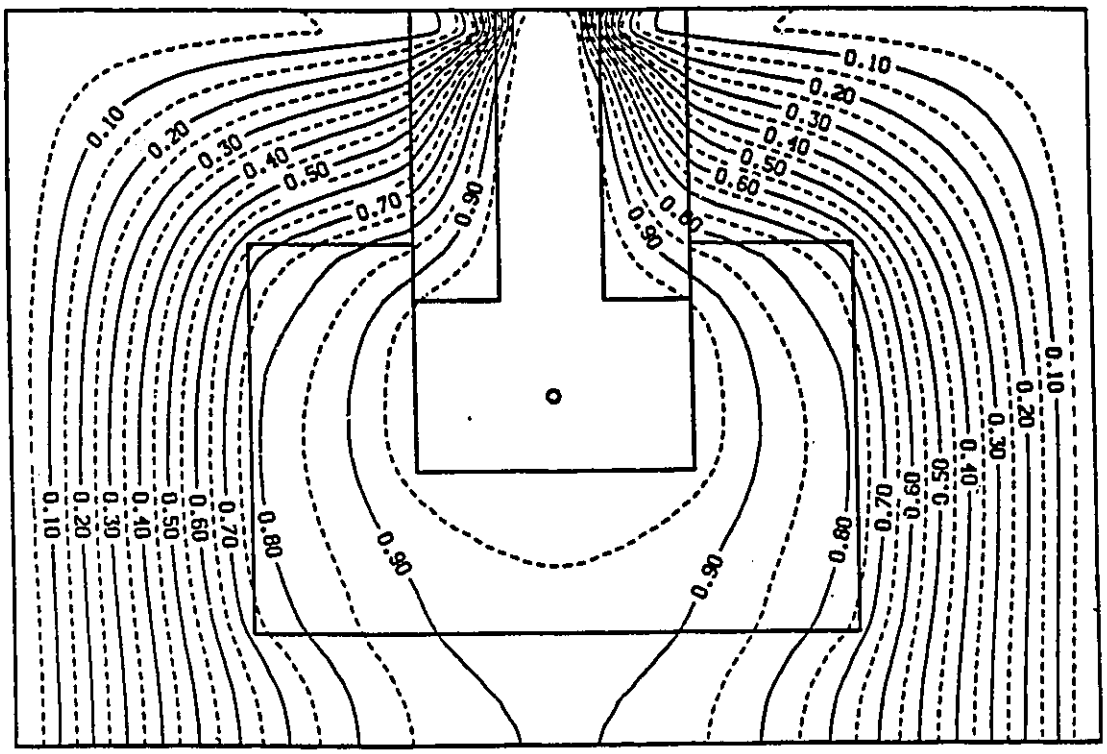

Figure 6.3: Isotherm contours $\frac{T - T_\infty}{T_{max} - T_\infty}$

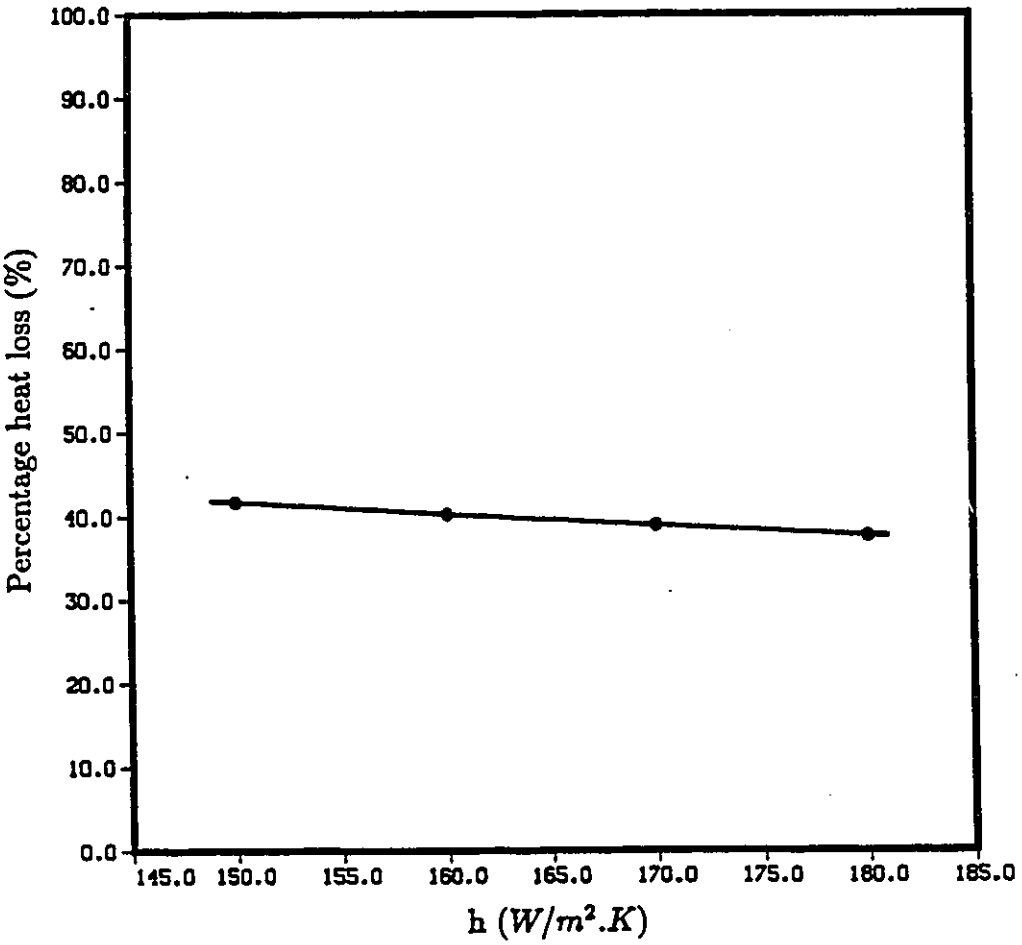

Figure 6.4: Heat losses variation with heat transfer coefficient

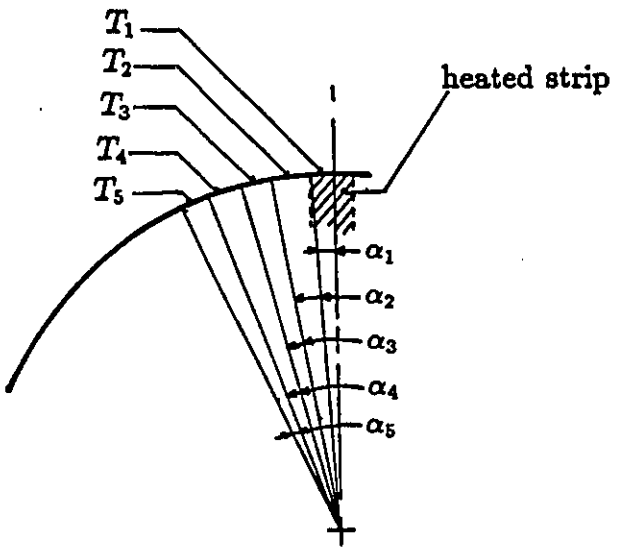

Free stream temperature: $T_\infty = 29.8°C$

i	α_i	T_i
1	3.25	44.6
2	6.75	32
3	5	31.5
4	5	31.1
5	5	30.6

Figure 6.5: Heat loss estimation from peripheral wall temperature measurements

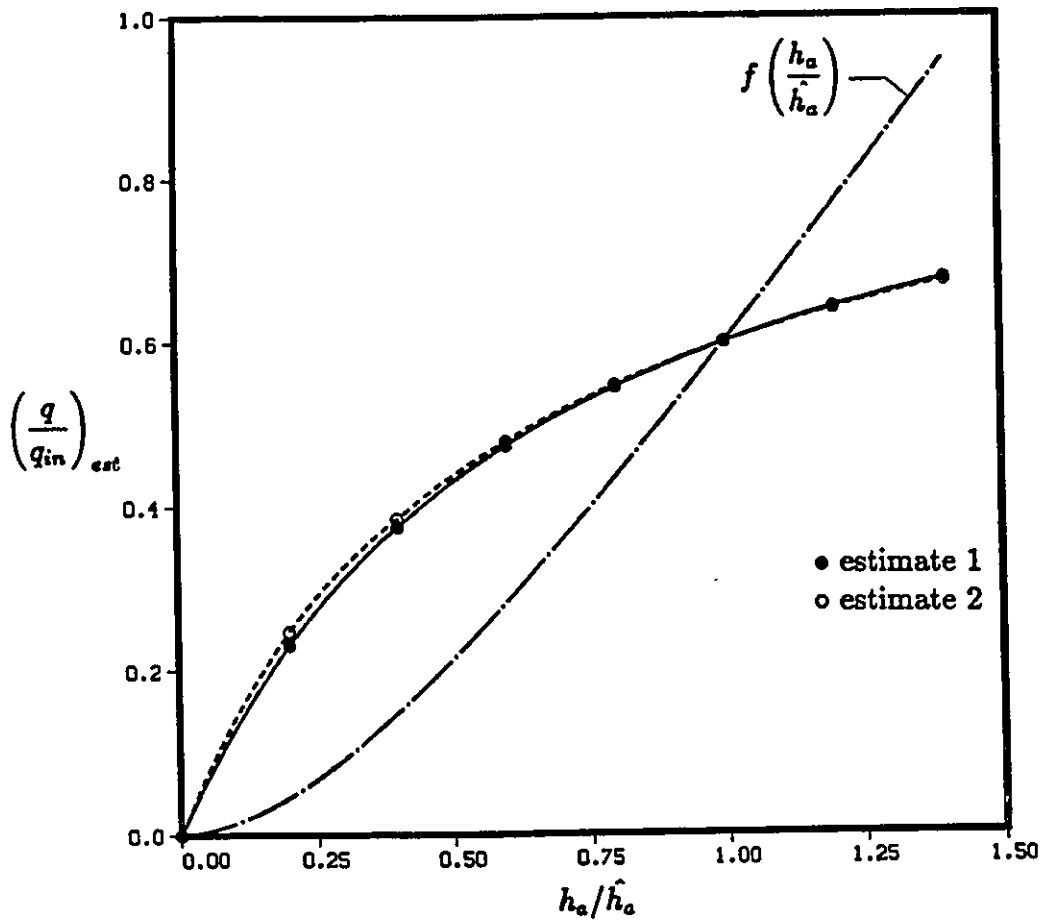

Figure 6.6: q/q_{in} variation with $h_a/\hat{h}_a$

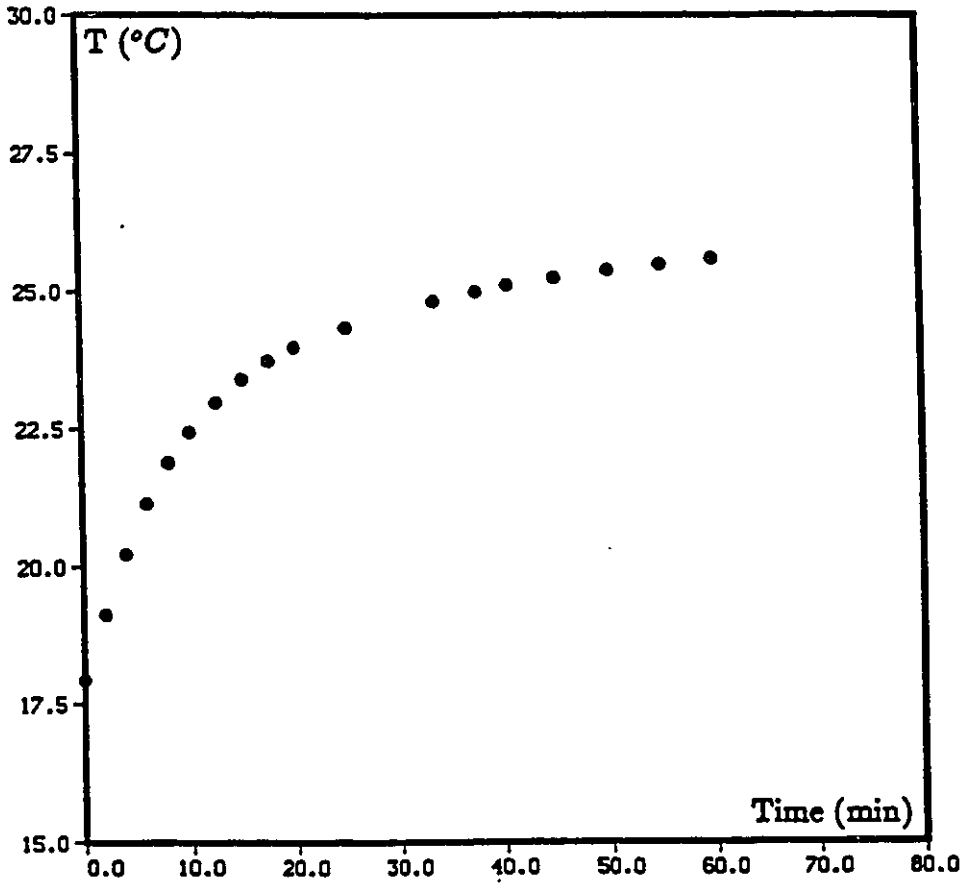

Figure 7.1: Unheated flow temperature as a function of duct operating time

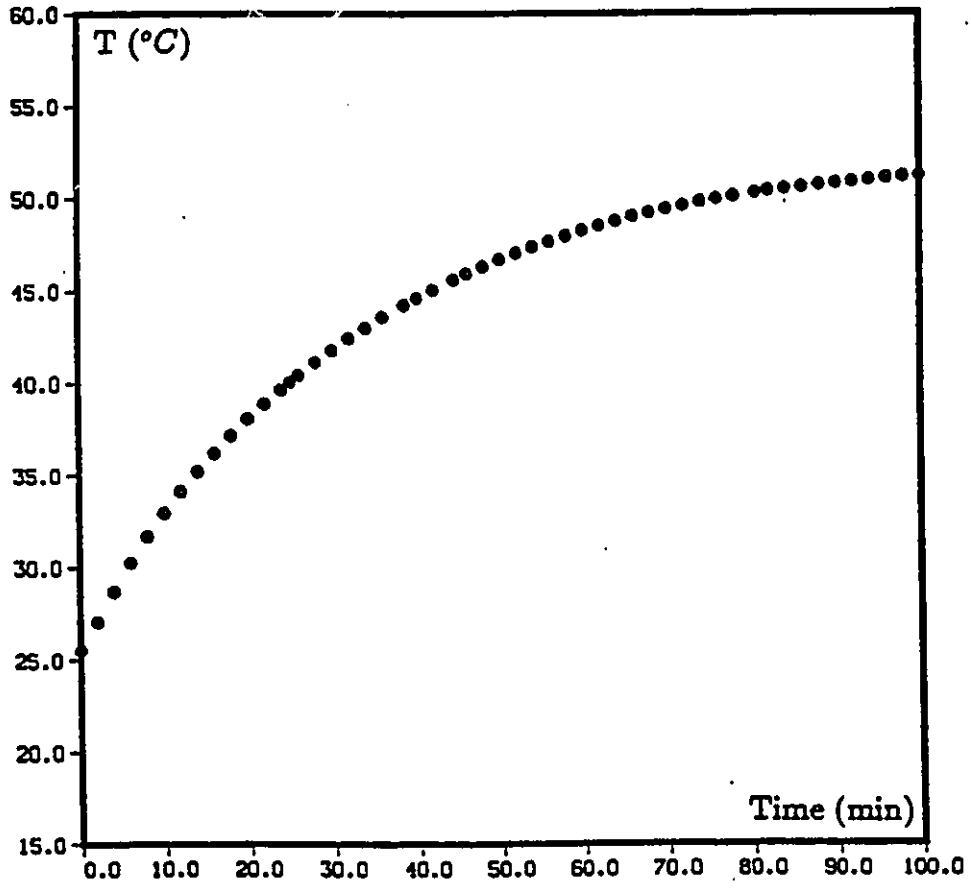

Figure 7.2: Heating block temperature as a function of the heater operating time

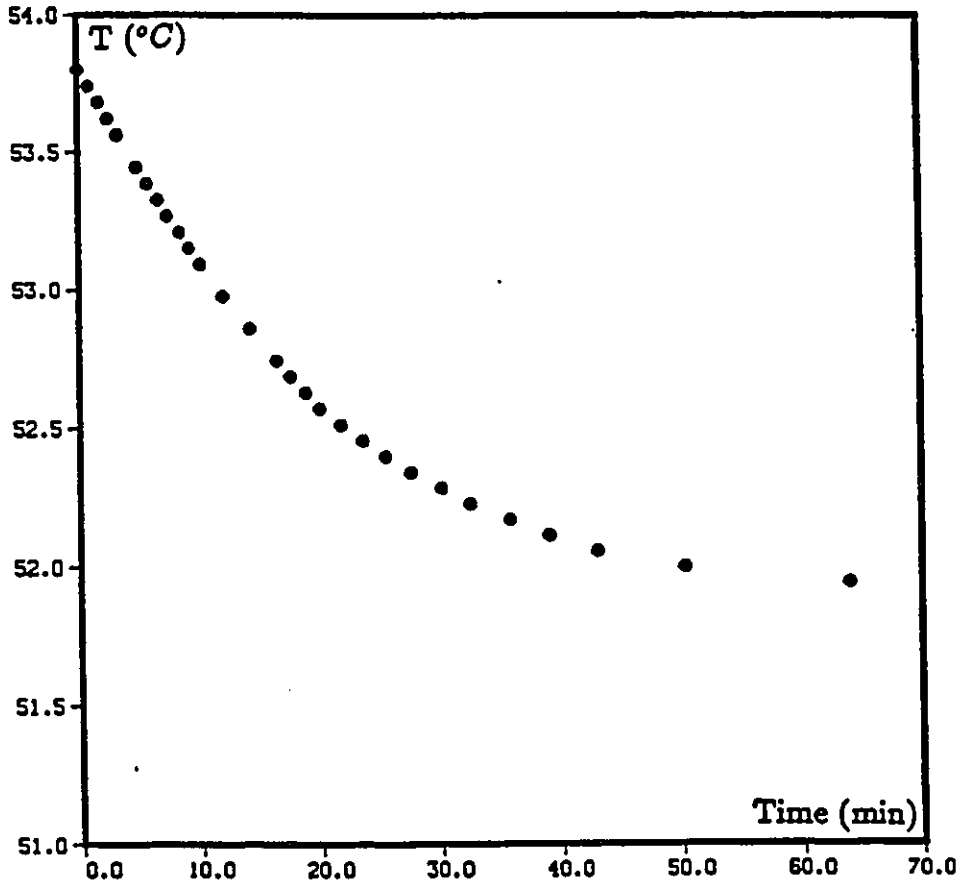

Figure 7.3: Heating block temperature as a function of time, after a step change in convection

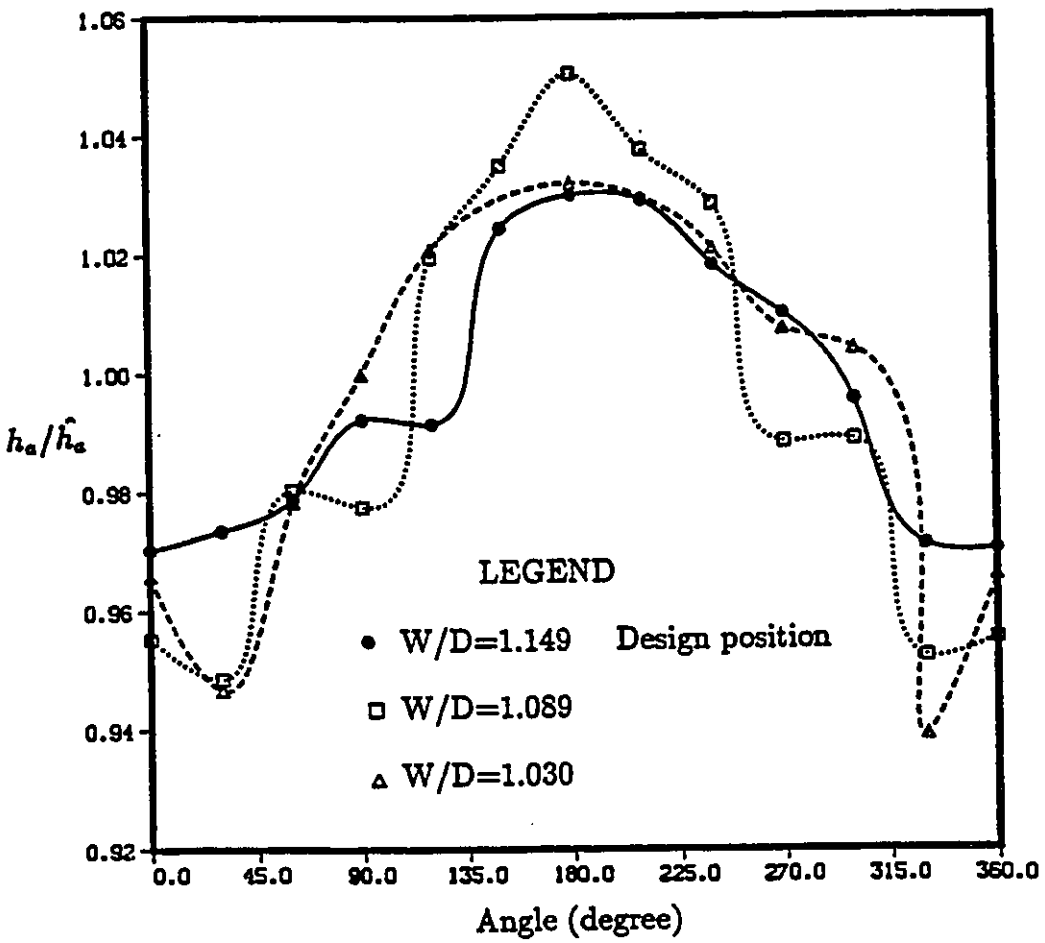

Figure 7.4: Distribution of the apparent heat transfer coefficient around the central rod for different values of W/D

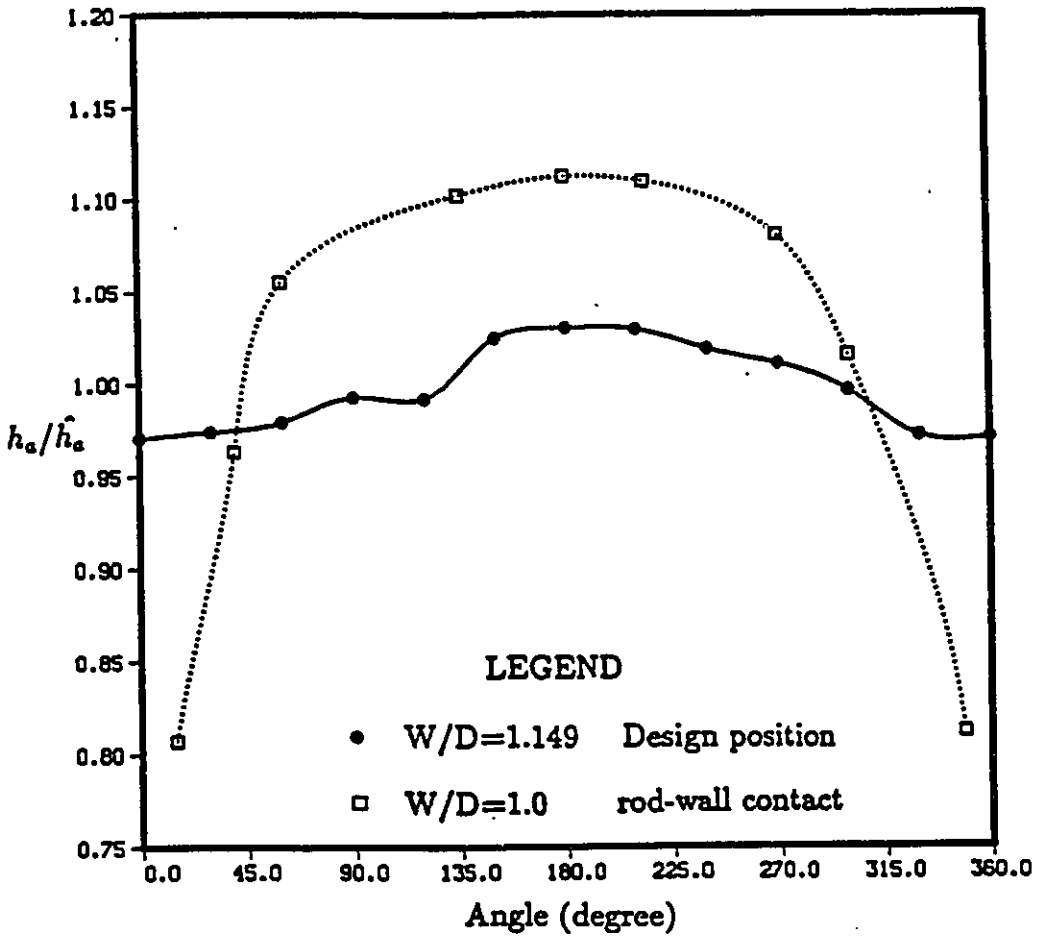

Figure 7.5: Distribution of the apparent heat transfer coefficient around the central rod for different values of W/D

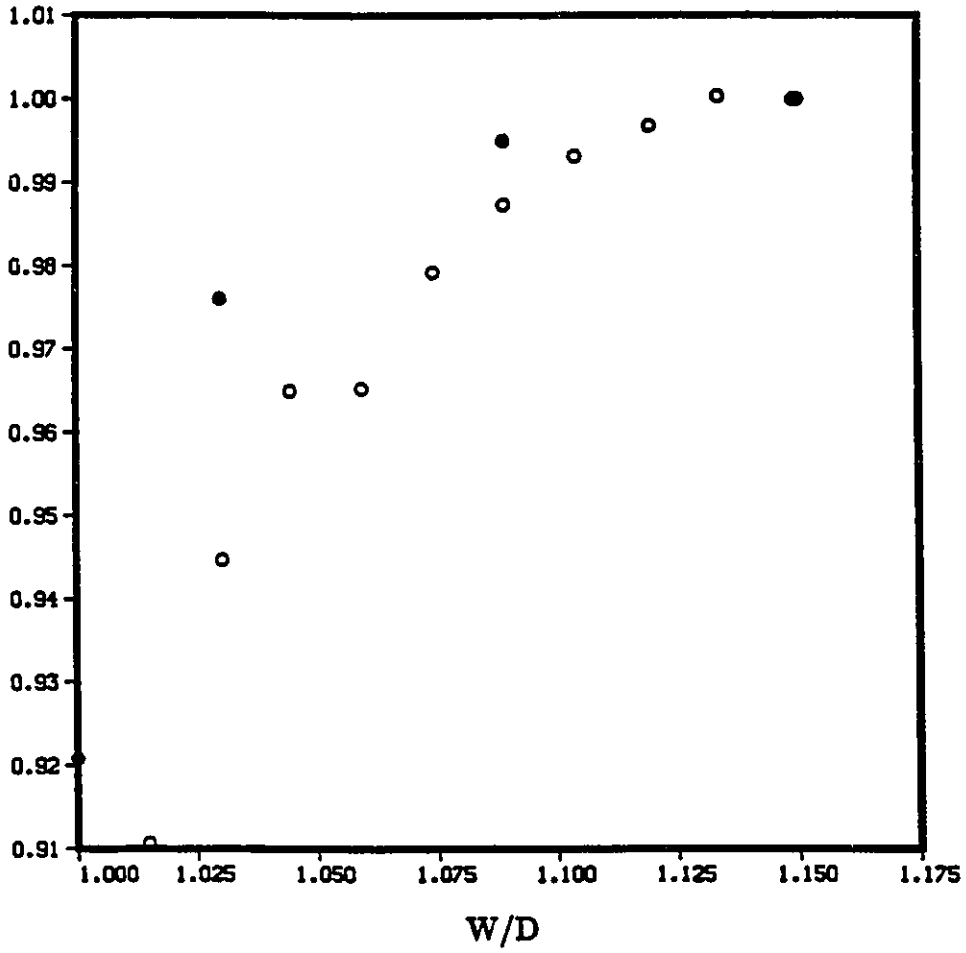

Figure 7.6: Variation of the apparent heat transfer coefficient with W/D $o h_a/h_{a_{design}}$ at the rod-wall gap; $\bullet \hat{h}_a/\hat{h}_{a_{design}}$

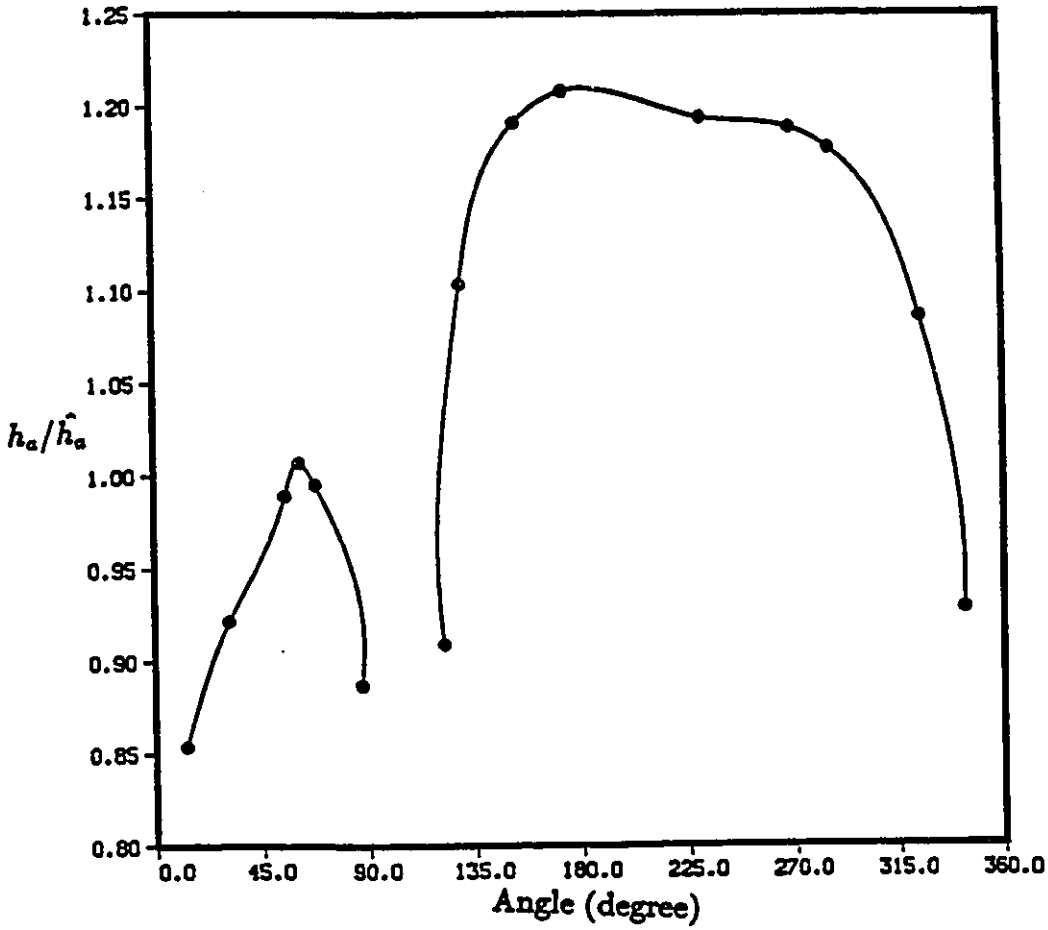

Figure 7.7: Distribution of the apparent heat transfer coefficient around the central rod for the rod-rod-wall contact position

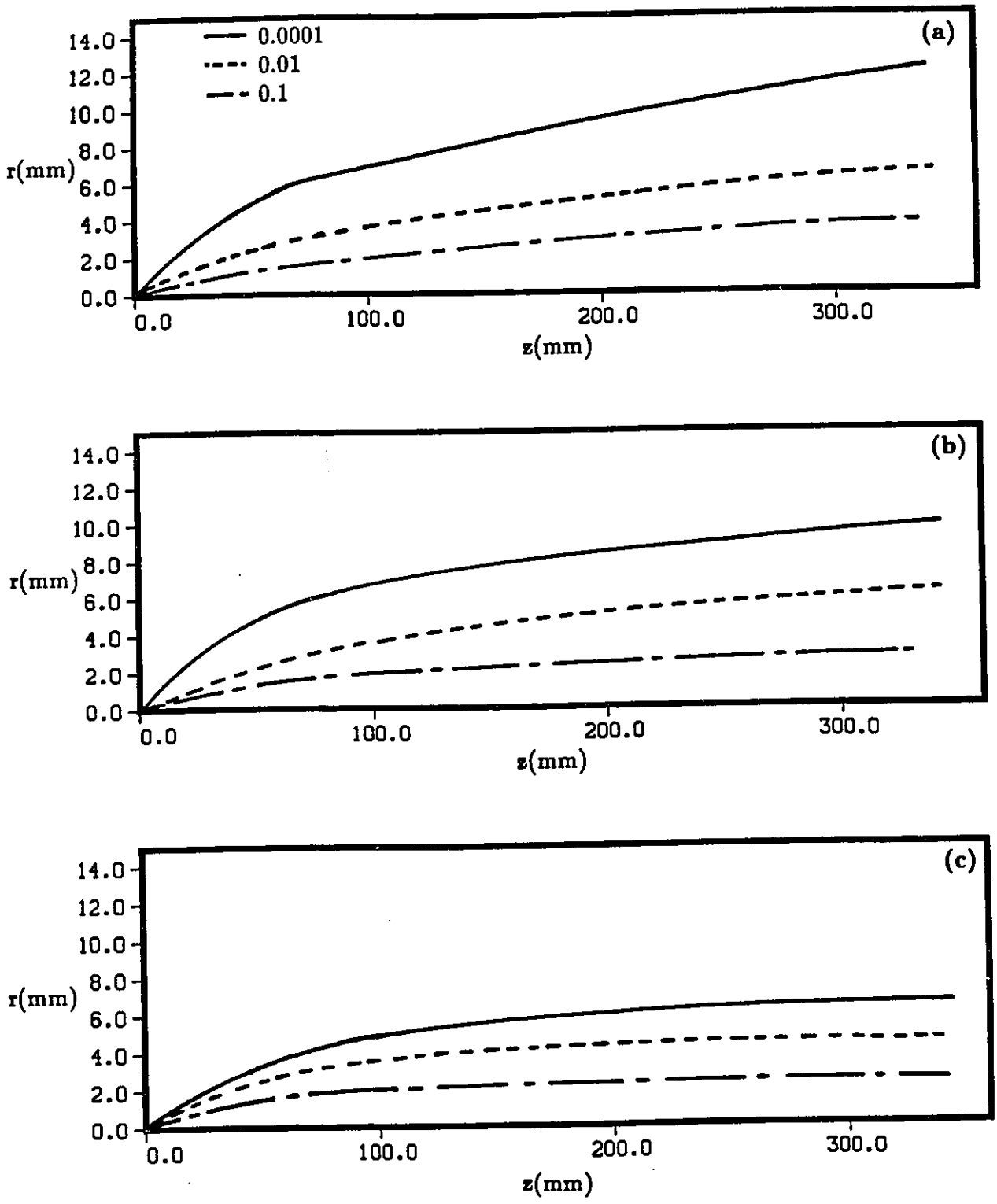

Figure 7.8: Downstream development of mean temperature isotherms $\left(\frac{T-T_\infty}{T_W-T_\infty}\right)$
(a) $\phi_o = -45°$, W/D=1.149; (b) $\phi_o = 0°$, W/D=1.149;
(c) $\phi_o = 0°$, W/D=1.119; (d) $\phi_o = 0°$, W/D=1.089;
(e) $\phi_o = 0°$, W/D=1.059.

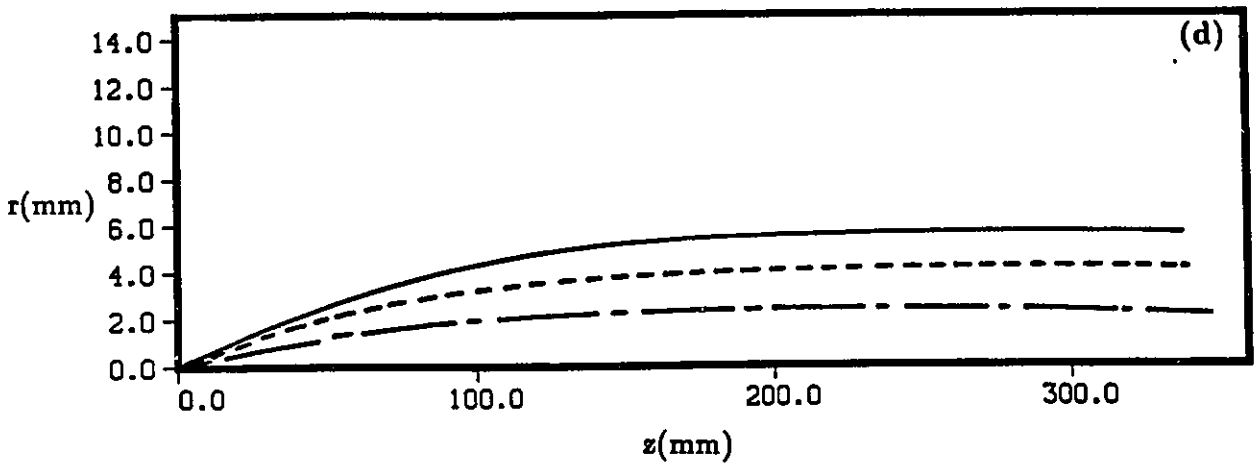
(d)
14.0
12.0
10.0
8.0
6.0
4.0
2.0
0.0
r(mm)
0.0
100.0
200.0
300.0
z(mm)

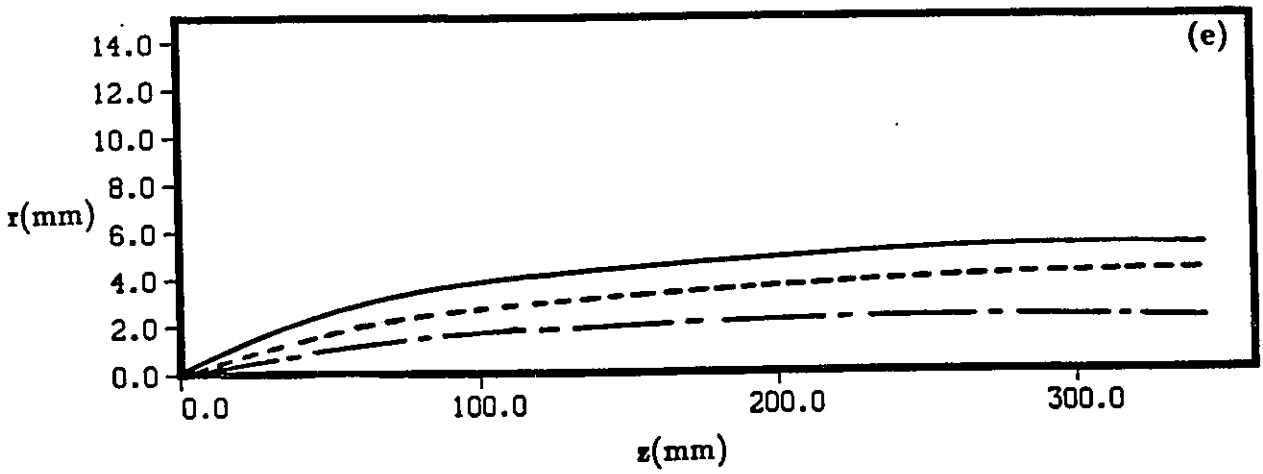
(e)
14.0
12.0
10.0
8.0
6.0
4.0
2.0
0.0
r(mm)
0.0
100.0
200.0
300.0
z(mm)

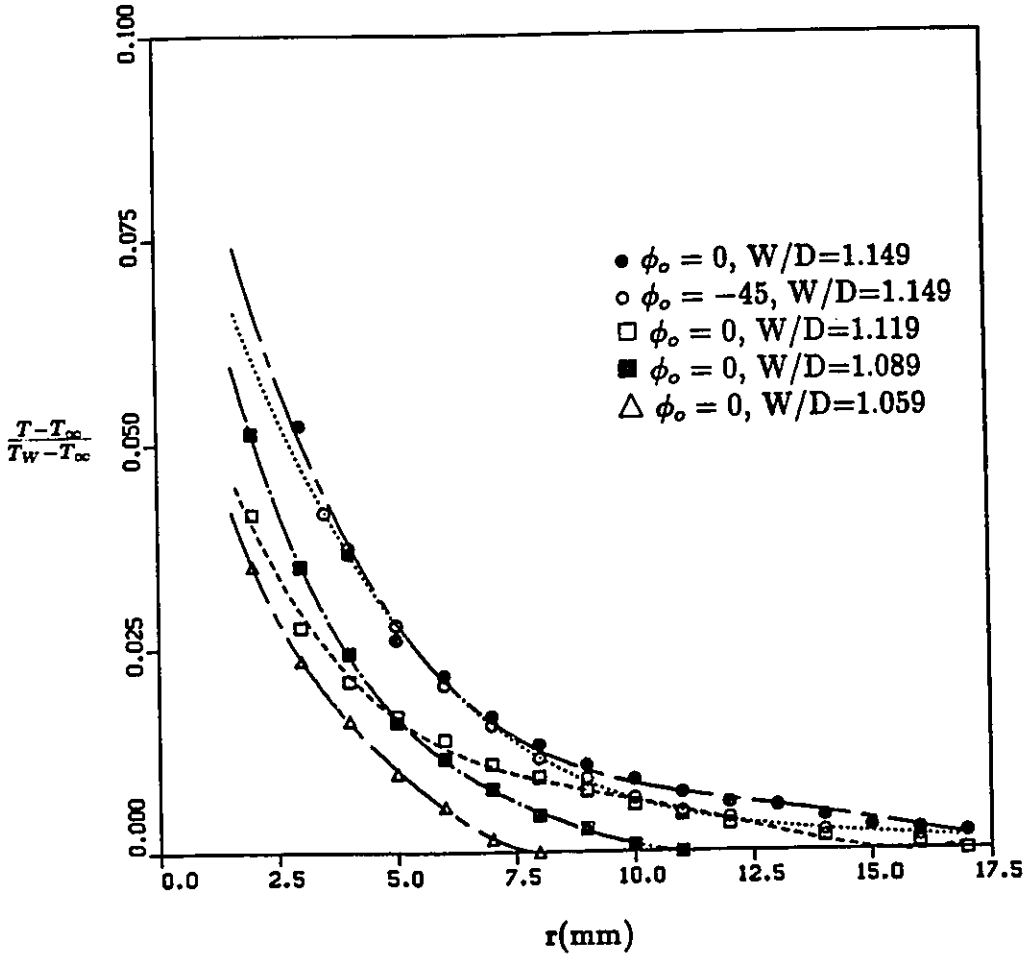

Figure 7.9: Mean temperature profiles ($\beta = 0°$).

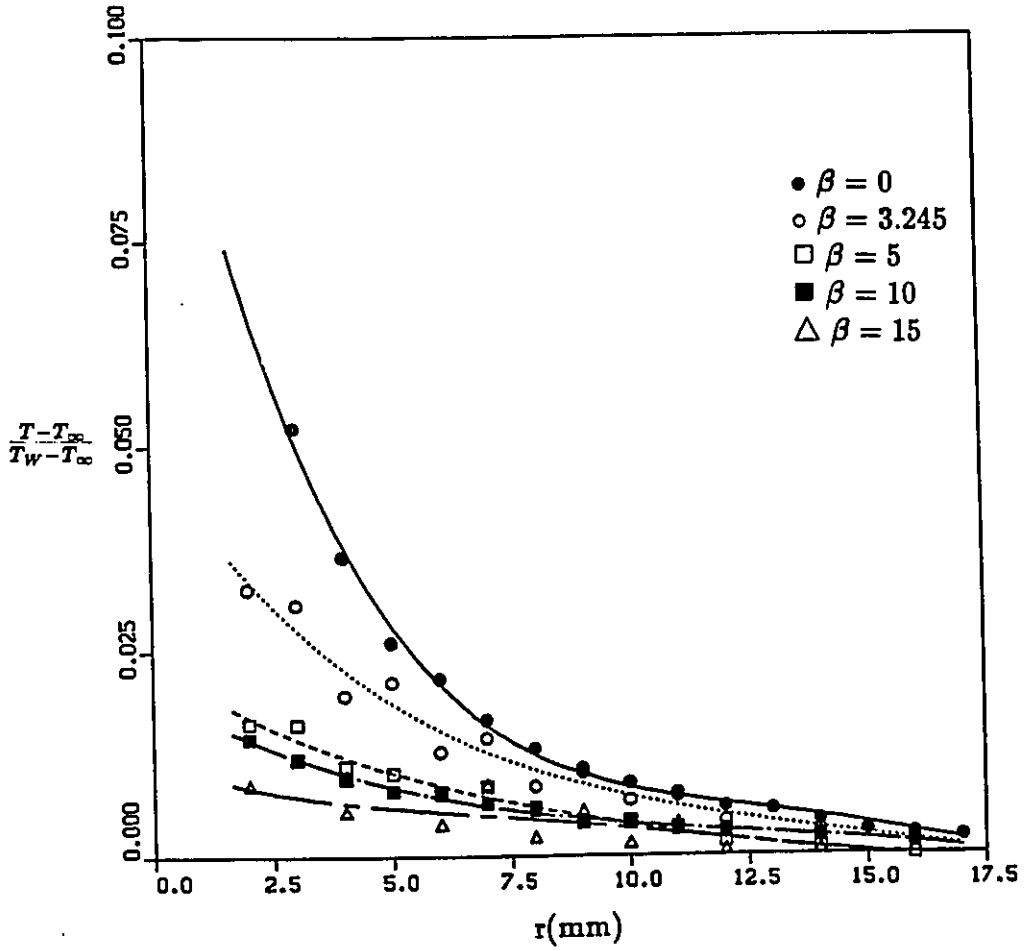

Figure 7.10: Mean temperature profiles ($\phi_o = 0°$, W/D=1.149).

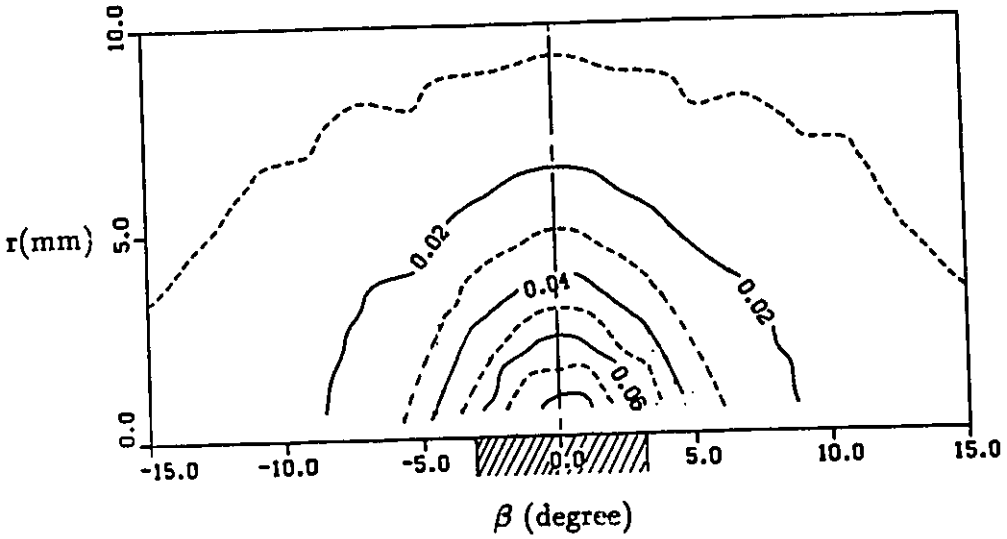

Figure 7.11: Mean temperature isotherm contours $\left(\frac{T-T_\infty}{T_W-T_\infty}\right)$ for $\phi_o = 0^o$

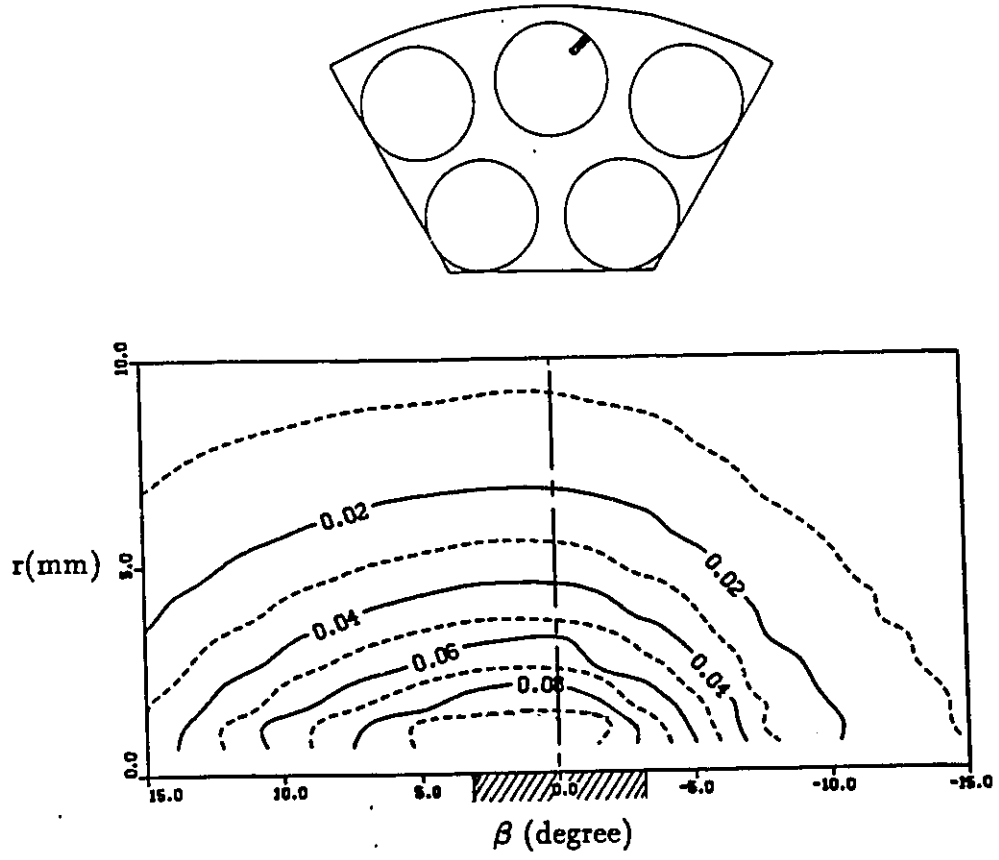

Figure 7.12: Mean temperature isotherm contours $\left(\frac{T-T_\infty}{T_W-T_\infty}\right)$ for $\phi_o = -45°$

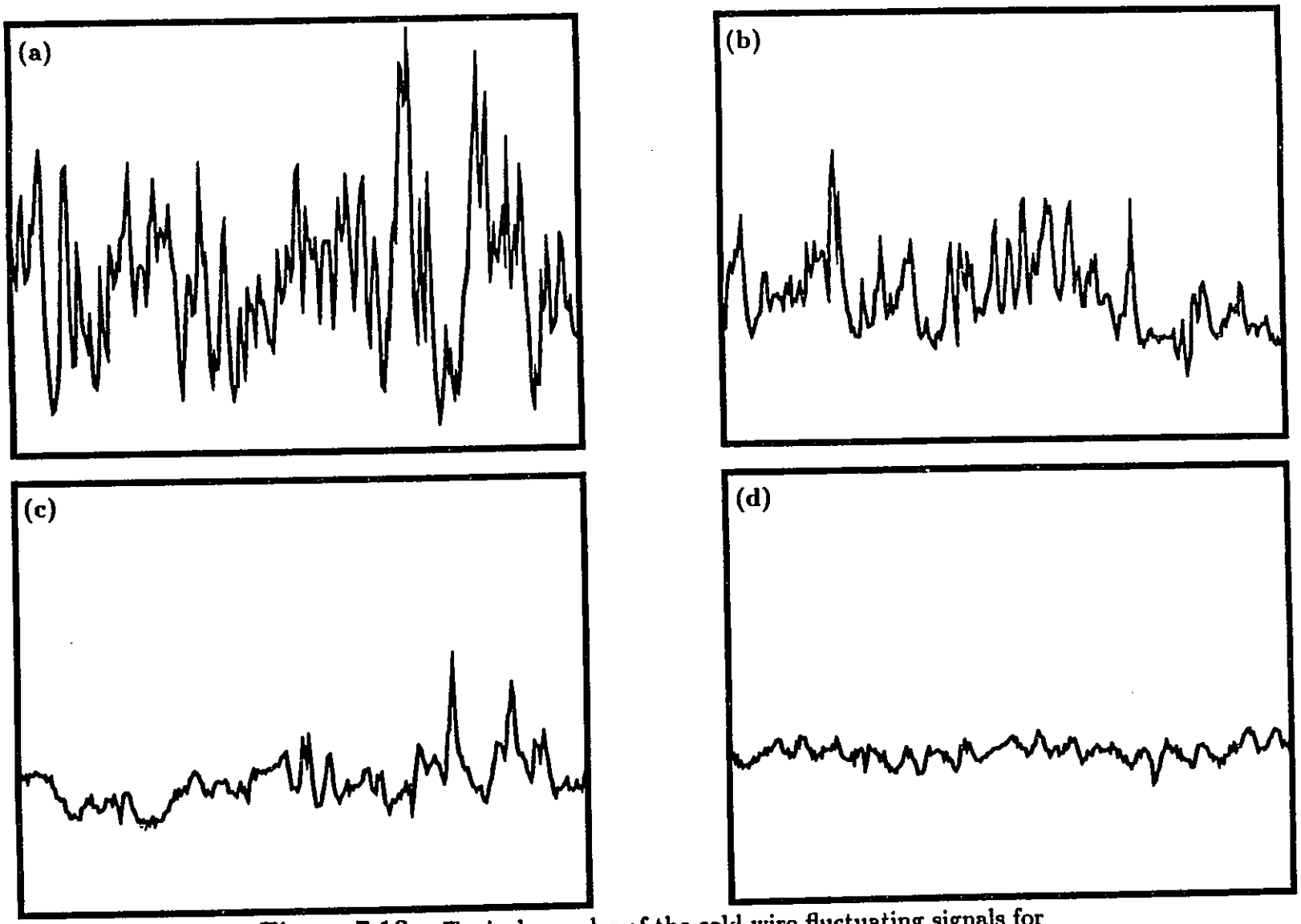

Figure 7.13: Typical samples of the cold-wire fluctuating signals for
(a) $\phi_o = 0°$, $\beta = 0°$ and r=2 mm;
(b) $\phi_o = 0°$, $\beta = 0°$ and r=6 mm;
(c) $\phi_o = 0°$, $\beta = 0°$ and r=10 mm;
(d) unheated flow

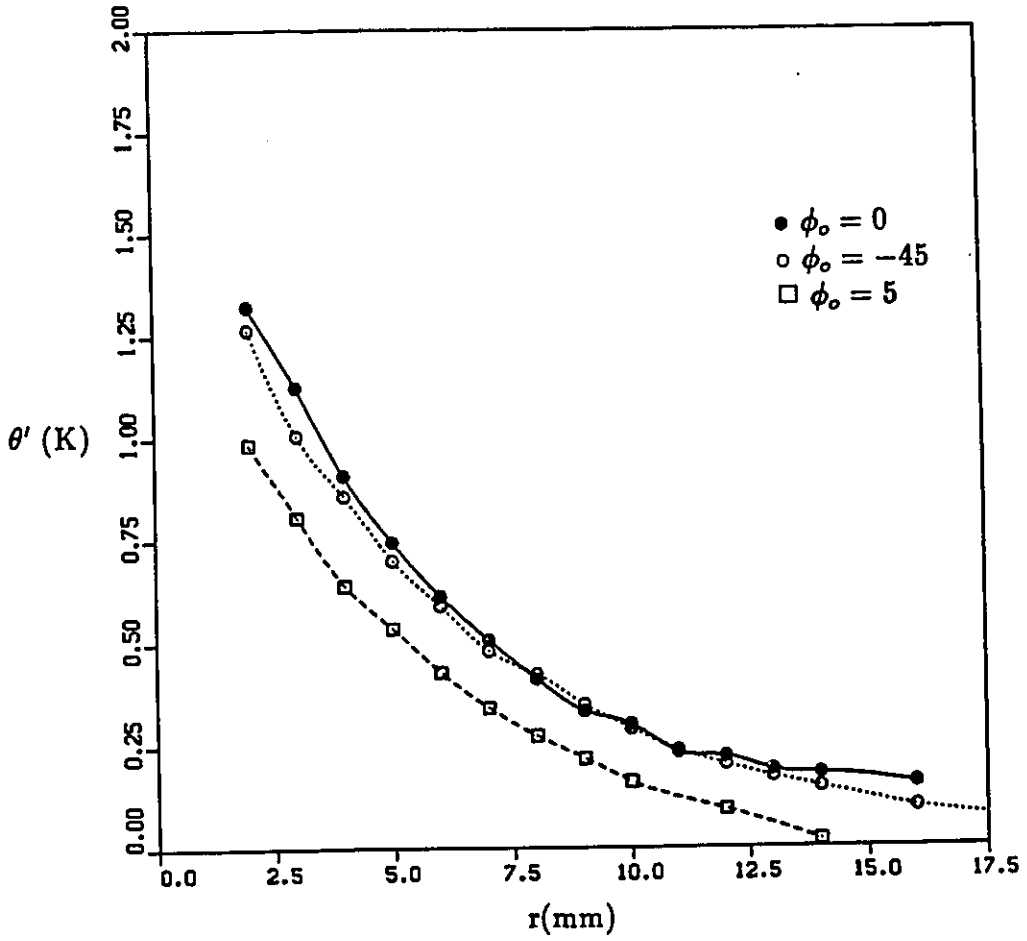

Figure 7.14: Profiles of the temperature fluctuation rms ($\beta = 0°$, W/D=1.149)

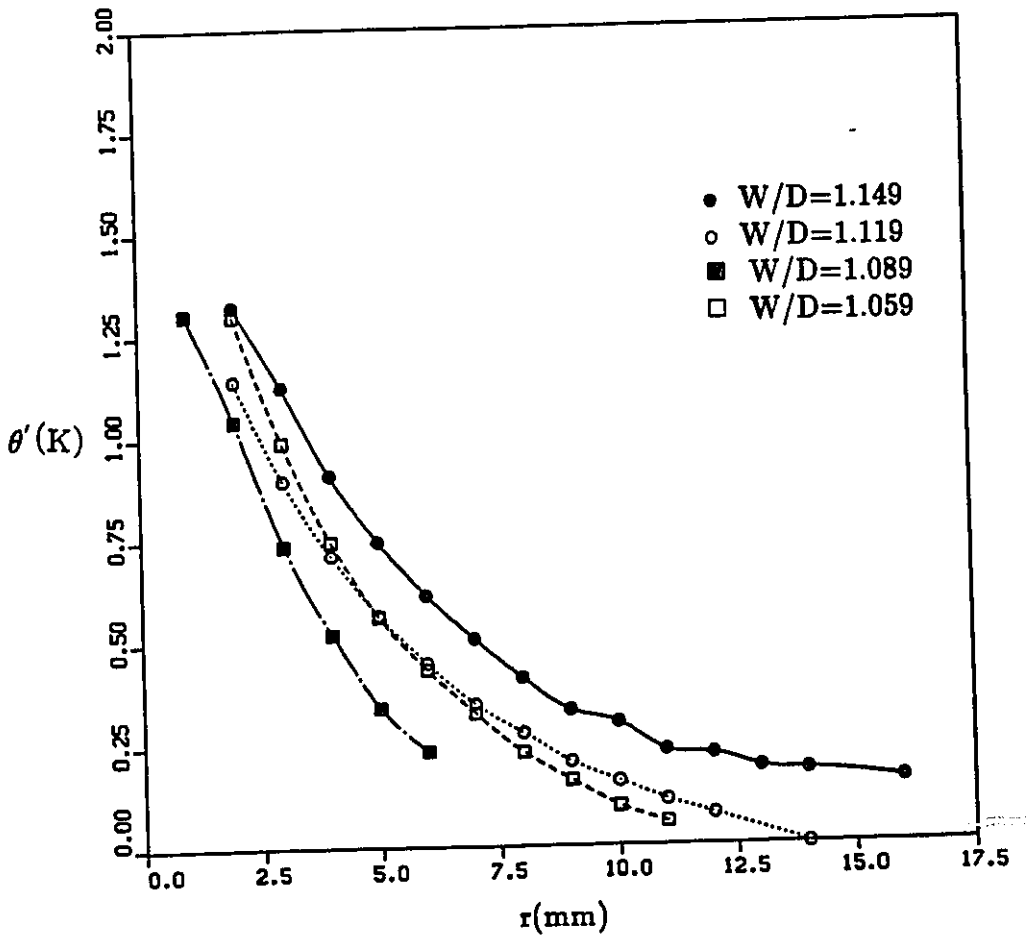

Figure 7.15: Profiles of the temperature fluctuation rms ($\beta = 0°$, $\phi_o = 0°$)

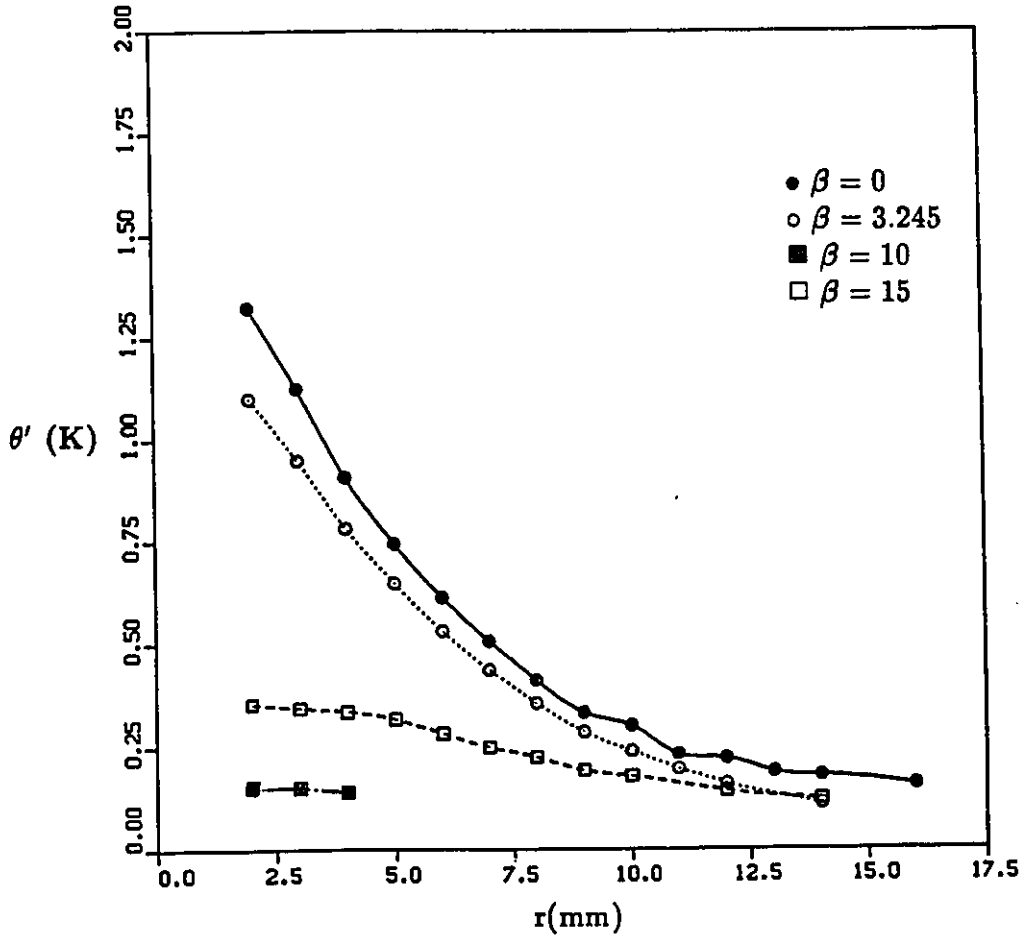

Figure 7.16: Profiles of the temperature fluctuation rms ($\phi_o = 0°$, W/D=1.149)

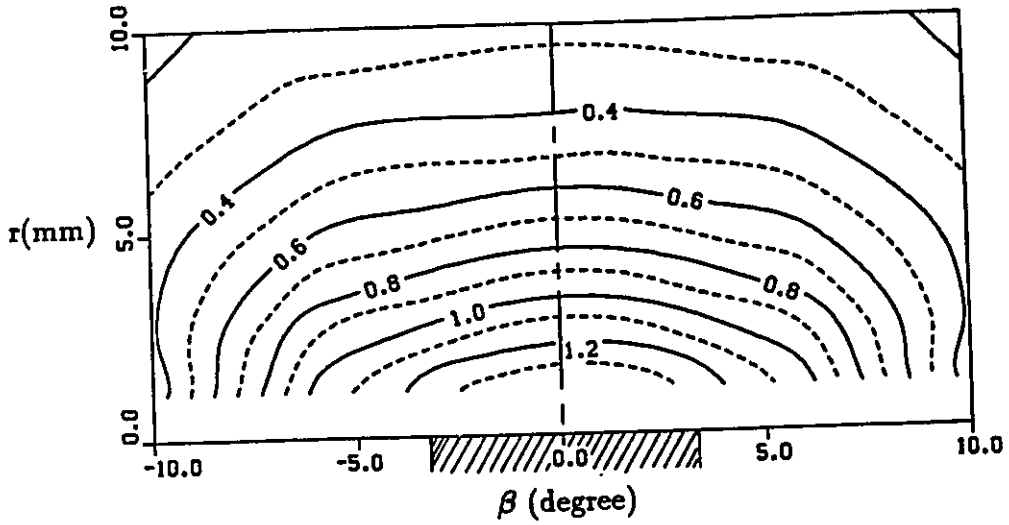

(a)

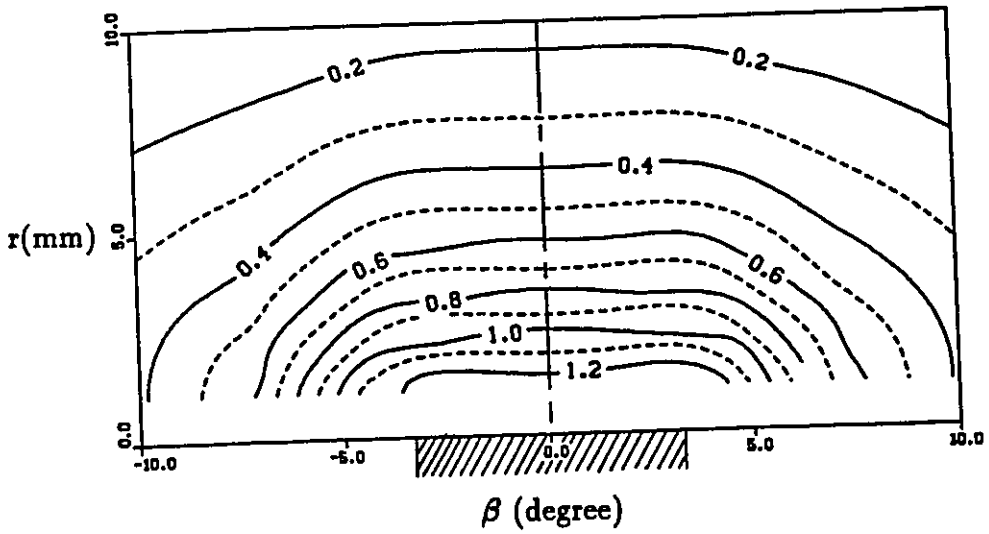

(b)

Figure 7.17: Constant-θ' contours for $\phi_o = 0^o$ and (a) W/D=1.149 ; (b) W/D=1.1 (c) W/D=1.089 ; (d) W/D=1.059 .

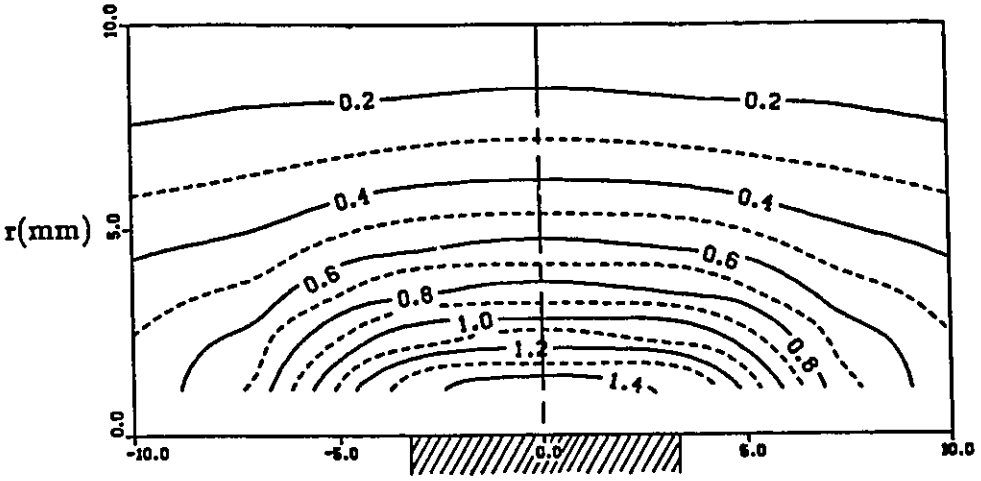
r(mm)
10.0
5.0
0.0
0.2
0.2
0.4
0.4
0.6
0.6
0.8
1.0
1.2
1.4
0.6
-10.0
-5.0
0.0
5.0
10.0
β (degree)

(c)

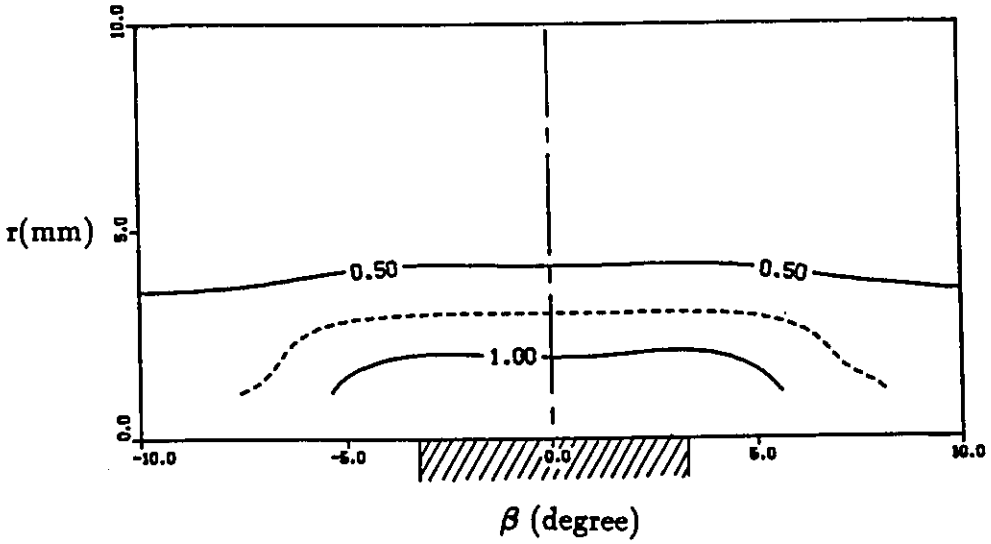
r(mm)
10.0
5.0
0.0
0.50
0.50
1.00
-10.0
-5.0
0.0
5.0
10.0
β (degree)

(d)

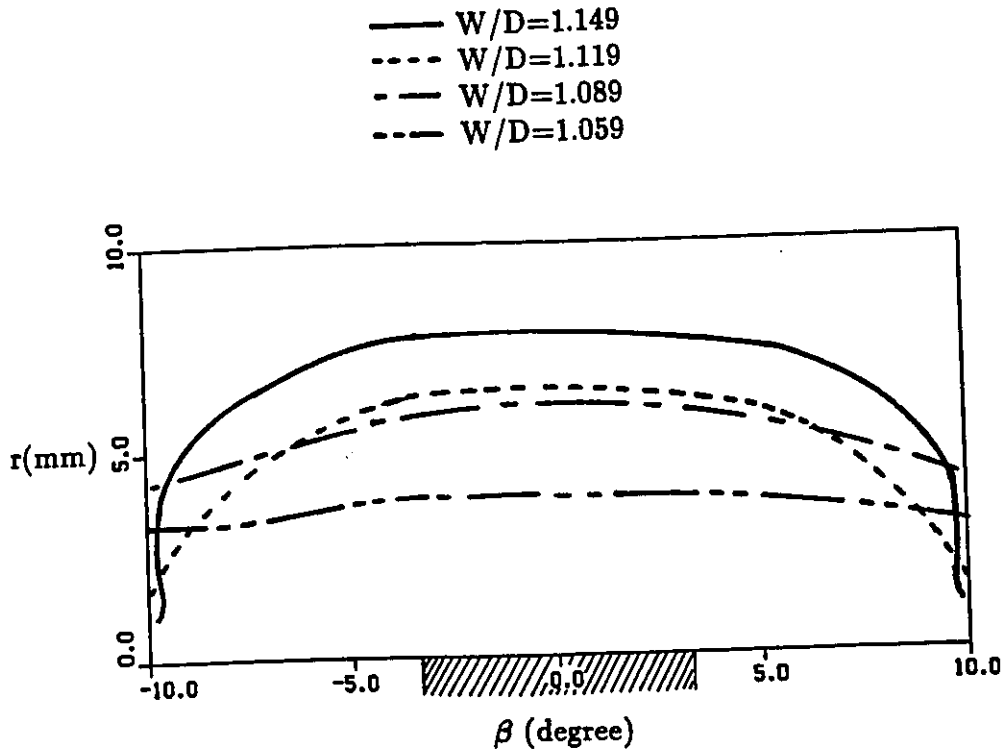

Figure 7.18: θ'=0.4K contour for several W/D.

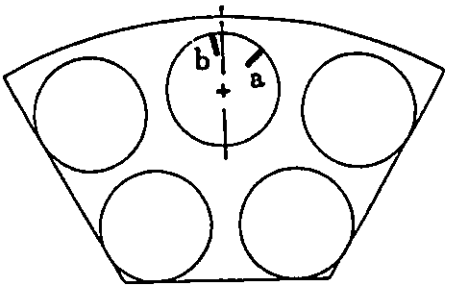

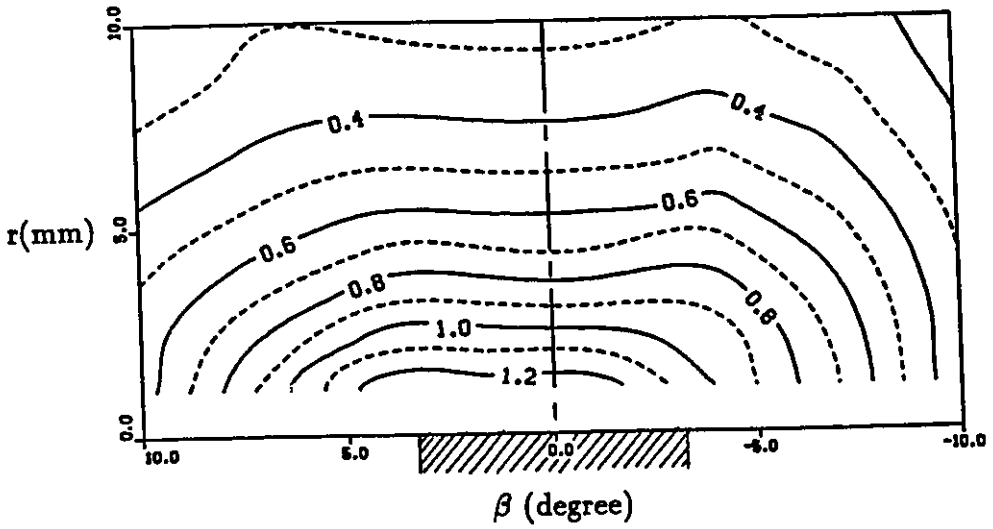

(a)

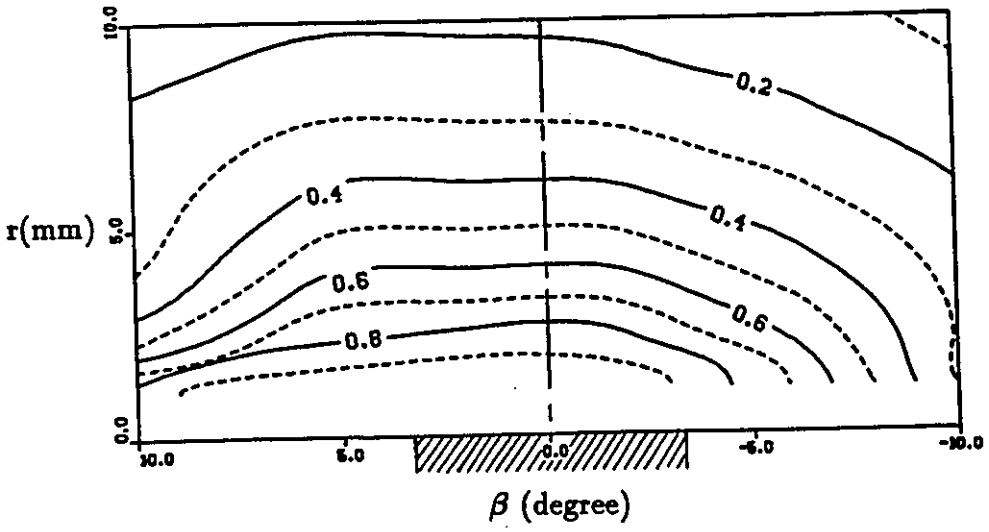

(b)

Figure 7.19: Constant-θ' contours for W/D=1.149 and (a) $\phi_o = -45°$; (b) $\phi_o = 5°$.

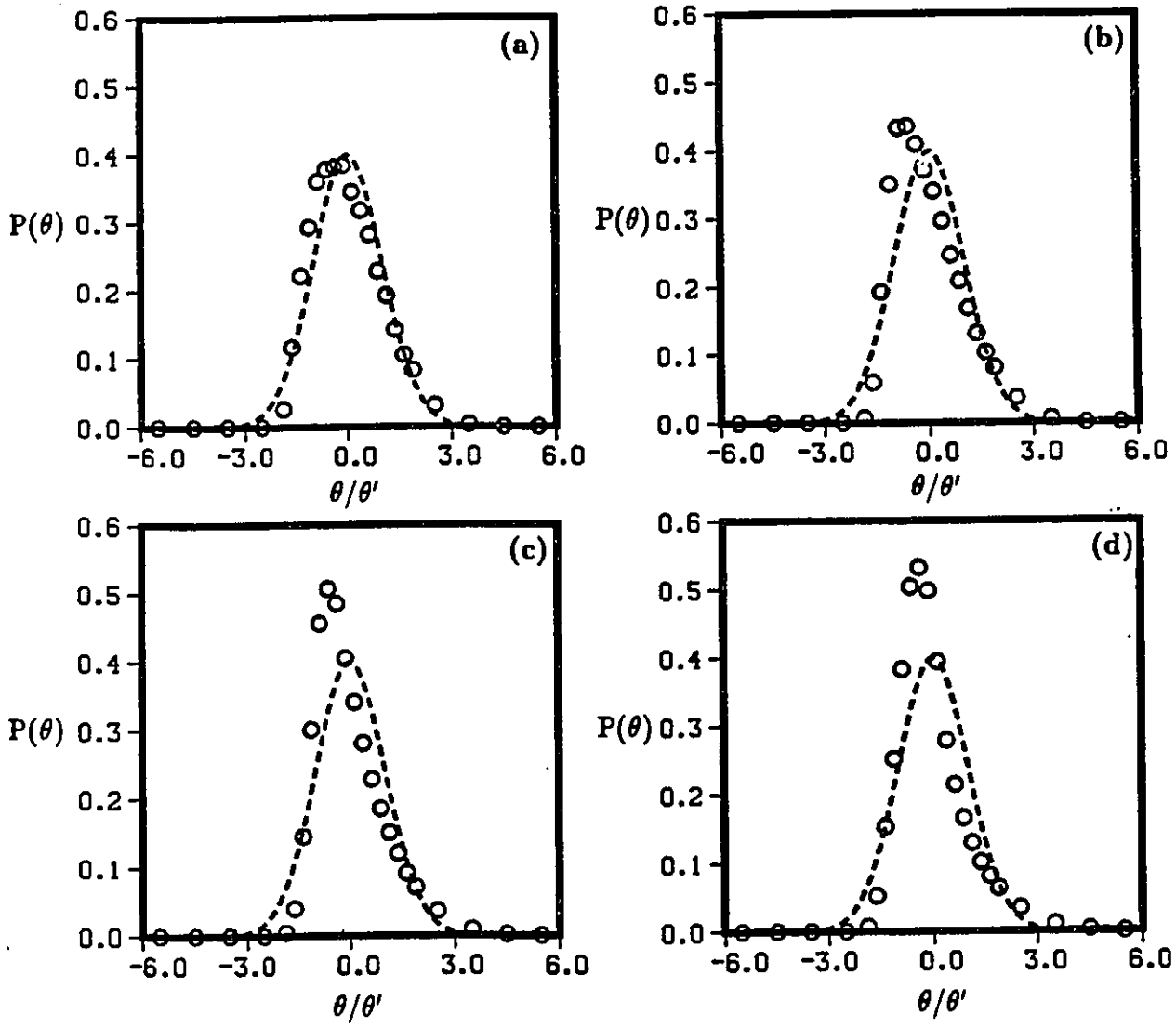

Figure 7.20: Pdf of the fluctuating temperature signal for $\phi_o = 0°$, W/D=1.149 and (a) r=2 mm; (b) r=4 mm; (c) r=6 mm; (d) r=8 mm.

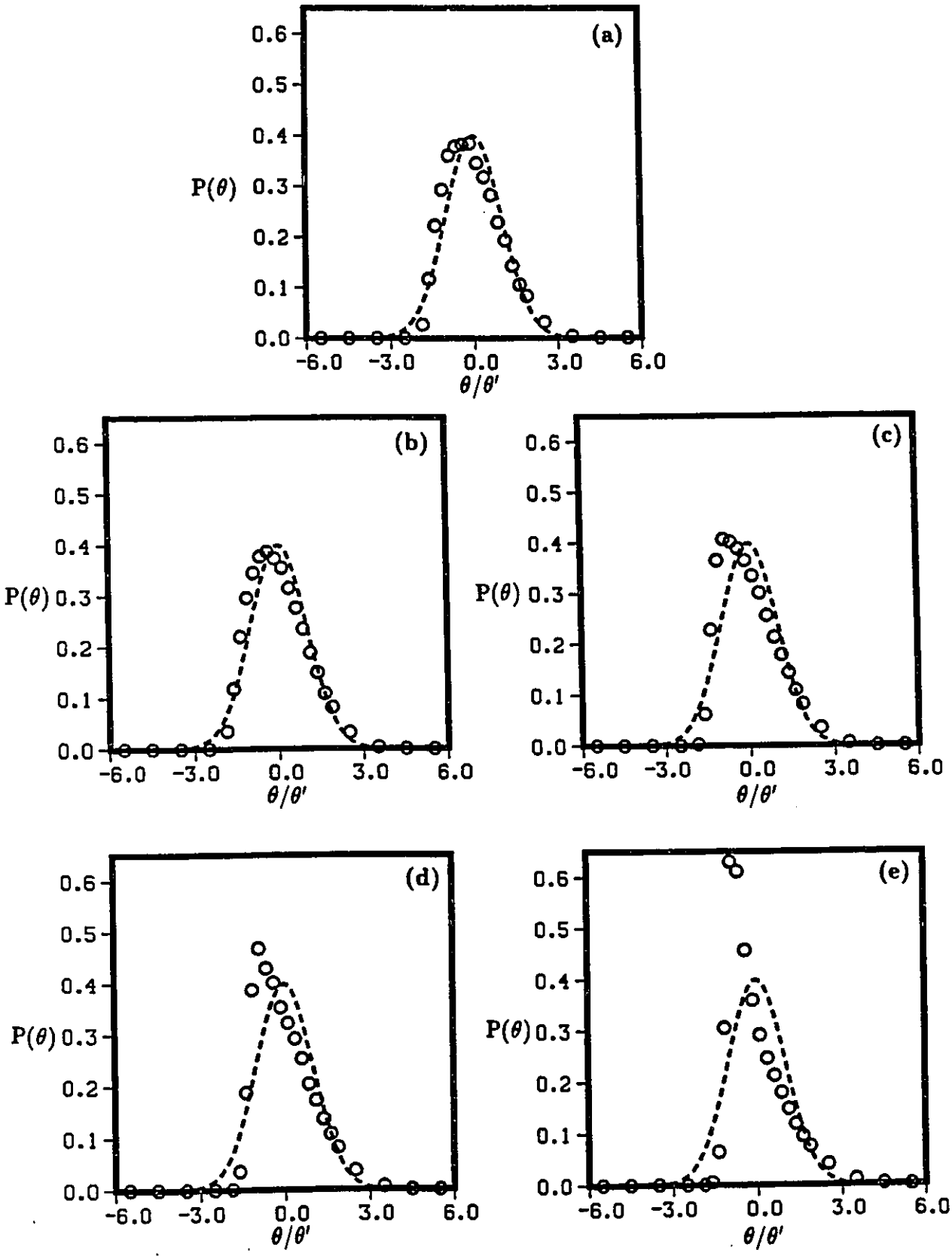

Figure 7.21: Pdf of the fluctuating temperature signal for r=2 mm and (a) $\phi_o = -45°$, W/D=1.149; (b) $\phi_o = 0°$, W/D=1.149; (c) $\phi_o = 0°$, W/D=1.119; (d) $\phi_o = 0°$, W/D=1.089; (e) $\phi_o = 0°$, W/D=1.059.

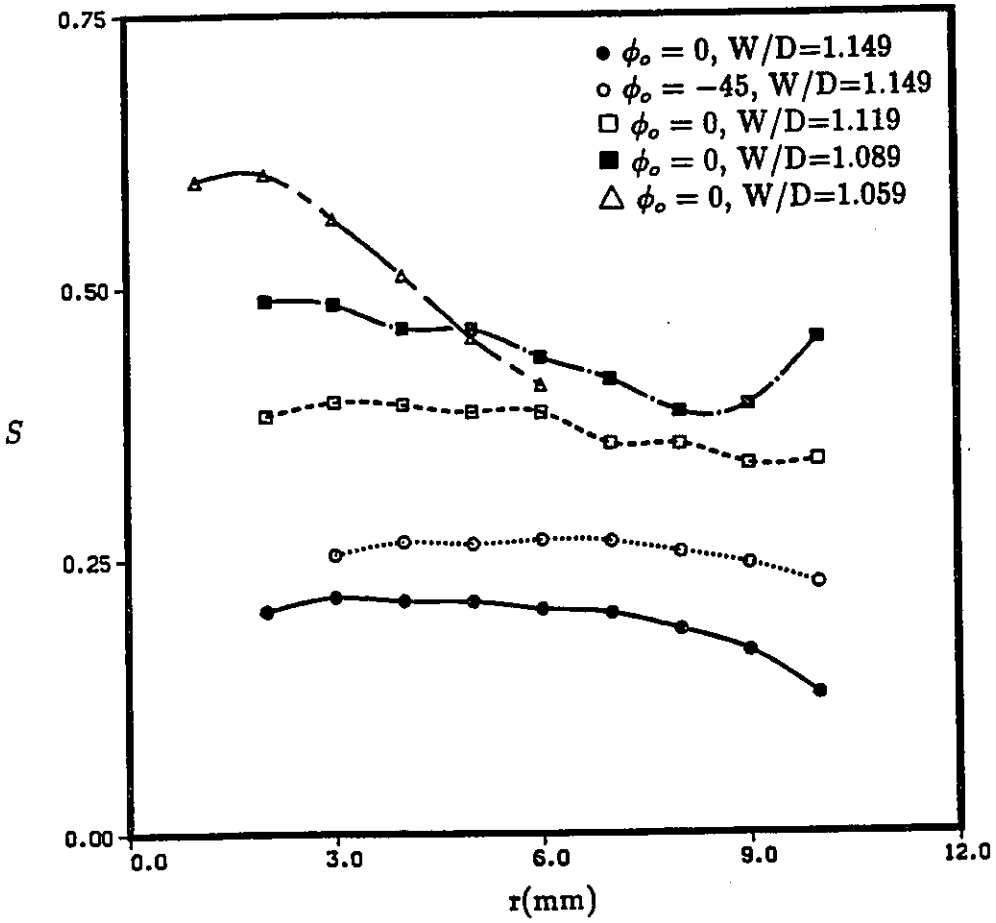

Figure 7.22: Skewness factor profiles ($\beta = 0°$)

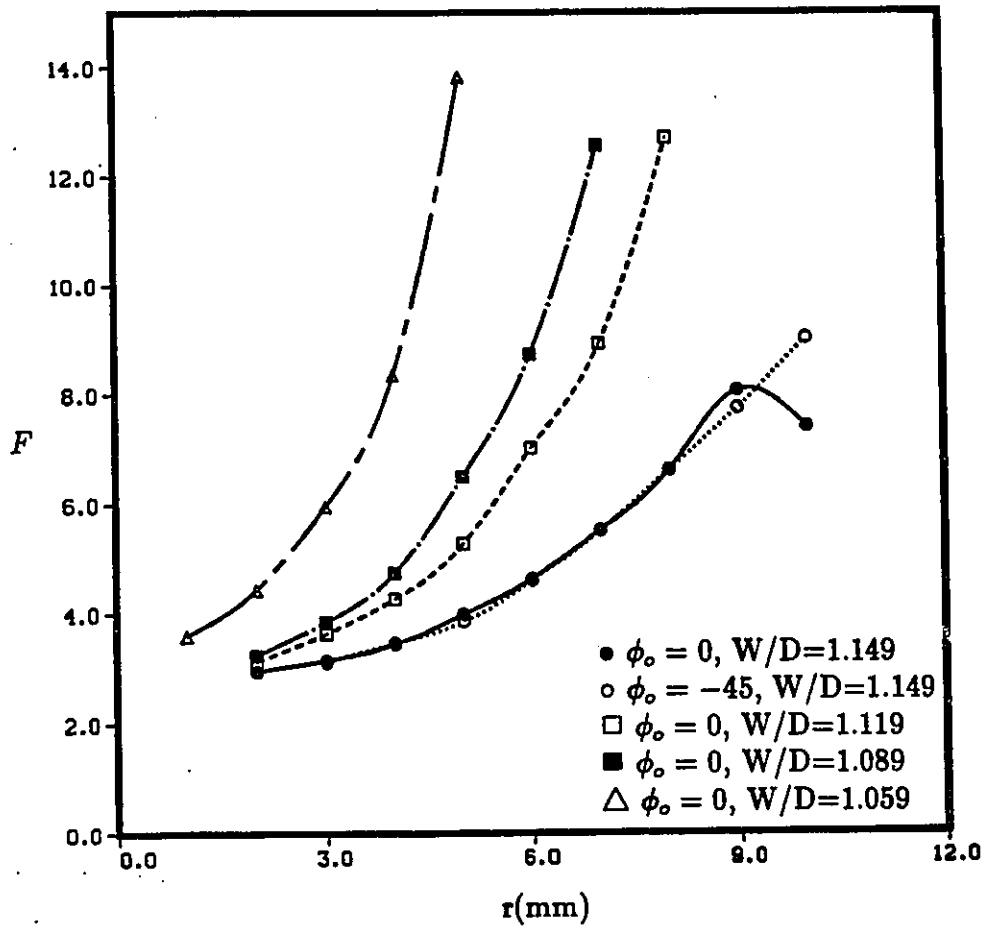

Figure 7.23: Flatness factor profiles ($\beta = 0°$)

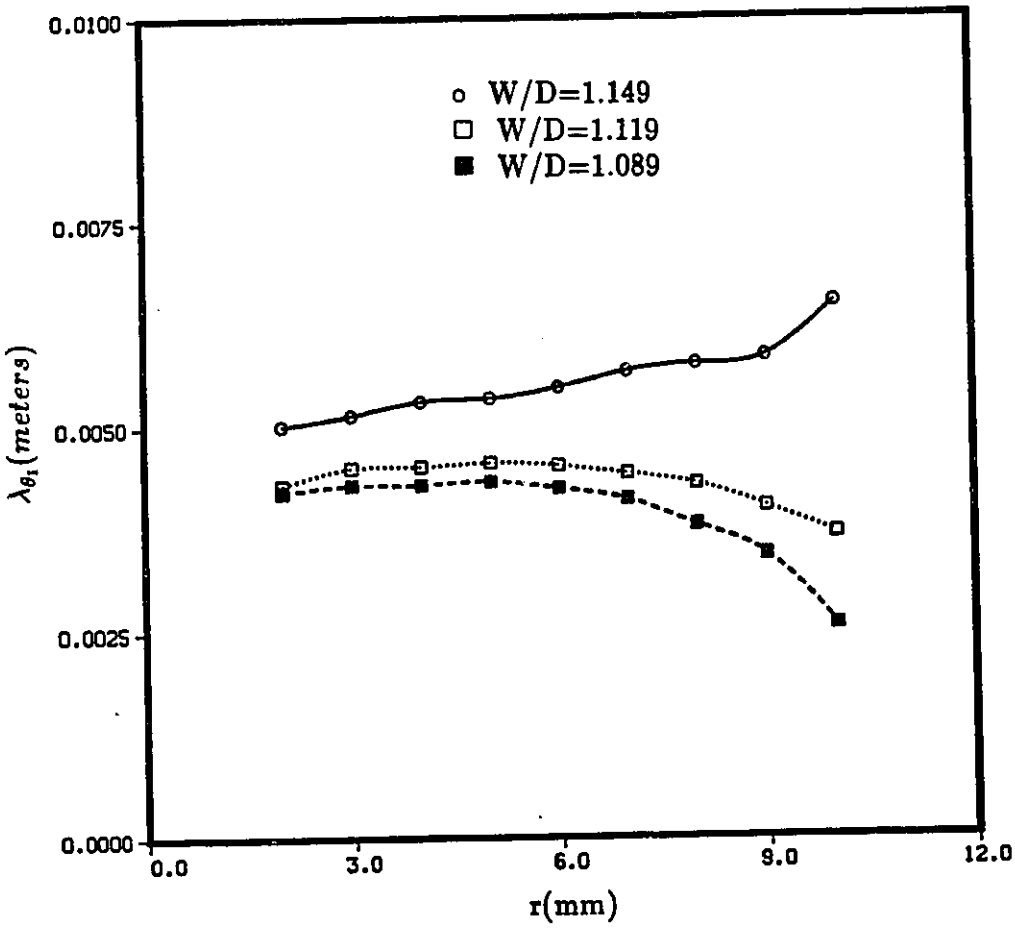

Figure 7.24: Corrsin microscale profiles ($\phi_o = 0°$, $\beta = 0°$)

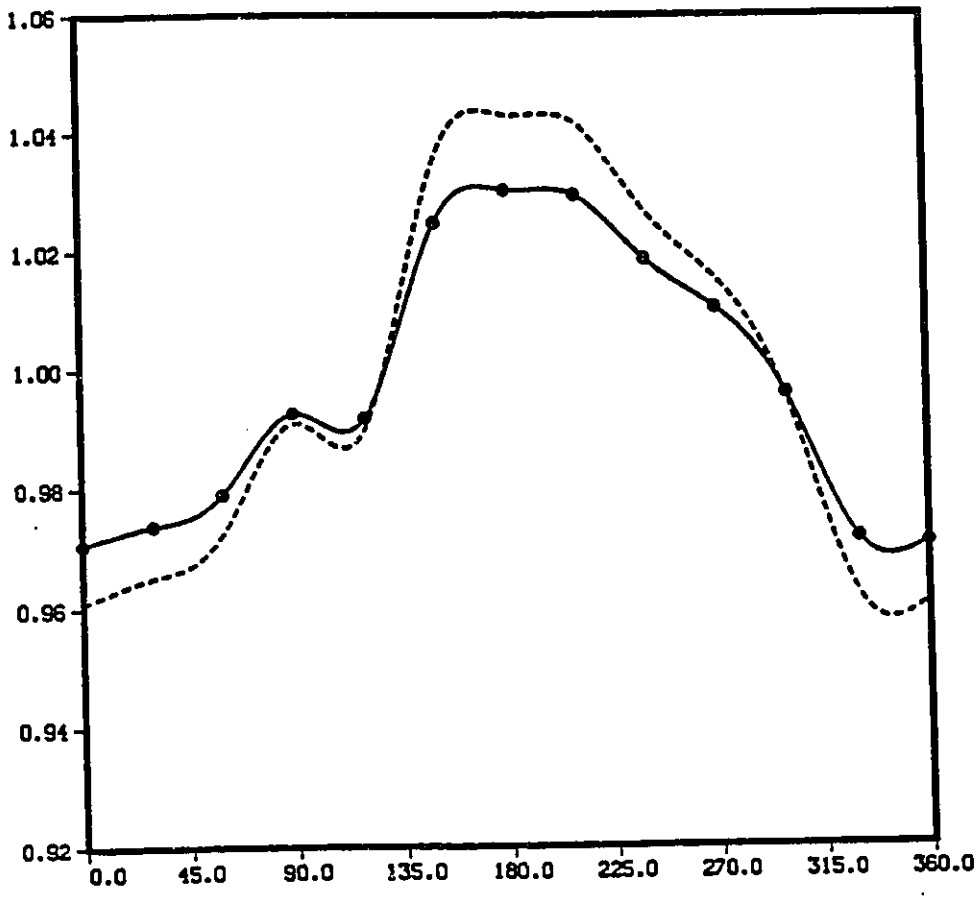

Figure 8.1: Distribution of the apparent and corrected heat transfer coefficients around the central rod for the design position

--- $h_c/\hat{h}_c$; -•- $h_a/\hat{h}_a$

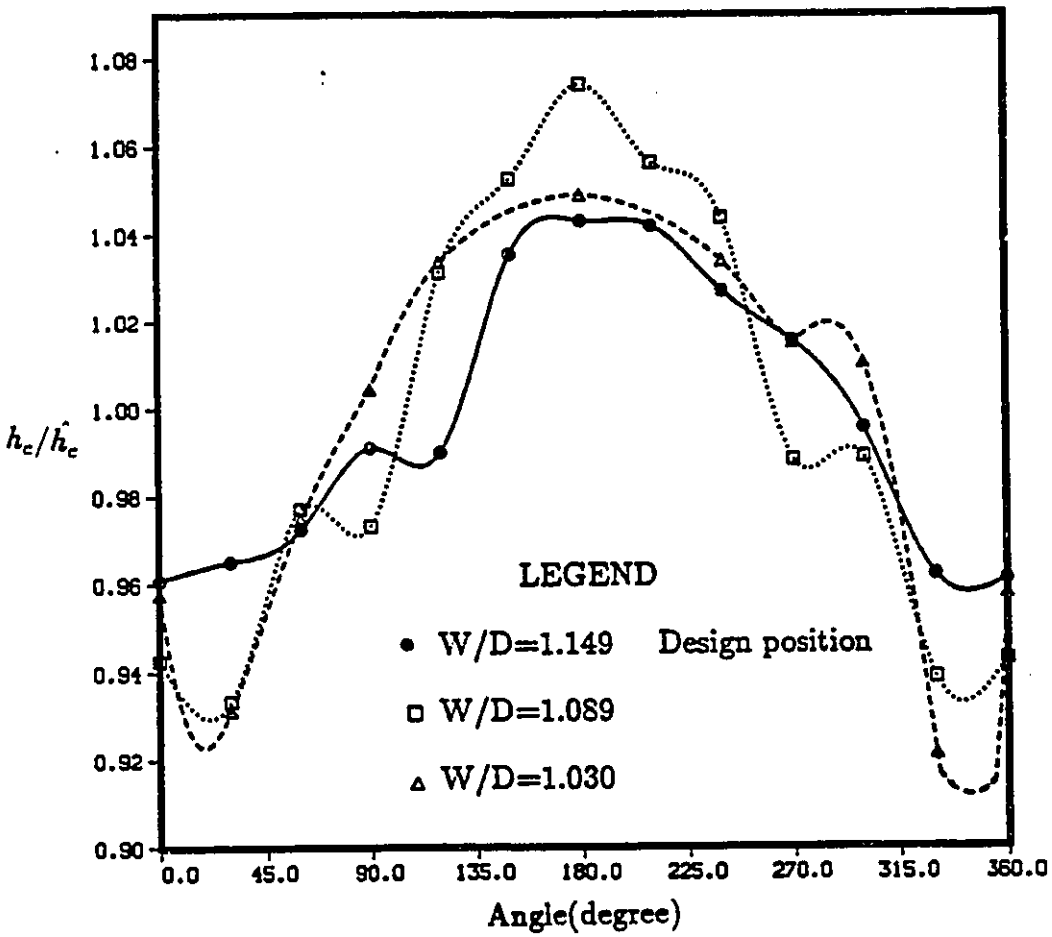

Figure 8.2: Distribution of the corrected heat transfer coefficient around the central rod for different values of W/D

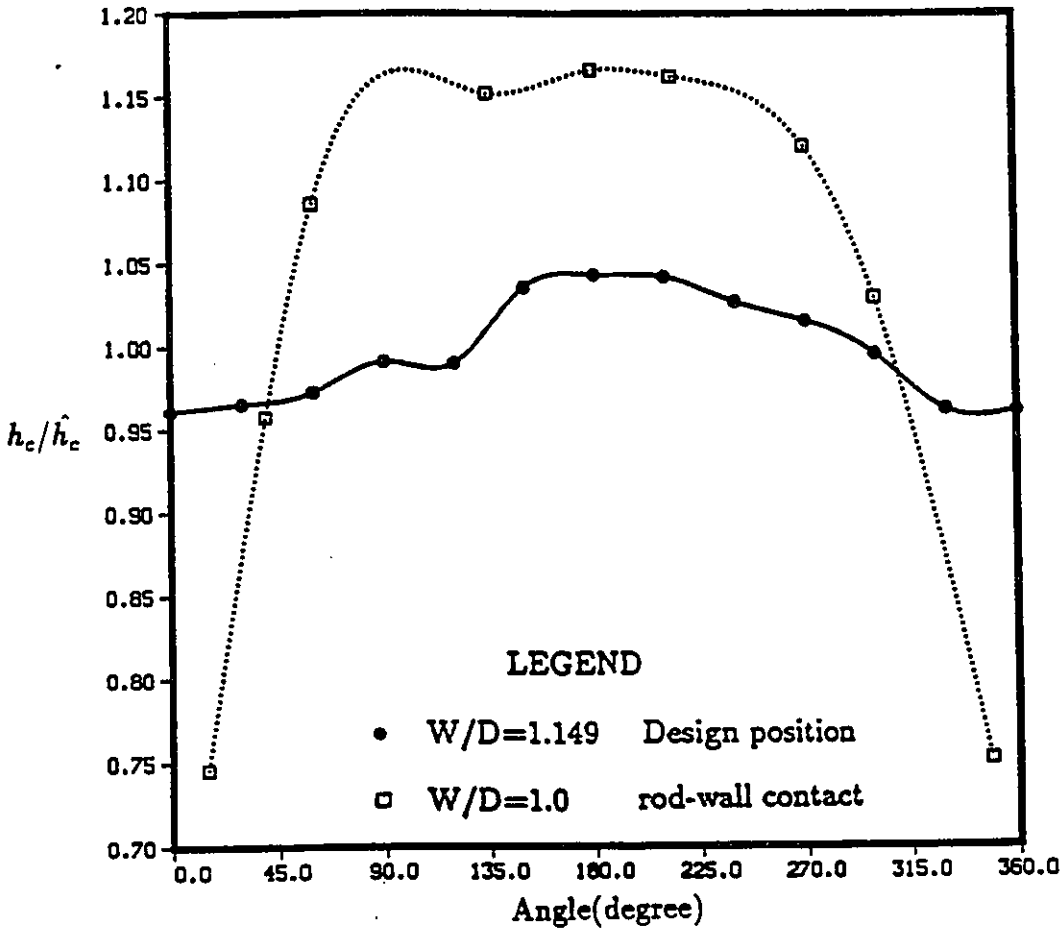

Figure 8.3: Distribution of the corrected heat transfer coefficient around the central rod for different values of W/D

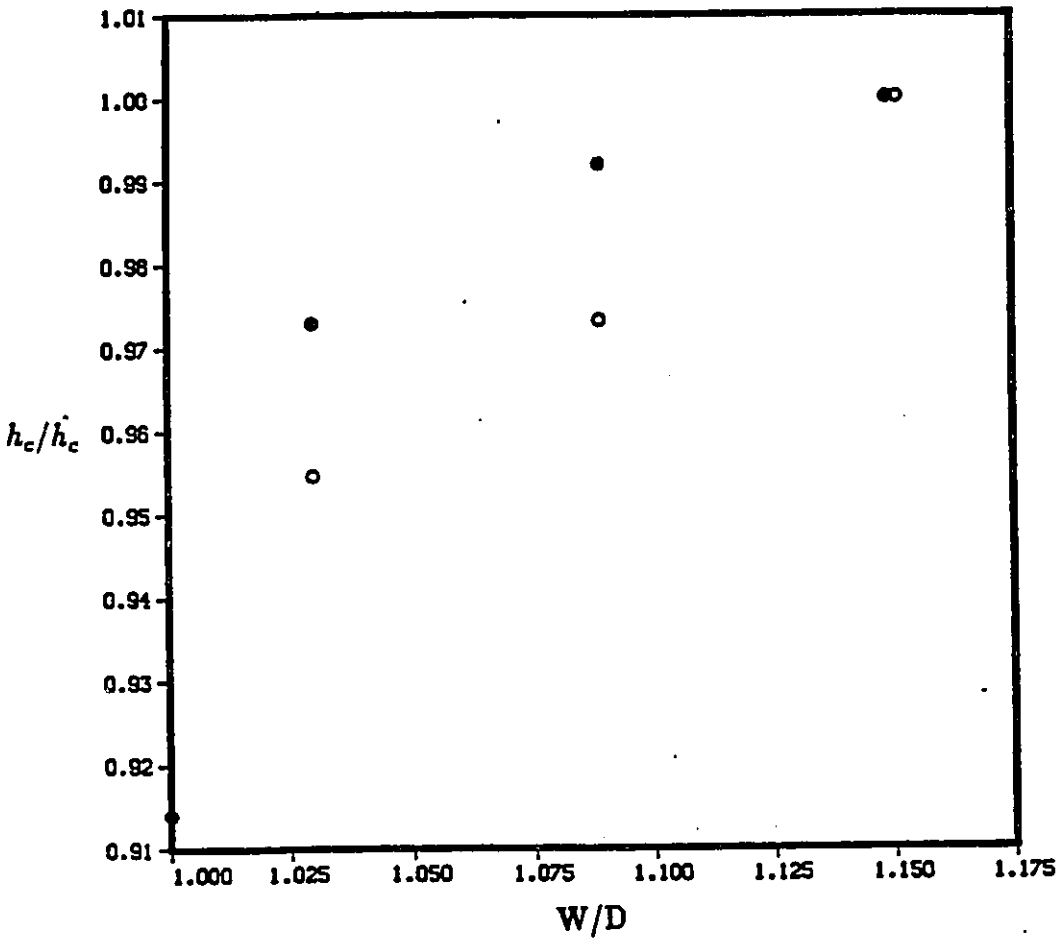

Figure 8.4: Variation of the corrected heat transfer coefficient with W/D at the rod-wall gap.

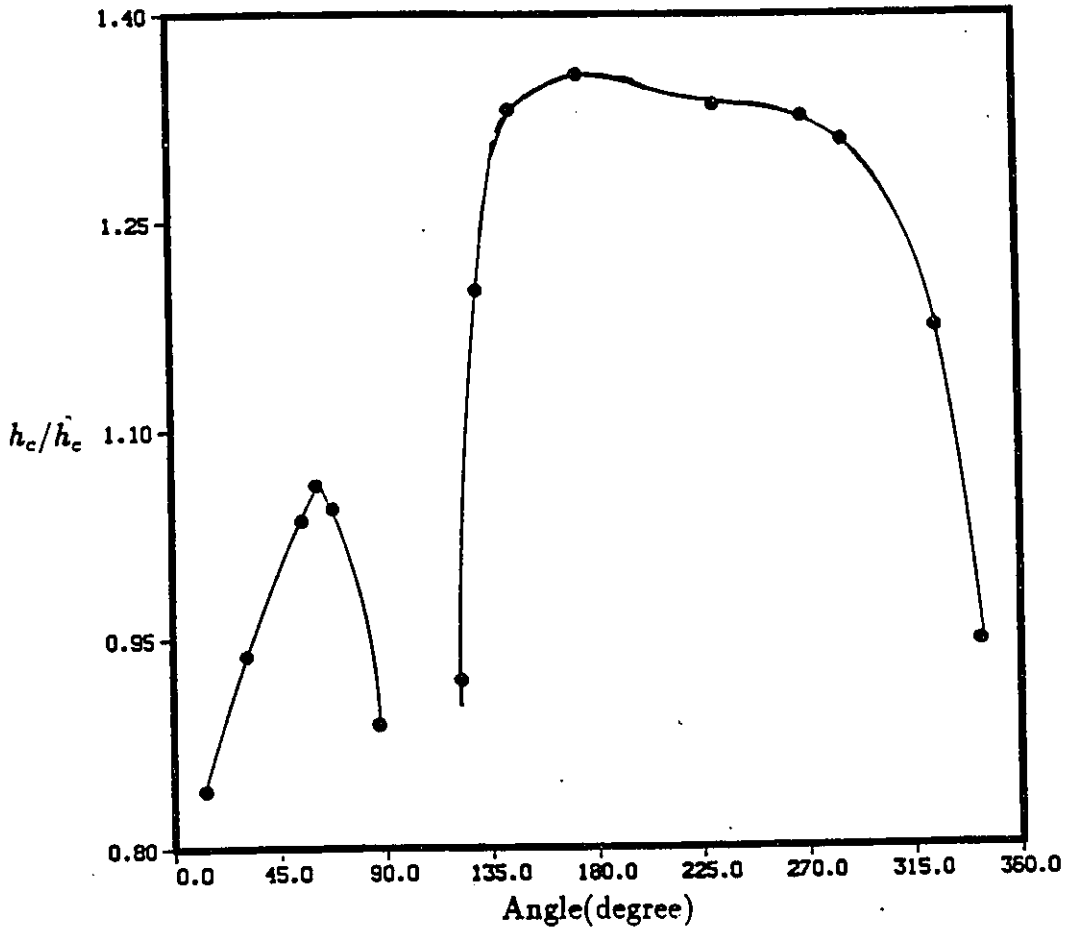

Figure 8.5: Distribution of the corrected heat transfer coefficient around the central rod for the rod-rod-wall contact position